Development of Ruddlesden-Popper type intercalation cathode material for all solid-state fluoride ion batteries

Hidenori Miki

Development of Ruddlesden-Popper type intercalation cathode material for all solid-state fluoride ion batteries

Hidenori Miki

Graduate School of Human and Environmental Studies
Kyoto University

Supervised by
Prof. Dr. Yoshiharu Uchimoto

Acknowledgements

I would like to express my special gratitude to Prof. Yoshiharu Uchimoto at the Graduate School of Human and Environmental Studies, Kyoto University, for his precise guidance and valuable advice. I am also grateful to Prof. Hiroshi Kageyama at the Graduate School of Engineering, Kyoto University, for his useful discussions and advice on writing papers with empathy.

I would like to express my sincere thanks to Dr. Kentaro Yamamoto of Nara Women's University and Dr. Toshiyuki Matsunaga at the Graduate School of Human and Environmental Studies, Kyoto University, for their effective discussions and advice on writing papers.

I would like to appreciate Dr. Hideki Iba, Dr. Shinji Nakanishi and Dr. Hideyuki Koga of Toyota Motor Corporation, for giving me this excellent opportunity to enter the doctoral program.

I would like to express my sincere thanks to Prof. Koji Amezawa of Tohoku University, Dr. Koji Nakanishi of the University of Hyogo and Prof. Yuki Orikasa of Ritsumeikan University, for their helpful advice and valuable discussions.

I would like to thank all the members of Uchimoto's laboratory, especially Dr. Takahiro Yoshinari, Mr. Hiroyuki Nakaki, Mr. Shuo Cao, Dr. Yanchang Wang, and Mr. Zhuoran Li, for their assistance and discussions. I would also like to thank Dr. Takeshi Tojigamori, Mr. Kazuto Ide, Mr. Kentaro Nakagawa, and Mr. Koki Terada of Toyota Motor Corporation for their assistance and discussions.

Finally, I would like to express my sincere gratitude to my family, especially my wife Chisato and my children Ayato, Yuua, and Nanoha for their understanding, support, and encouragement.

Without the support of all the people who have been involved with me, this thesis would not have been completed. I would like to express my deepest gratitude once again.

Hidenori Miki
February 2024

CONTENTS

Chapter 1.

Chapter 2.

Chapter 3.

Chapter 4.

Chapter 1.
General Introduction

1.1. Background

For realization of a sustainable society, moving away from fossil fuels by diversifying energy is required. In the background, there are problems such as depletion of energy resources and suppression of CO_2 emissions due to remarkable industrial development and liberalization of mobility of people and things. CO_2 accounts for about 70% of greenhouse gases, which are regulated by international treaties under the Kyoto Protocol. The Paris Agreement also adopted in 2015 has the goal of "suppressing the temperature rise below 2 °C compared to before the Industrial Revolution". In the "Global Warming Countermeasures Plan" approved by the Cabinet on May 13, 2016, Japan stated that "the long-term goal is to reduce greenhouse gas emissions by 80% by 2050". Therefore, a high energy power storage system, which has the function of stabilizing the output fluctuation of sustainable energy and the function of surplus absorption of electric power, is demanded together with the development of sustainable energy resources such as hydropower, geothermal power, wind power, and biomass. The development of high-capacity, long-life, low-cost secondary batteries have been actively promoted to realize the power storage system.

Similarly, in the automobile industry and the transportation field, conversion to electric vehicles (electric vehicles, plug-in hybrid vehicles, hybrid vehicles) has been promoted worldwide in order to reduce energy consumption. For example, the UK and France have announced a policy to ban the sale of internal combustion vehicles by 2040.

The Japanese government has also set a target of 20-30% of EV (including plug-in hybrid) share in new car sales by 2030. Therefore, in order to widely spread electric vehicles, high-performance in-vehicle storage battery technology, that can exceed current batteries, are strongly demanded similar to the infrastructure development such as charging facilities.

Among the secondary batteries currently in practical use, the lithium ion secondary batteries (LIBs) have the highest energy density and high capacity[1]. LIBs were commercialized by Sony Corporation in 1991[2]. The schematic diagram[3] is shown in **Fig. 1-1**. A typical LIB consists $LiCoO_2$ as the carhode[4], graphite as the anode[5]. It has become a mature technology, such as being used for small-sized electronic devices and in-vehicle batteries. On the other hand, however, the demands of the world are increasing day by day, and there is a constant requirement for the development of battery technology with higher energy density and higher input/output for longer cruising range of electric vehicles and faster charging[3,6]. Also, for further spread of electric vehicle batteries, resources such as lithium and cobalt are often attracting attention due to their high resource costs and risks. For these reasons, there is an increasing demand for development of innovative batteries, so-called post-LIBs, instead of LIBs.

Here, the battery capacity Q [mAh/g] and the energy density W [Wh/kg] will be described by the following equations (1. 1) and (1. 2):

$$\mathrm{Q} = \frac{\mathrm{F}}{\mathrm{M}} \times n \times \frac{1000}{3600} \qquad \mathbf{(1.1)}$$

$$\mathrm{W} = \mathrm{Q} \times \mathrm{E} \qquad \mathbf{(1.2)}$$

Where, M [g/mol], F [C/mol], n and E [V] means the molecular weight of the active material, the Faraday constant, the number of electrons related to the positive electrode/negative electrode reaction, and the battery voltage, respectively. That is, the number of reaction electrons per molecular weight and the battery voltage are considered as the controlling factors for increasing the capacity and energy density of the battery.

Examples of the post-LIBs include lithium-air batteries[7], lithium-sulfur batteries[8], and sodium ion secondary batteries[9] and magnesium ion secondary batteries[10] using different cation carriers. In particular, magnesium batteries use multivalent ions, which increases the number of reaction electrons per carrier. In other words, since two electrons per carrier contribute to the reaction in the charge/discharge reaction, it is expected that the electric capacity is doubled. (In the case of LIBs, one electron per carrier contributes to the charge/discharge reaction.) However, magnesium ions are divalent, their ionic radii are similar to lithium ions (Mg^{2+}: 72 pm, Li^{+}: 76 pm), so the charge density is higher[11]. It increases electrostatic attraction with anions and repulsion with cations, resulting in inhibition of diffusion of magnesium ions in electrode material[12].

On the other hand, studies on batteries using anions (e.g., hydride ions[13], fluoride ions[14], chloride ions[15]) as carriers have also been reported. These have the potential to utilize multi-electron reactions of polyvalent metals while the carrier ions are monovalent anions. Furthermore, these monovalent anions are considered advantageous over multivalent cations in terms of diffusion in the solid phase. In particular, with regard to fluoride ion batteries (FIBs), there are reports of operation in all-solid-state batteries, which are attracting attention as high energy density batteries for post LIBs[16].

1.2. All Solid-State Fluoride Ion Batteries

1.2.1. Mechanism

The operation mechanism of the charge/discharge reaction of the all solid-state FIBs is shown the schematic diagram in **Fig. 1-2** and the reaction equation (1.3) and (1.4). Upon discharge process, the metal fluorides $M\mathrm{F}_x$ in the cathode receives electrons from an external circuit, resulting in reduction to the metal M. Fluoride ions move through the electrolyte and bind with anode metal M' to form metal fluoride $M'\mathrm{F}_x$. The reverse reaction proceeds upon charge process.

$$\text{Cathode}: x\mathrm{e}^- + M\mathrm{F}_x \rightarrow M + x\mathrm{F}^- \qquad \textbf{(1.3)}$$

$$\text{Anode}: x\mathrm{F}^- + M' \rightarrow M'\mathrm{F}_x + x\mathrm{e}^- \qquad \textbf{(1.4)}$$

1.2.2. Solid Electrolytes

There are many research reports on fluoride ion conductors since the 1980s. **Fig. 1-3** shows the conductivity of reported fluoride ion conductors[17]. At present, tetragonal-type $M\mathrm{SnF}_4$ (M = Pb, Ba, Sr) (space group; tetragonal) has been reported as a fluoride ion conductor with high ionic conductivity even at room temperature, among them, PbSnF_4 has the highest ion conductivity[18]. However, there are few reports that they have been used as solid electrolytes for batteries because the solid electrolytes including Sn and Pb elements should have poor reduction stability. $\mathrm{La}_{0.9}\mathrm{Ba}_{0.1}\mathrm{F}_{2.9}$ with tysonite-type structure has lower conductivity than tetragonal-type PbSnF_4-based materials but has a relatively wide electrochemical potential window, there are some reports, therefore, as a solid electrolyte for an all-solid-state battery[19–22]. (In this thesis also, $La_{0.9}Ba_{0.1}F_{2.9}$ is used as the solid electrolyte.) Nevertheless, most reports still conduct charge/discharge tests at temperatures above 100 °C. The development of solid electrolytes with both high ionic conductivity and high reduction stability is desired.

Conduction mechanisms of reported materials have been investigated toward developing the solid electrolytes with higher ionic conductivity[23,24]. The ion conduction basically has a mechanism with hopping between sites in the crystal structure. The ionic conductivity is determined by the ion concentration and its mobility, and the ionic conductivity can be increased by improving these two parameters. Attempts, which introduce defects such as anion vacancies by doping heterovalent cations in fluoride ion conductors, have also been made to improve the ionic conductivity[25].

For example, tysonite-type $La_{0.9}Ba_{0.1}F_{2.9}$ is also well-known as an ionic conductor in which 10 mol% of LaF_3 is substituted with BaF_2, and there have been many reports on ion conduction mechanisms and differences in conductivity due to synthesis methods, in recent years[25]. The tysonite-type $La_{0.9}Ba_{0.1}F_{2.9}$ in various form (powder, sintered, single crystal) were investigated by electrochemical examination[24]. Among them, single crystal has the highest conductivity, while the ball-milled (powder) sample has the lowest conductivity. This result suggests that the bulk conductivity is faster than that of the grain boundary.

Conduction mechanism analysis using solid-state MAS-NMR (Solid State Magic Angle Spinning Nuclear Magnetic Resonance) has been also reported[25]. The electrochemical impedance method for solid electrolytes can calculate the specific ionic conductivity by dividing the grain boundaries, electrodes, and bulk resistances with different time constants. On the other hand, solid-state NMR can investigate the state of molecular motion and the distance and angle between nuclei. The spectrum was obtained from solid-state ^{19}F NMR at each content of Ba in $La_{1-x}Ba_xF_{3-x}$. In the tysonite structure, there are three independent fluorine atom sites F1, F2, and F3, and peaks attributed to each site are observed. In addition, it has been reported the F1 site would have the most influence on fluoride ion conduction in the literature. In the ^{19}F NMR spectrum, the spectrum change is observed with the Ba content. This result suggests that the F2 and F3 sites can contribute to conduction increase due to the introduction of vacancy, not only the F1 site.

1.2.3. Electrode Active Materials

Metal (or metal fluoride) has been studied as an electrode active material, in particular, studying metal fluorides such as CuF_2 and BiF_3 have been reported as cathode active materials[14,26]. **Fig. 1-4** shows charge/discharge curves using various metal fluorides as cathode[14]. $La_{0.9}Ba_{0.1}F_{2.9}$ and Ce metal were used as a solid electrolyte and an anode, respectively. The charge/discharge reaction was examined at a current density of 10 $\mu A/cm^2$ with low current rate. BiF_3 shows 190 mAh/g of the initial discharge capacity, corresponding to 62% of the theoretical capacity. The discharge capacity decreases to almost half in the initial 10 cycles.

Similarly, there is a report on the charge/discharge behavior of the CuF_2 cathode[26]. $La_{0.9}Ba_{0.1}F_{2.9}$ and La metal are used as the solid electrolyte and the anode, respectively. The evaluation was measured at 150 °C, 4 mA/g of a very low current rate, which corresponds to 1/135 C converted in C-rate. The 1st discharge capacity delivers 360 mAh/g, which corresponds 68% of the theoretical capacity. However, the discharge capacity at the 10th cycle dramatically decreased to 168 mAh/g, which is still a challenge with the cycle characteristics. As for anode active materials, CeF_3, MgF_2, CaF_2 were examined by incorporating into the full cell of all-solid-state battery[27]. The metal peaks which indicate defluorination of each metal fluoride upon charge process are confirmed by XRD. However, there are no reports of half cells evaluation, which shows the performance only anode material, so other properties are unknown. Anode materials should also have issues similar to cathode materials due to their same charge/discharge mechanism.

In summary, ever reported active materials should mainly have two issues shown in **Fig. 1-5**: rate capability and cycle performance. These problems can be attributed to the fact that the charge/discharge reaction mechanism has a metal/metal fluoride conversion-like reaction. The active materials do not have a clear fluoride ion diffusion path during (de)fluorination, therefore the fluoride ion diffusivity is low resulting in the poor rate capability. In addition, this conversion-like reaction generally greatly changes the crystal structure of the active material, and thus causes dramatic expansion/contraction of the active material during the charge/discharge process. This volume change due to expansion/contraction is a big challenge for all solid-state batteries which forms a solid-solid interface with the electrolyte. That is, a decrease in contact strength and contact area at the interface due to expansion/contraction prevent from the transfer of electrons and carriers, resulting in a decrease in charge/discharge capacity for each cycle. For the practical application of FIBs, fundamental solutions to these problems are desired.

1.3. Strategy for Novel Active Materials

1.3.1. Intercalation-type Cathode Active Materials

One solution for the essential problem of the metal/metal fluoride conversion reaction described above will be the application of an intercalation reaction. The intercalation reaction refers to a reaction in which carrier ions are topochemically inserted into and extracted from the host crystal structure during charge and discharge. A typical LIB utilizes intercalation reaction[2,4,5]. Lithium ions can be inserted electrochemically into the graphite layer of the negative electrode and the layered rock salt type oxide of the positive electrode. The capacity degradation of the intercalation type active material due to their volume expansion/contraction can be suppressed because that volume change was smaller than that of the conversion type active material during charge and discharge. In addition, since there is a clear diffusion path of lithium ions in the active material, it is generally superior to the conversion material in terms of rate performance. Also in FIBs, improvement of charge/discharge characteristics can be expected by utilizing intercalation reaction.

1.3.2. Li-excess cathode involving anionic redox in LIBs

In the previous paragraph, we described the advantages of intercalation reaction material systems over conversion reaction material systems. However, intercalation type active material system generally has a challenge showing lower theoretical capacity than that of the conversion material, and there would be some trade-off relationship between a capacity and a cycle stability/rate performance. In order to solve this problem, various material developments are being studied. Among them, Li-rich cathode active material, which has excess lithium that cannot be completely de-intercalated by only the transition metal redox, can be one promising candidate to achieve both high capacity and cycle stability by utilizing the anionic redox[28–30].

Recently, research reports on the use of anion redox have been increasing. *Yabuuchi* et al. reports that $Li_{1.3}Nb_{0.3}Mn_{0.4}O_2$ and $Li_{1.2}Ti_{0.4}Mn_{0.4}O_2$ with a rock salt structure can express a high capacity around 300 mAh/g by using both cationic and anionic redox reaction reversibly[31]. In addition, the conditions for enabling reversible use of anion redox are considered from the band structure of oxygen and transition metal as shown in **Fig. 1-6**. In the case of Fe contained active material, superoxide ions O_2^- are generated by reductive coupling due to the relationship between these energy levels, resulting in oxygen release, so the redox of oxide ions cannot be used reversibly. On the other hand, in the case of Mn contained active material, it has been reported that oxide ions are stabilized as peroxide ions $(O_2)^{2-}$ because they do not receive electrons, leading to the stable use of anion redox.

1.3.3. Ruddlesden-Popper type Layered Perovskite

As described so far, with reference to the development of intercalation materials in LIBs, we will study to explore the fluoride ion intercalation type active materials. Ruddlesden-Popper type structure is a kind of layered perovskite type structure represented by chemical formula $A_{n+1}B_nO_{3n+1}$ (n = 1, 2, 3…), in which perovskite layers and salt layers are alternately stacked. In the chemical formula, n represents the number of perovskite phases. **Fig. 1-7** shows a schematic diagram of the layered perovskite structure from $n = 1$ to $n = 3$. Many studies have been conducted on this layered perovskite material due to their various physical properties, which are expressed by combination of cations and fine composition control, such as superconductivity and magnetism.

Additionally, research focusing on the anion site in the materials has been increasing in recent years. One of them is a study on the structure and physical properties of materials in which oxygen is replaced by fluorine or fluorine is introduced into vacancies[32]. These oxyfluorides are often synthesized by introducing chemical fluorine into a layered perovskite oxide at a relatively low temperature using a fluorinating agent. There are four types of fluorination of layered perovskite oxides[33]: (1) Reductive fluorine introduction. (2) Fluorine substitution of oxygen. (3) Oxidative fluorine introduction. (4) Rearrangement with the reactions (1) ~ (3). In order to use as electrode materials, the oxidative fluorination route (3) is desirable because fluoride ion is taken in the crystal structure during charge (oxidation) process. As a material group applicable to (3) (e.g., $Sr_3Ru_2O_7F_2$[34], $Ln_{1.2}Sr_{1.8}Mn_2O_7F_2$[35] ($Ln$ = lanthanide element), and $La_2SrCr_2O_7F_2$[36]), in which fluorine is topochemically inserted into a rock layer of Ruddlesden-Popper structure as shown in **Fig. 1-8**, have been reported.

1.3.4. Previous Research and the Challenges

Oliver et al. has reported studies for the application of intercalation reaction to FIBs, such as $BaFeO_{2.5}$[37], $LaSrMnO_4$[38] and La_2CoO_4[39].

$BaFeO_{2.5}$, which is a brownmillerite structure represented by the chemical formula

$ABO_{2.5}$, has a structure in which a defect occurs at the oxygen site of the perovskite structure ABO_3. In anticipation of insertion/extraction of fluoride ions to/from defects at the oxygen site, a charge/discharge test with an all-solid-state battery was conducted at 150 ° C and 10 μA, and it was reported a discharge capacity of about 5 mAh/g was obtained repeatedly, as shown in **Fig. 1-9.**

In $LaSrMnO_4$ with a layered perovskite structure, the synthesis of $LaSrMnO_4F$ by chemical fluorination using F_2 gas has been reported by *Greaves* et al., and they have also reported from structural analysis that fluorine was inserted between the perovskite layer and the rock salt layer[40]. Based on the results, an all-solid-state battery was prepared to examine the fluoride ion electrochemical intercalation under the condition at a low current of 10 μA and 170 °C, and the authors reported that electrochemically topochemical fluorination of $LaSrMnO_4$ has been succeeded. It is reported that the potential plateau can be confirmed at 0.3 V and 1.25 V during charge process shown in **Fig. 1-10**, and fluorinated compounds such $LaSrMnO_4F$ and $LaSrMnO_4F_{2-x}$ were also confirmed from the result of XRD measurement. However, the charge capacity shows 800 mAh/g, far exceeding the capacity of both $LaSrMnO_4F$ (77.5 mAh/g) and $LaSrMnO_4F_2$ (155 mAh/g). On the other hand, the discharge capacity was obtained only ~100 mAh/g, with poor reversibility. In this regard, the authors consider that some side reaction should occur. Thus, although the possibility of the electrochemical intercalation reaction of fluoride ions to the layered perovskite structure could be shown, there are still many unclear points in charge-discharge mechanism.

M.A. Nowroozi et al. have reported also La_2CoO_4 as well as $LaSrMnO_4$. Although La_2CoO_4 has not been reported to be chemically fluorinated, an all-solid battery was formed, and a charge/discharge test was conducted at 170 °C under a current value of 10 μA. As shown in **Fig. 1-11**, when the cell was charged up to 65 mAh/g and 130 mAh/g of the capacity, 30 mAh/g and 22 mAh/g of discharge capacity were obtained, respectively. In both cases, the capacity decreased to less than 50% at the 50th cycle, and cycle characteristics could not have been improved by intercalation mechanism unlike as found in LIBs.

As described above, the possibility of fluoride ion intercalation at the oxygen defect site of perovskite structure and rocksalt layer in Ruddlesden-Popper type layered perovskite has been reported in previous reports. However, there still remains many unclear points about the charge/discharge mechanism, such as the charge reaction includes a large amount of side reactions that cannot be ignored or the expected discharge capacity (corresponding to the interstitial site between layers) has not been obtained. In addition, there remains a problem that the good cycle characteristics found in intercalation materials in LIBs have not been demonstrated (Challenge (1)).

Furthermore, even if Challenge (1) is solved, the charge/discharge capacity when all the sites between the layers can be utilized is only about 150 mAh/g, and the high energy density, which is the greatest advantage of FIBs, cannot be achieved (Challenge (2)) is easy to imagine.

No specific solution has been proposed for these Challenges, and the application of intercalation materials as cathode active materials for high energy density FIBs still requires a large breakthrough.

1.4. Motivation and Research Objective

In order to approach the practical application of FIBs, the development of new materials that can solve the challenges of electrodes as described above is required. The purpose of this study is to develop a novel intercalation type cathode material with excellent cycle stability and high energy density.

Attempt to develop materials in the following scenario: (i) To demonstrate a stable fluoride ion intercalation reaction by utilizing the n = 2 Ruddlesden-Popper phase. (ii) Increasing the capacity of the material by application of anion redox (to receive further fluoride ion) to cathode materials of FIBs.

Regarding (i), we are wondering that n = 1 Ruddlesden-Popper phase was focused in the previous reports[38,39], because, in the n = 1 Ruddlesden-Popper phase, especially in compounds containing Mn and Co as shown in the literature, up to 1 mol of fluorine can be incorporated into the structure by charge compensation of the transition metal redox (having empty sites which can receive up to 2 mol of fluorine). Furthermore, survey of chemically fluorinated Ruddlesden-Popper type oxyfluorides revealed that there are many studies on inserting fluorine into the rock salt layers in the n = 2 Ruddlesden-Popper phase. On the other hand, attempting to insert 2 mol of fluorine into the n = 1 Ruddlesden-Popper phase seems to promote the substitution reaction with oxygen (*c.f.* $Sr_2RuO_3F_2$[41], $La_2NiO_3F_2$[42]) shown in **Fig. 1-12**. In order to use the empty site in the rock salt layer stably for topochemical intercalation, we focused on $La_{1.2}Sr_{1.8}Mn_2O_7F_2$[35,43] which has the n = 2 Ruddlesden-Popper structure shown in **Fig. 1-13**, and examined the charge/discharge property. In order to use the empty site in the rock salt layer stably for topochemical intercalation, we focused on $La_{1.2}Sr_{1.8}Mn_2O_7F_2$ which has the $n = 2$ Ruddlesden-Popper structure, and examined the charge/discharge property.

With regard to (ii), we focus on the point that “in order to increase the capacity, it is necessary to incorporate excessive fluoride ion into the structure”. In research on proton conductors, it has been reported that excess oxide anions can be accommodated by the formation of peroxide ions in the perovskite structure[44]. Additionally, in LIBs, high capacity due to the formation of peroxide ions has also been reported for the Li-excess oxides mentioned above. Therefore, the insertion of excess fluoride ions to $La_{1.2}Sr_{1.8}Mn_2O_7F_2$ is examined.

1.5. Outline of the Present Thesis

The present thesis consists of six chapters, presenting electrochemical performances of a novel intercalation-type cathode active material for FIBs, involving the anionic redox leading high energy density, and additionally elucidating the reaction mechanism such as charge compensation and phase transition during charge/discharge process.

In Chapter 1, the basic principles of FIB and previous reports on the development of component materials such as electrode materials and solid electrolytes are described. Especially, the challenges of cathode materials are focused on, and development strategy of a novel fluoride ion intercalation cathode material toward electrode with excellent electrochemical performance are proposed, referring to the strategy of increasing the capacity of intercalation type material in LIBs.

In Chapter 2, Ruddlesden-Popper type layered perovskite $La_{1.2}Sr_{1.8}Mn_2O_7F_2$ is examined for electrochemical topotactic intercalation of fluoride ion. Additionally, an electrochemical performance as a high-capacity cathode for FIBs is also examined. Where fluoride ions are inserted is observed by Cs-STEM. Contributions of charge compensation during charge/discharge process are investigated by XAS analysis.

In Chapter 3, Phase transition mechanism during topotactic intercalation ion reaction of $La_{1.2}Sr1.8Mn_2O_7Fx$ ($0 < x < 2$) were investigated by XRD and XAS analysis. In order to investigate the crystal structural change in detail, various fluorinated states of $La_{1.2}Sr_{1.8}Mn_2O_7F_x$ are prepared by chemical fluorination using PVDF.

In Chapter 4, effect on fluoride ion diffusion in layered-perovskite cathode for fluoride ion batteries by controlling interlayer distance are investigated. The materials with controlled the interlayer distance are prepared by changing the ratio La/Sr in the compounds.

In Chapter 5, charge/discharge properties of layered perovskite containing various transition metals are examined, and effects of transition metal species on anionic redox reactions in Ruddlesden-Popper type oxyfluorides are considered, especially origins of high capacity.

In Chapter 6, conclusion obtained from the present studies.

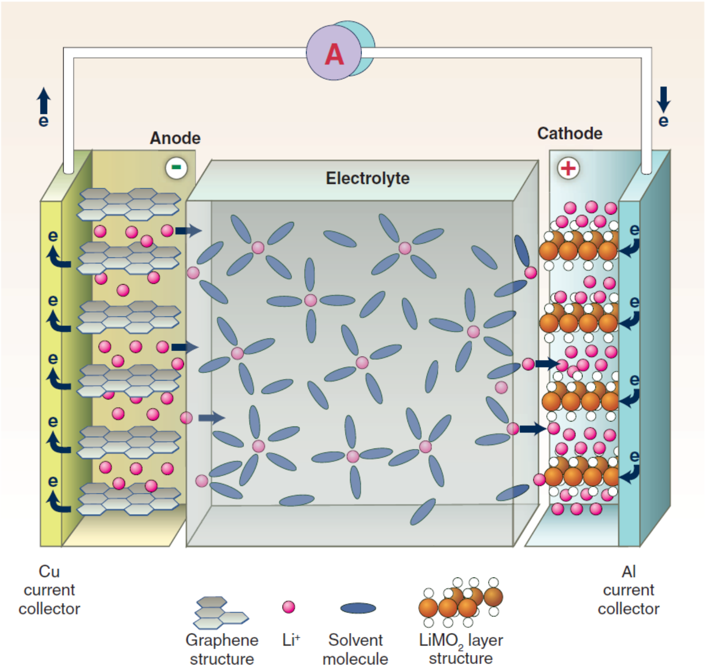

Fig. 1-1. Schematic diagram of a lithium ion battery[3]

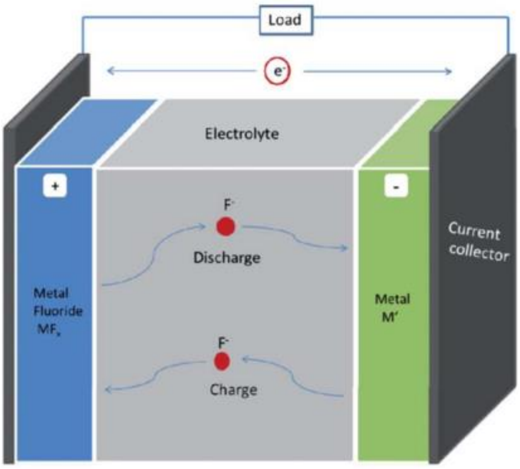

Fig. 1-2. Schematic diagram of a fluoride ion battery[14]

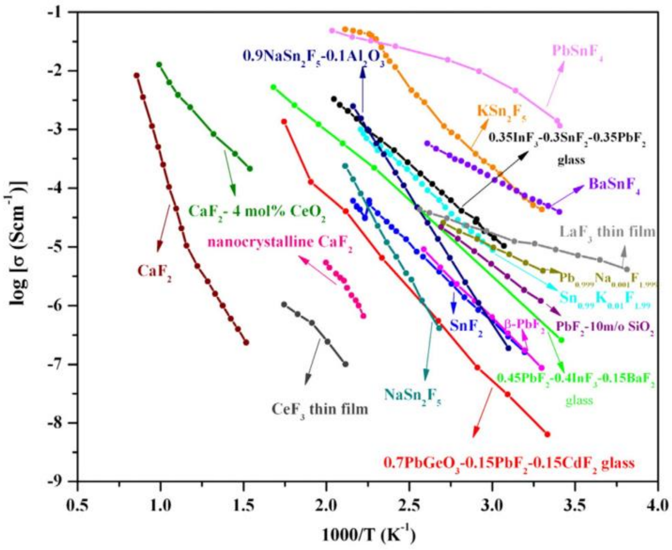

Fig. 1-3. Temperature dependent conductivity plots for typical fluoride ion conducting materials in the form of glasses, polycrystalline, nano-crystalline and thin film[17]

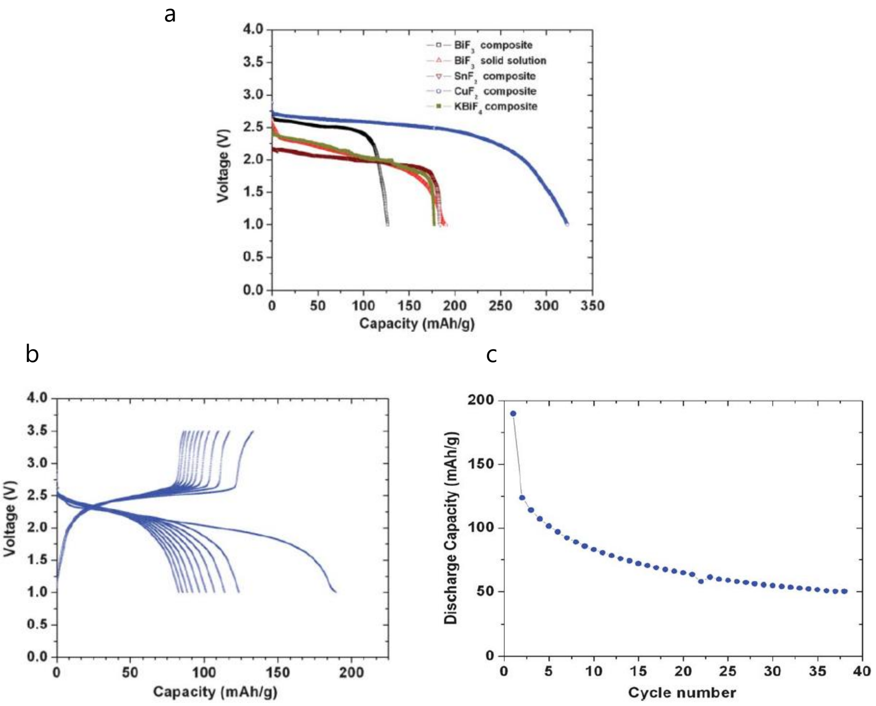

Fig. 1-4. Electrochemical examinations of various metal fluoride electrode materials. **a,** Discharge curves of various metal fluoride cathodes. **b,** Discharge-charge curves of BiF_3 cathode. **c,** Cycle performance of BiF_3 cathode.[14]

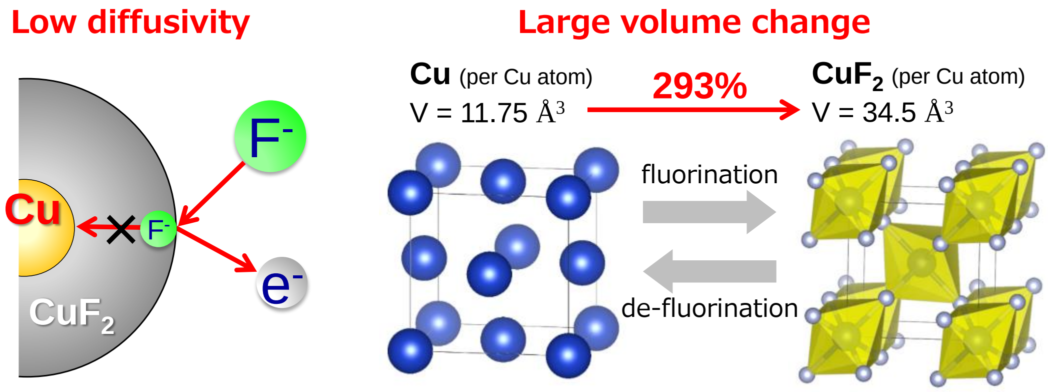

Fig. 1-5. Challenges for metal/metal fluoride active materials, especially Cu/CuF$_2$.

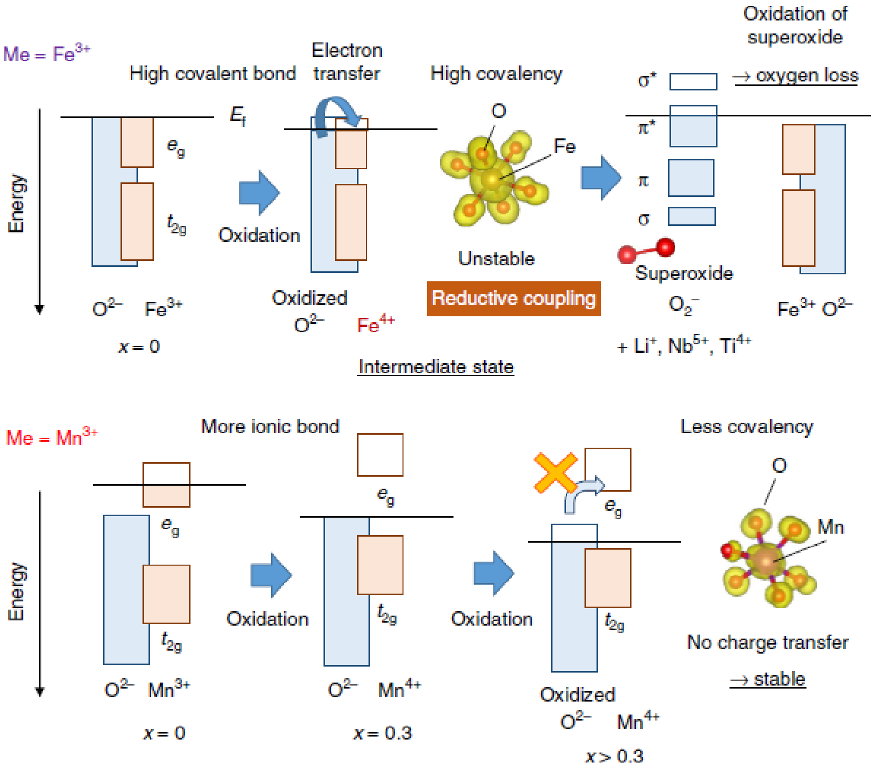

Fig. 1-6. Contribution of solid-state redox reaction of oxide ions to charge compensation in Li$_{1.3-x}$Nb$_{0.3}$Me$_{0.4}$O$_2$ (Me = Fe^{3+} and Mn^{3+}).[31]

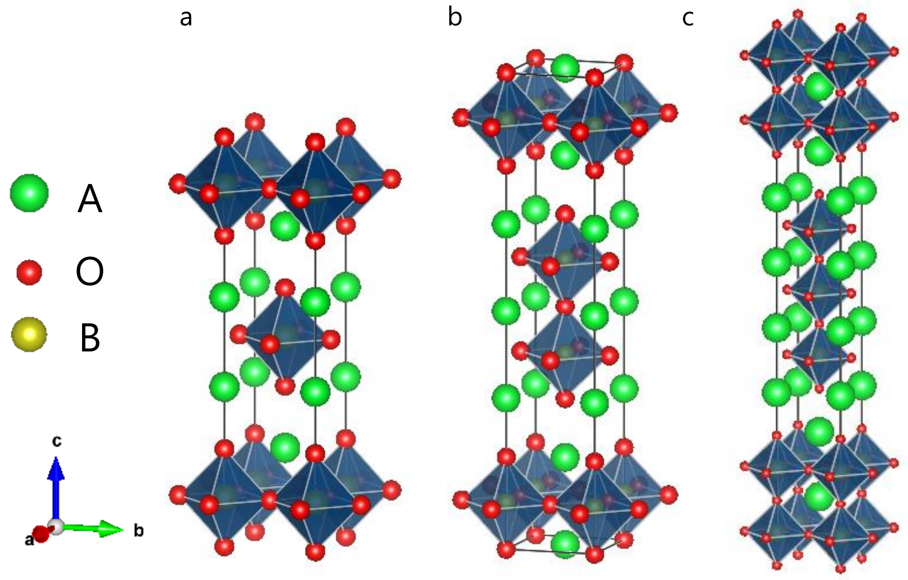

Fig. 1-7. The crystal structures of Ruddlesden-Popper type $A_{n+1}B_nO_{3n+1}$. **a,** $n = 1$. **b,** $n = 2$. **c,** $n = 3$. This figure is drawn by using VESTA package.[45]

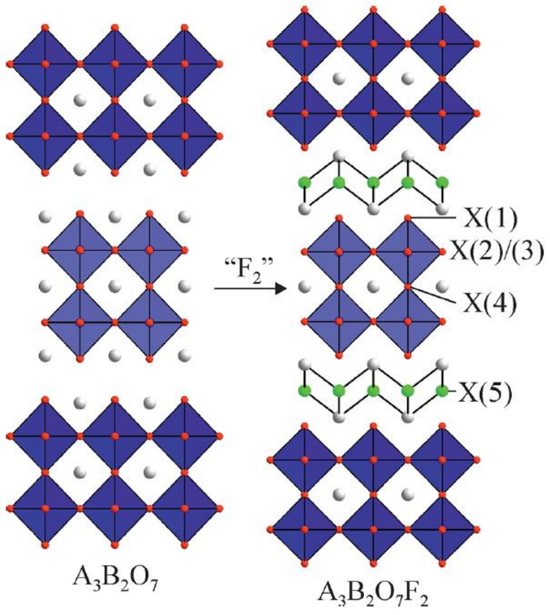

Fig. 1-8. Topochemical fluorination reaction of Ruddlesden−Popper type $A_3B_2O_7$, and the formation of the $A_3B_2O_7F_2$ by oxidative fluorine insertion.[36]

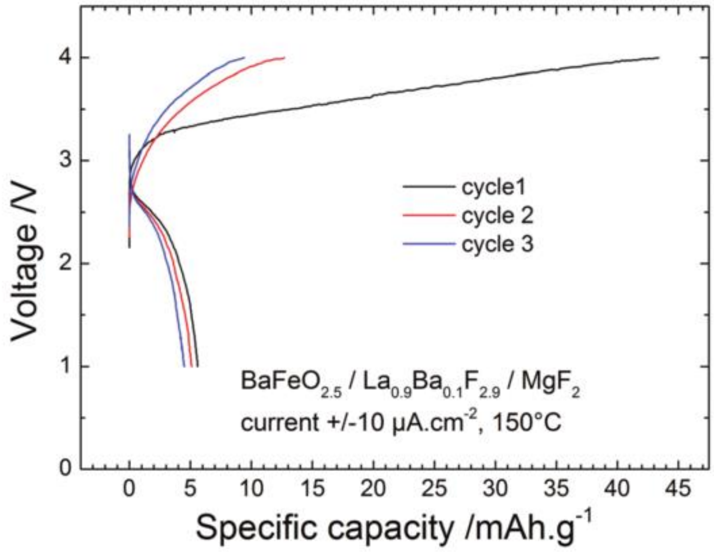

Fig. 1-9. Charge-discharge profiles of BaFeO$_{2.5}$ in all solid-state battery cell.[37]

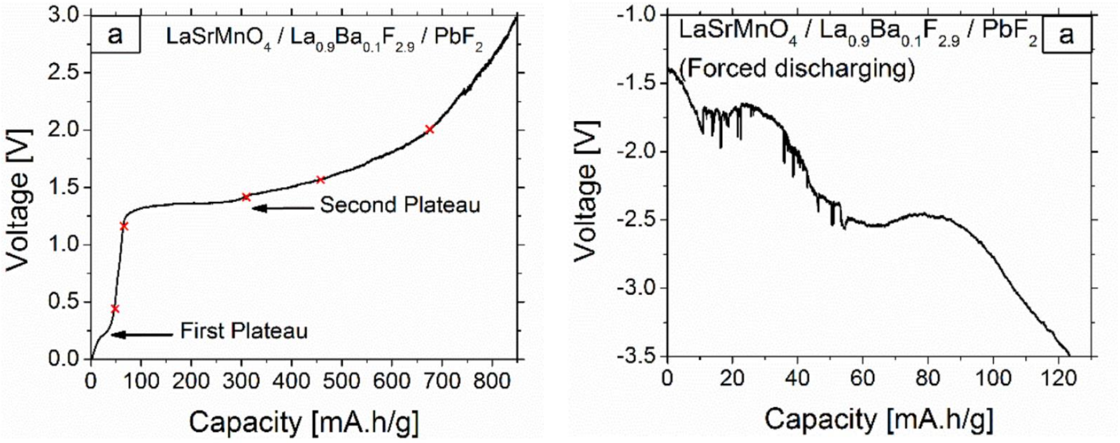

Fig. 1-10. Charge and discharge profiles of LaSrMnO$_4$ at 170 °C.[38]

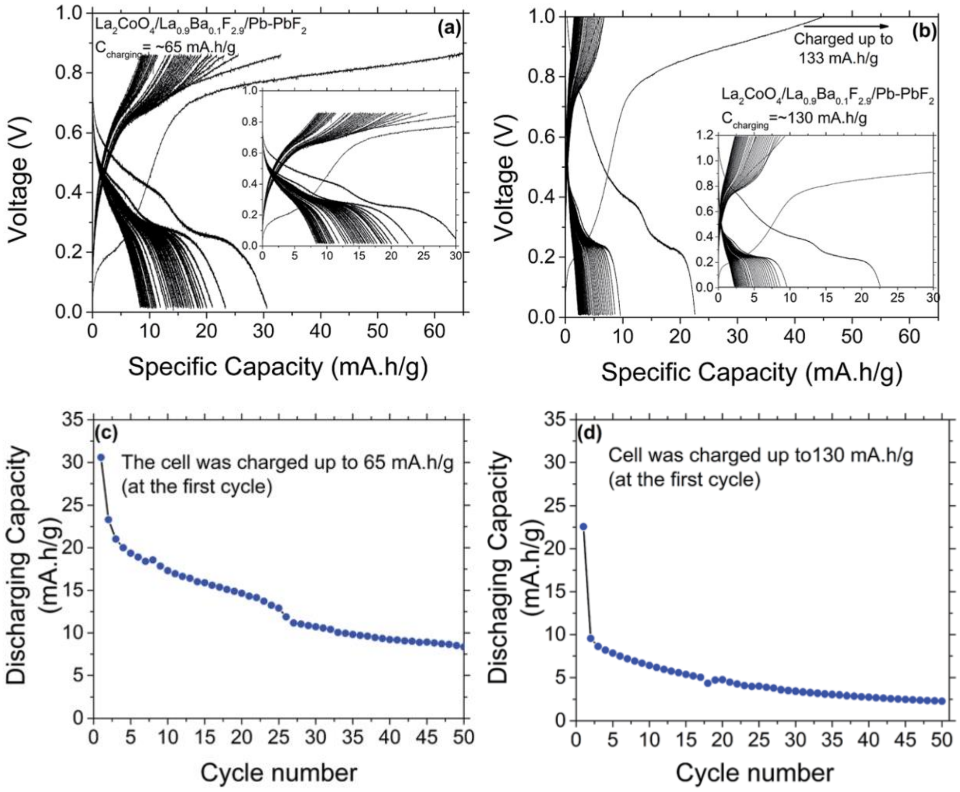

Fig. 1-11. Charge-discharge profiles and cycle performance of La_2CoO_4.[39]

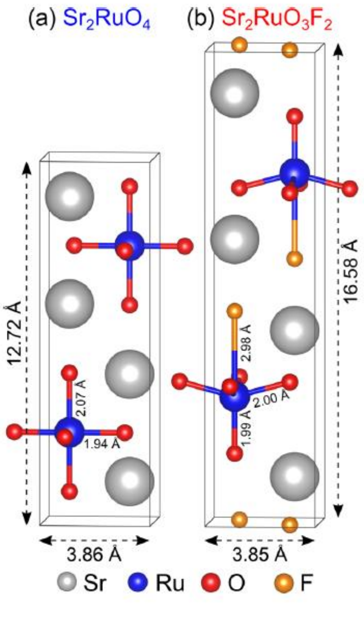

Fig. 1-12. Crystal structures of Sr_2RuO_4 and $Sr_2RuO_3F_2$ after fluorination.[41]

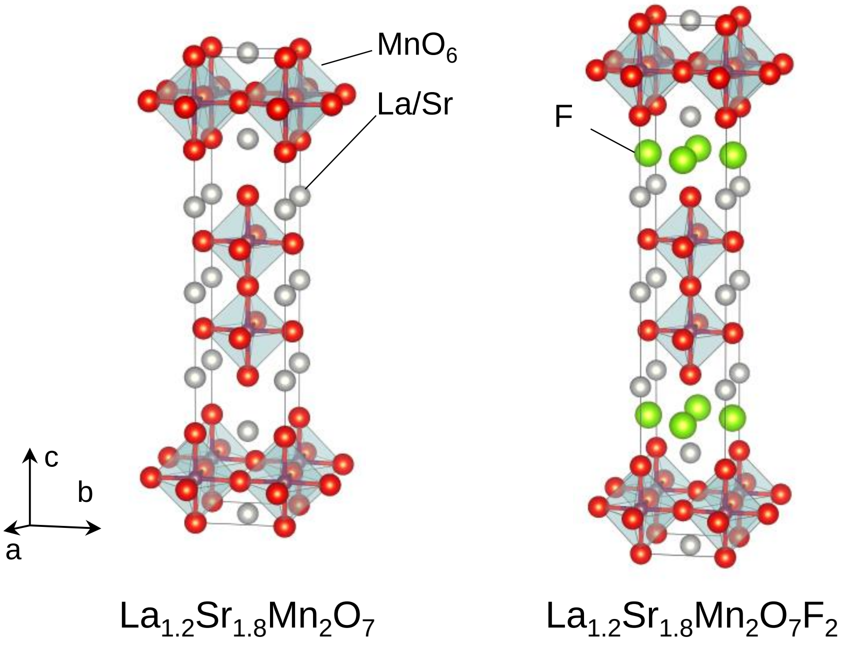

La$_{1.2}$Sr$_{1.8}$Mn$_2$O$_7$ La$_{1.2}$Sr$_{1.8}$Mn$_2$O$_7$F$_2$

Fig. 1-13. Crystal structures of La$_{1.2}$Sr$_{1.8}$Mn$_2$O$_7$ and La$_{1.2}$Sr$_{1.8}$Mn$_2$O$_7$F$_2$ drawn by using VESTA package.[45]

1.6. References

1. Goodenough, J. B. & Park, K. S. The Li-ion rechargeable battery: A perspective. *J. Am. Chem. Soc.* **135**, 1167–1176 (2013).

2. Yoshino, A. The birth of the lithium-ion battery. *Angew. Chemie - Int. Ed.* **51**, 5798–5800 (2012).

3. Dunn, B., Kamath, H. & Tarascon, J. M. Electrical energy storage for the grid: A battery of choices. *Science (80-.).* **334**, 928–935 (2011).

4. K. Mizushima, P. C. Jones, P. J. Wiseman, J. B. G. LixCoO2 (0<x<-1): A new cathode material for batteries of high energy density. *Mater. Res. Bull.* **15**, 783–789 (1980).

5. Yazami, R. & Touzain, P. A reversible graphite-lithium negative electrode for electrochemical generators. *J. Power Sources* **9**, 365–371 (1983).

6. M. Armand, J.-M. Tarascon. Building better batteries. *Nature* **451**, 652–657 (2008).

7. Lee, J. S. *et al.* Metal-air batteries with high energy density: Li-air versus Zn-air. *Adv. Energy Mater.* **1**, 34–50 (2011).

8. Bruce, P. G., Freunberger, S. A., Hardwick, L. J. & Tarascon, J. M. Li-O2 and Li-S batteries with high energy storage. *Nat. Mater.* **11**, 19–29 (2012).

9. Slater, M. D., Kim, D., Lee, E. & Johnson, C. S. Sodium-ion batteries. *Adv. Funct. Mater.* **23**, 947–958 (2013).

10. Aurbach, D. *et al.* Prototype systems for rechargeable magnesium batteries. *Nature* **407**, 724–727 (2000).

11. Orikasa, Y. *et al.* High energy density rechargeable magnesium battery using earth-abundant and non-toxic elements. *Sci. Rep.* **4**, 1–6 (2014).

12. Levi, E., Levi, M. D., Chasid, O. & Aurbach, D. A review on the problems of the solid state ions diffusion in cathodes for rechargeable Mg batteries. *J. Electroceramics* **22**, 13–19 (2009).

13. Kobayashi, G. *et al.* Pure H- conduction in oxyhydrides. *Science (80-.).* **351**, 1314–1317 (2016).

14. Anji Reddy, M. & Fichtner, M. Batteries based on fluoride shuttle. *J. Mater. Chem.* **21**, 17059–17062 (2011).

15. Zhao, X., Ren, S., Bruns, M. & Fichtner, M. Chloride ion battery: A new member in the rechargeable battery family. *J. Power Sources* **245**, 706–711 (2014).

16. Gschwind, F. *et al.* Fluoride ion batteries: Theoretical performance, safety, toxicity, and a combinatorial screening of new electrodes. *J. Fluor. Chem.* **182**, 76–90 (2016).

17. Patro, L. N. & Hariharan, K. Fast fluoride ion conducting materials in solid state ionics: An overview. *Solid State Ionics* **239**, 41–49 (2013).

18. Kanno, R., Nakamura, S. & Kawamoto, Y. Ionic conductivity of tetragonal PbSnF4 substituted by aliovalent cations Zr4+, Al3+, Ga3+, In3+ and Na+. *Solid State Ionics* **51**, 53–59 (1992).

19. Xiao, R., Li, H. & Chen, L. Density functional investigation on Li 2MnO 3. *Chem. Mater.* **24**, 4242–4251 (2012).

20. Zhang, L., Reddy, M. A., Gao, P. & Diemant, T. Study of all solid-state rechargeable fluoride ion batteries based on thin-film electrolyte. 1243–1251 (2017) doi:10.1007/s10008-016-3479-x.

21. Zhang, L., Reddy, M. A., Gao, P. & Fichtner, M. Development of dense solid state thin- fi lm electrolyte for fl uoride ion batteries. *J. Alloys Compd.* **684**, 733–738 (2016).

22. Zhang, L., Anji, M. & Fichtner, M. Development of tysonite-type fl uoride conducting thin fi lm electrolytes for fl uoride ion batteries. *Solid State Ionics* **272**, 39–44 (2015).

23. Preishuber-p, F. & Wilkening, M. structures and ion transport. 8675–8687 (2016) doi:10.1039/c6dt00944a.

24. Rongeat, C., Reddy, M. A., Witter, R. & Fichtner, M. Solid Electrolytes for Fluoride Ion Batteries : Ionic Conductivity in Polycrystalline Tysonite-Type

Fluorides. (2014) doi:10.1021/am4052188.

25. Chable, J., Dieudonné, B., Body, M. & Legein, C. Fluoride solid electrolytes: investigation of the tysonite-type solid solutions La1−xBaxF3−x (x < 0.15). (2015) doi:10.1039/c5dt02321a.

26. Thieu, D. T. *et al.* CuF 2 as Reversible Cathode for Fluoride Ion Batteries. **1701051**, 1–11 (2017).

27. Rongeat, C., Reddy, M. A., Diemant, T., Behm, R. J. & Fichtner, M. Development of new anode composite materials for fl uoride ion batteries †. 20861–20872 (2014) doi:10.1039/c4ta02840f.

28. Kim, J. *et al.* Electrochemical and Structural Properties of Batteries (M ′) Ti , Mn , Zr ; 0 e x E 0 . 3). 1996–2006 (2006) doi:10.1021/cm0306461.

29. Batteries, R. *et al.* Detailed Studies of a High-Capacity Electrode Material for. 4404–4419 (2011) doi:10.1021/ja108588y.

30. Seo, D., Lee, J., Urban, A., Malik, R. & Kang, S. redox activity in layered and cation-disordered Li-excess cathode materials. *Nat. Chem.* **8**, 692–697 (2016).

31. Yabuuchi, N. *et al.* Origin of stabilization and destabilization in solid-state redox reaction of oxide ions for lithium-ion batteries. *Nat. Commun.* **7**, 1–10 (2016).

32. Tsujimoto, Y., Yamaura, K. & Takayama-Muromachi, E. Oxyfluoride Chemistry of Layered Perovskite Compounds. *Appl. Sci.* **2**, 206–219 (2012).

33. Mccabe, E. E. & Greaves, C. Fluorine insertion reactions into pre-formed metal oxides. **128**, 448–458 (2007).

34. Li, R. & Greaves, C. Double-layered ruthenate formed by fluorine insertion into. *Phys. Rev. B - Condens. Matter Mater. Phys.* **62**, 3811–3815 (2000).

35. Sivakumar, T. & Wiley, J. B. Topotactic route for new layered perovskite oxides containing fluorine: Ln1.2Sr1.8Mn2O7F2 (Ln = Pr, Nd, Sm, Eu, and Gd). *Mater. Res. Bull.* **44**, 74–77 (2009).

36. Zhang, R. *et al.* La2SrCr2O7F2: A Ruddlesden-Popper Oxyfluoride Containing Octahedrally Coordinated Cr4+ Centers. *Inorg. Chem.* **55**, 3169–3174 (2016).

37. Clemens, O. *et al.* Electrochemical fluorination of perovskite type BaFeO2.5. *Dalt. Trans.* **43**, 15771–15778 (2014).

38. Nowroozi, M. A., Wissel, K., Rohrer, J., Munnangi, A. R. & Clemens, O. LaSrMnO4: Reversible Electrochemical Intercalation of Fluoride Ions in the Context of Fluoride Ion Batteries. *Chem. Mater.* **29**, 3441–3453 (2017).

39. Nowroozi, M. A., Ivlev, S., Rohrer, J. & Clemens, O. La2CoO4: A new intercalation based cathode material for fluoride ion batteries with improved cycling stability. *J. Mater. Chem. A* **6**, 4658–4669 (2018).

40. Aikens, L. D., Li, R. K. & Greaves, C. The synthesis and structure of a new oxide fluoride, LaSrMnO4F, with staged fluorine insertion. *Chem. Commun.* 2129–2130 (2000) doi:10.1039/b007045i.

41. Chikamatsu, A. *et al.* Spectroscopic and theoretical investigation of the electronic states of layered perovskite oxyfluoride S r2Ru O3 F2 thin films. *Phys. Rev. B* **97**, 2–8 (2018).

42. Wissel, K. *et al.* Topochemical Fluorination of La2NiO4+d: Unprecedented Ordering of Oxide and Fluoride Ions in La2NiO3F2. *Inorg. Chem.* **57**, 6549–6560 (2018).

43. Greaves, C., Kissick, J. L., Francesconi, M. G., Aikens, L. D. & Gillie, L. J. Synthetic strategies for new inorganic oxide fluorides and oxide sulfates. *J. Mater. Chem.* **9**, 111–116 (1999).

44. Middleburgh, S. C. *et al.* Peroxide defect formation in zirconate perovskites. *J. Mater. Chem. A* **2**, 15883–15888 (2014).

45. Momma, K. & Izumi, F. VESTA 3 for three-dimensional visualization of crystal , volumetric and morphology data. 1272–1276 (2011) doi:10.1107/S0021889811038970.

Chapter 2.

Double-layered Perovskite Oxyfluoride Cathode with High Capacity Involving O–O Bond Formation for Fluoride Ion Batteries

Abstract

Developing electrochemical high-energy storage systems is of crucial importance towards a green and sustainable energy supply. A promising candidate is fluoride ion batteries (FIBs), which can deliver a far higher volumetric energy density than lithium-ion batteries. However, typical metal fluoride cathodes with conversion-type reaction causes a low-rate capability. Recently, layered perovskite oxides and oxyfluorides such as $LaSrMnO_4$ and $Sr_3Fe_2O_5F_2$ have been reported to exhibit relatively high-rate performance and cycle stability compared to typical metal fluoride cathodes with conversion-type reaction, but their discharge capacities (~ 118 mAh/g) are lower than typical cathode's ones used in lithium-ion batteries. Here we show that a double-layered perovskite oxyfluoride $La_{1.2}Sr_{1.8}Mn_2O_{7-\delta}F_2$ exhibits (de)intercalation of two fluoride ions to rock-salt slabs and further (de)intercalation of excess fluoride ions to the perovskite layer, leading to a reversible capacity of 200 mAh/g. The additional fluoride ions intercalation leads to the formation of O–O bond in the structure for charge compensation (i.e., anion redox). These results highlight the layered perovskite oxyfluorides as a new class of active materials for the construction of high-performance FIBs.

2.1. Introduction

Considerable efforts have been devoted to developing efficient energy storage systems in order to achieve a green and sustainable energy society in the future. The widespread success of lithium-ion rechargeable batteries (LIBs) is attributed to their high energy density, long-term durability, and the presence of a large number of available host structures[1]. In recent years, special attention has been paid to enhancing the capacity of cathode materials through the redox of oxide anions (leading to the formation of O^-, O_2^{2-}, O_2^- and O_2), in addition to the redox of transition metal cations[2–11]. However, there is a growing demand for electric vehicles with longer mileage for which developing power sources with more volumetric energy density is required.

In order to meet these requirements, various types of batteries (e.g., all-solid-state, air battery type, redox flow type) using different carrier ions (e.g., Li^+, Na^+, Mg^{2+}, Cl^-, F^-) have been proposed[11–20]. Among them, fluoride ion batteries (FIBs) with fluoride ions working as a carrier are highly promising with respect to theoretical high volumetric energy densities[20–27]. The highest electronegativity of fluorine as well as high redox potential 2.87 V (vs. SHE) of F^-/F_2 (*cf.* 1.36 V for Cl^-/Cl_2, 0.54 V for I^-/I_2) allow the wide electrochemical potential window, leading to high voltage batteries[28]. A high electrochemical capacity per weight in conversion-type compounds (e.g., Cu/CuF_2) is also an advantage[20,22,23–27]. However, a drastic decrease in electronic conductivity and a large volume change during charge-discharge process seriously impairs rate capability and cycle stability.

For these reasons, as an alternative to the conversion type, the search for electrode candidates from materials capable of topotactic fluorine intercalation[29–33] appears to be promising, as has been with the case of LIBs (e.g., $LiCoO_2$[34] and $LiCo_{1/3}Ni_{1/3}Mn_{1/3}O_2$[35]). It has been reported electrochemical topotactic fluorinations in compounds such as $LaSrMnO_4$[36], Sr_2MnO_3F[37] and $Sr_3Fe_2O_5F_2$[38] with a Ruddlesden-Popper perovskite structure of $A_{n+1}B_nO_{3n+1}$ ($n = 1, 2$), in which A is a rare-earth or alkaline earth element and B is a transition metal[39–41]. Although these compounds exhibited relatively high-rate performance and cycle stability[37, 38] compared to conversion-type compounds, their capacities of 83 mAh/g (~0.98F^- per Sr_2MnO_3F) and 118 mAh/g (~2 F^- per $Sr_3Fe_2O_5F_2$) were smaller than typical cathode’s ones used in LIBs.

In this study, we demonstrate that chemically fluorinated $La_{1.2}Sr_{1.8}Mn_2O_{7-\delta}F_2$ oxyfluoride[30, 42] can electrochemically deintercalate (and intercalate) two fluoride ions by fully utilizing the interstitial site in the rock-salt slab. Unexpectedly, $La_{1.2}Sr_{1.8}Mn_2O_{7-\delta}F_2$ oxyfluoride can be further topotactically fluorinated beyond 2F to a capacity of 200 mAh/g, allowing the development of FIBs with high energy density and durability. Interestingly, these excess fluoride ions are introduced into the perovskite slabs, where oxygen-oxygen bond are formed for charge compensation (i.e., anion redox), as seen in delithiated/desodiated cathode materials of LIBs and sodium ion batteries[2–5,9]. To the best of our knowledge, this is the first report of the introduction of holes and the resulting formation of an oxygen-oxygen bond following electrochemical intercalation of an anion species. Given the abundance of perovskite compounds, these results are expected to facilitate the development of cathode materials for FIBs, as mixed-anion compounds with anion redox could be applied to active materials.

2.2. Experimental

2.2.1. Synthesis of Materials

$La_{1.2}Sr_{1.8}Mn_2O_7$ oxide was prepared by using conventional solid-state reaction similar to previously described[32]. Reagent grade of La_2O_3 (99.99%, Kojundo Chemical Laboratory), $SrCO_3$ (99.9%, WAKO pure chemical industries, ltd.) and MnO_2 (99.5%, WAKO pure chemical industries, ltd.) were used as starting materials. These materials were weighed in a stoichiometric ratio and mixed by planetary ball-milling for 10 h. This mixed powder was pressed into a pellet and annealed at 1400 °C for twice of 20 h in air with an intermediate grinding. $La_{1.2}Sr_{1.8}Mn_2O_{7-\delta}F_2$ oxyfluoride was synthesized from chemical fluorination of $La_{1.2}Sr_{1.8}Mn_2O_7$ oxide using polyvinylidene difluoride (PVdF) as previously reported[32]. 1.0 g of the obtained $La_{1.2}Sr_{1.8}Mn_2O_7$ powder and 1.5 g of PVdF (Aldrich, average Mw: ~180,000, average Mn: ~71,000) were placed in separate alumina boats, covered with a sagger in an electric muffle furnace, and heated at 400 °C for 10 h under air. $La_{0.9}Ba_{0.1}F_{2.9}$, using as a solid electrolyte with fluoride-ion conductivity, was synthesized as reported in the literature[43]. LaF_3 (99.9%, Kojundo Chemical Laboratory) and BaF_2 (99.9%, Kojundo Chemical Laboratory) were mixed in a molar ratio of 9:1 and ball-milled at 600 rpm for 12 h using Ar-filled 45 mL ZrO_2 pot and 30 g of Φ5 mm balls. The mixture was annealed at 600 °C for 10 h in Ar atmosphere.

2.2.2. Assembly of the Electrochemical Cell

The cathode composite consisted of $La_{1.2}Sr_{1.8}Mn_2O_{7-\delta}F_2$ oxyfluoride powder, $La_{0.9}Ba_{0.1}F_{2.9}$ powder and Vapor-Grown Carbon Fiber (Showa Denko, VGCF, battery grade), with mixed in a weight ratio of 30:60:10 by ball-milling for 10 h at 100 rpm using 45 mL of ZrO_2 pot and 30 g of ZrO_2 balls. $La_{0.9}Ba_{0.1}F_{2.9}$ and 0.2 mm thickness of Pb foil were used as a solid electrolyte and an anode, respectively. Additionally, in case of examination of further fluorination, PbF_2/acetylene black (Denki Kagaku Kogyo, AB) composites, mixed by ball-milling for 3 h at 600 rpm, are used as a fluorine source on anode side. The electrochemical cells were assembled in disk-shaped pellet by compressed cathode/solid electrolyte/anode layers. At first, 10 mg of cathode composite and 200 mg of $La_{0.9}Ba_{0.1}F_{2.9}$ were compressed heating at 120 °C for 45 min under 4 ton/cm^2. After that, Pb foil (and PbF_2/AB composite) was added as an anode layer and Pt foils were added on both ends as a current collector. These layers were compressed under 4 ton/cm^2. The diameter of the pellet was 11.28 mm. All fabrication processes of the all-solid-state type electrochemical cell were conducted under Ar atmosphere in a glovebox, in which the oxygen content and the dew point were controlled below 0.5 ppm and -90°C, respectively.

2.2.3. Electrochemical Measurement

Assembled cells were put in a sealed container without exposing to the air atmosphere. Charge and discharge experiments of the all-solid-state fluoride ion cells were conducted in a potential range –1.5~2.0 (or –1.5~3.0) V vs. Pb/PbF_2 at 140 °C heated by mantle heater. The lower cut-off potential was set at –1.5 V since $La_{0.9}Ba_{0.1}F_{2.9}$ (in the cathode) decompose under –2.4 V vs. PbF_2/Pb. Unless otherwise specified, 6.7 mA/g was applied as the current density. Rate dependence of the charge-discharge profiles were measured with various current densities at both charge and discharge process. Cyclic voltammetry was carried out with at a sweep rate of 1 mV/sec. The electrochemical properties of the electrochemical test cells were collected using a potentiostat/galvanostat apparatus (VMP3, Bio-Logic Science Instruments). Electrochemical impedance spectroscopy (EIS) was performed with frequency range of 1 MHz to 10 mHz.

2.2.4. Materials Characterization

XRD profiles of the material were obtained using Rigaku Ultima IV using Cu Kα radiation with 40 kV of tube voltage and 40 mA of current. Time-of-flight (TOF) neutron diffraction measurements were made using the special-environment neutron diffractometer super-HRPD located at the BL08 beam line and the total scattering spectrometer NOVA at the BL21 beam line of the Materials and Life Science Experimental Facility, Japan Proton Accelerator Research Complex (J-PARC MLF)[44, 45]. The $La_{1.2}Sr_{1.8}Mn_2O_{7-\delta}F_2$ oxyfluoride powder sample were placed in a cylindrical vanadium－nickel-alloy holder (diameter of 6 mm and thickness of 0.1 mm) in a high-purity argon atmosphere. The intensity was measured as a function of the neutron time-of-flight, I (TOF), at room temperature using a device for measuring neutron scattering data in a controlled argon gas atmosphere at high temperatures (Cryo-furnace). Spherical Aberration (Cs) corrected scanning transmission electron-microscope (Cs-corrected

STEM) observations and selected area electron diffraction (SAED) measurements were collected using JEM-ARM200F (JEOL) to characterize the crystal structures of the samples. Thin sections of the samples were fabricated by cryo-focused ion beam (cryo-FIB) micro-sampling technique using nanoDUE'T NB5000 (HITACHI). Atomic resolution electron energy loss spectroscopy (EELS) mapping and energy dispersive X-ray spectroscopy (EDX) were obtained to investigate the elements ordering and the position of fluorine element in the crystal structures of samples.

High-resolution X-ray powder diffraction data were collected at room temperature in Ar atmosphere, at the BL02B2 beamline at the SPring-8 (Hyogo, Japan). The diffractometer was equipped with six MYTHEN silicon micro-strip photon-counting detectors (Dectris Ltd., Baden, Switzerland), and the measurements were performed in Debye-Scherrer transmission geometry[46]. The incident beam energy was 30 keV. X-ray absorption spectra for Mn *K*-edge, La L_{III}-edge and Sr *K*-edge were obtained in the transmission/fluorescence mode using a Si(111) double crystal monochromator at BL01B1 and BL14B2 at SPring-8. For Mn/La and Sr, a pair of Rh mirrors with angles of 6 mrad and 2.8 mrad, respectively, were used to eliminate higher order harmonics. The samples were fixed in the laminate cell filled with Ar. X-ray absorption spectra for O/F *K*-edge and Mn *L*-edge were obtained in the fluorescence mode using a varied-line-spacing plane grating as a monochromator with Au mirror at C-branch of BL27SU at SPring-8. The measurements were conducted under vacuum and the samples were transferred from an Ar-filled glove box without exposure to air. Resonant inelastic X-ray scattering (RIXS) measurements were performed at BL07LSU in SPring-8 using a grazing flat-field type high resolution soft X-ray emission spectrometer[47]. The total energy resolution of the RIXS spectra $\Delta E_{tot} = \sqrt{\Delta E_{h\nu}^2 + \Delta E_{ana}^2}$ was approximately 150 meV, determined by fitting the elastic scattering from Cu plate. The energy resolution of the incident photon $\Delta E_{h\nu}$ is around 100 meV, so the energy resolution of the soft X-ray emission analyzer at 530 eV ΔE_{ana} is estimated to be around 110 meV. The loss energy of RIXS was calibrated as follows. First, the incident X-ray energy was set to 530 eV and 520 eV, the elastic peaks from a Cu plate at both energies were measured, and the emission energy of each elastic peak was determined to be 530 and 520 eV, respectively. The scaling between the two peaks was then calculated by a quadratic function derived from the optical design, and the conversion equation from the position on the detector to emission energy was obtained. As with the accuracy of the beamline photon energy, the accuracy of the absolute emission energy is about ±0.2 eV, but the relative accuracy is within ±0.5%. Here, the energy loss in RIXS is the energy difference from the elastic scattering, which means that the accuracy of the energy loss is within ±0.5%. The sample powders were supported on the carbon tape in the glovebox filled with Ar gas and transferred to the measurement chamber without exposure to atmosphere. The sample positions were changed at 2.4 μm/s during the RIXS measurements to avoid radiation damage.

2.2.5. First principle calculation

Density Functional theory (DFT) calculations were performed using the plane-wave basis projector augmented wave (PAW) method[48,49] implemented in the Vienna Ab-initio Simulation Package (VASP)[50–52]. Configurations of valence electrons in the PAW potentials are $5s^2$ $5p^6$ $4f^0$ $5d^1$ $6s^2$ for La, $4s^2$ $4p^6$ $5s^2$ for Sr, $3s^2$ $3p^6$ $3d^5$ $4s^2$ for Mn, $2s^2$ $2p^4$ for O, and $2s^2$ $2p^5$ for F. The exchange correlation potentials of electrons are treated by the PBEsol functional[53] and the on-site Coulomb (so-called $+U$) correction scheme[54] was additionally included for the strong correlation effect of Mn 3d electrons. The U value of Mn 3d in the PBEsol+U calculations was set at 3.0 eV[55]. The ***k***-points sampling in the Brillouin zones was based on Monkhorst–Pack scheme[56] with spacing between sampled ***k***-points in 0.3 $Å^{-1}$. The cell parameters and atomic positions were fully relaxed with an energy plane-wave cutoff of 550 eV until residual forces acting on each atom were less than 2.0×10^{-2} eV/Å. Optimized crystal structures are visualized using VESTA[57].

2.3. Results and Discussion

2.3.1. Electrochemical intercalation in rock-salt slabs of $La_{1.2}Sr_{1.8}Mn_2O_{7-\delta}F_x$ ($0 \leq x \leq 2$) oxyfluoride

A chemically fluorinated $La_{1.2}Sr_{1.8}Mn_2O_{7-\delta}F_2$ oxyfluoride was employed as a starting cathode active material. X-ray diffraction (XRD) data (**Fig. 2-1**) yielded tetragonal (*I*4/*mmm*) cell parameters of the starting $La_{1.2}Sr_{1.8}Mn_2O_7$ oxide and fluorinated $La_{1.2}Sr_{1.8}Mn_2O_7$ ($La_{1.2}Sr_{1.8}Mn_2O_{7-\delta}F_2$) in consistent with those reported[32]. Neutron diffraction data and Rietveld analysis results of the $La_{1.2}Sr_{1.8}Mn_2O_{7-\delta}F_2$ were shown in **Fig. 2-2** and **Table 2-1**, indicating that oxygen defects (δ ~0.46) form in the chemically fluorinated $La_{1.2}Sr_{1.8}Mn_2O_{7-\delta}F_2$ oxyfluoride. Scanning Transmission Electron

Microscope (STEM) and electron energy loss spectroscopy (EELS) for $La_{1.2}Sr_{1.8}Mn_2O_{7-\delta}F_2$ oxyfluoride revealed the fluorine insertion at the interstitial site in the rock-salt block (**Fig. 2-3, 2-4**). Observation by Scanning Electron Microscopy (SEM) show that the shape and size of the primary particles (1 ~ 3 μm) are retained after chemical fluorination (**Fig. 2-5**).

A cathode mixture was prepared by ball-milling $La_{1.2}Sr_{1.8}Mn_2O_{7-\delta}F_2$ oxyfluoride with $La_{0.9}Ba_{0.1}F_{2.9}$ and Vapor-Grown Carbon Fiber (VGCF), as often used in FIBs[36,37], and a three-electrodes cell was assembled using the mixture, with Pb wire as a reference electrode by inserting its tip into the solid electrolyte not to contact with each electrode layer. **Fig. 2-6a** shows discharge-charge profiles in a voltage range of –1.5~2.0 V at 10 mA/g. Upon initial discharge, the capacity reached 91.2 mAh/g, which is equivalent to the capacity of two fluoride ions (91.7 mAh/g) and suggests an almost complete fluoride ions extraction from $La_{1.2}Sr_{1.8}Mn_2O_{7-\delta}F_2$ oxyfluoride. Subsequent charge process yielded a capacity of 86.8 mAh/g, corresponding to a discharge-charge efficiency of 95.2%.

Structural changes in the cathode material during discharge-charge reactions were probed by *ex-situ* XRD (**Fig. 2-6b**). Upon discharge, the pristine $La_{1.2}Sr_{1.8}Mn_2O_{7-\delta}F_2$ oxyfluoride ($I4/mmm$) changes to $La_{1.2}Sr_{1.8}Mn_2O_{7-\delta}$ ($I4/mmm$; a = 3.842(2) Å, c = 20.25(2) Å), and upon charging, it changes to the original $La_{1.2}Sr_{1.8}Mn_2O_{7-\delta}F_2$ (a = 3.781(34) Å, c = 23.32(21) Å). No change of the diffraction peaks in $La_{0.9}Ba_{0.1}F_{2.9}$ is observed. HAADF–STEM images (**Fig. 2-6c**, **Fig. 2-7a**, **b**) and SAED patterns (**Fig. 2-7c**, **d**) of the $La_{1.2}Sr_{1.8}Mn_2O_{7-\delta}F_2$ oxyfluoride cathode after discharge and 1-cycle agree with the proposed structures. These observations verify a reversible electrochemical (de)intercalation in $La_{1.2}Sr_{1.8}Mn_2O_{7-\delta}F_x$ oxyfluoride ($0 \leq x \leq 2$) (**Fig. 2-8**). Atomic-resolution STEM–EELS mapping supported the insertion/extraction of fluoride ions, where fluoride ions are occupied at the interstitial site of the rock-salt slabs (**Fig. 2-9**). Moreover, the electrode $La_{1.2}Sr_{1.8}Mn_2O_{7-\delta}F_2$ oxyfluoride exhibited excellent cycle stability and rate capability (**Fig. 2-10**). It maintained capacity retention at 80% of the initial capacity after 50 cycles, with the coulombic discharge-charge efficiency of almost 100% during the cycles (**Fig. 2-10a**). Moreover, even at 100 mA/g, this electrode has a capacity of 60 mAh/g (corresponding to 65% of the discharge capacity at 10 mA/g, **Fig. 2-10b**). These properties are distinct from conversion-type active materials (e.g., CuF_2, BiF_3) whose capacity drops rapidly. The HAADF-STEM images after 50 cycles at charge state (**Fig. 2-10c, d**) resemble those of the pristine $La_{1.2}Sr_{1.8}Mn_2O_{7-\delta}F_2$ oxyfluoride, with no cracks in the active material or voids at the active/solid electrolyte interface in the electrode (**Fig. 2-10c**, **Fig. 2-7a, b**). It may be related to a smaller volume change of our material (10%) than reported cathode materials of FIBs (e.g., CuF_2 (193%), BiF_3 (49%), $LaSrMnO_4F_{2-x}$ (17%), $La_2CoO_4F_{2-x}$ (13%)).

2.3.2. Electrochemical further fluorination of $La_{1.2}Sr_{1.8}Mn_2O_{7-\delta}F_x$ oxyfluoride ($0 \leq x \leq 4$)

So far, we have demonstrated the excellent performance of electrochemical reactions for $La_{1.2}Sr_{1.8}Mn_2O_{7-\delta}F_x$ oxyfluoride ($0 \leq x \leq 2$). Although $La_{1.2}Sr_{1.8}Mn_2O_{7-\delta}F_2$ oxyfluoride is the terminal phase available via chemical fluorination[30, 32], recent studies on oxides for LIBs utilize oxygen redox chemistry to achieve extended capacity (e.g., $Li_2Ru_{0.75}Sn_{0.25}O_3$[5], $Li_{1.3}Nb_{0.3}Mn_{0.4}O_2$[9]). With this in mind, we attempted further fluorination by increasing the upper cut-off potential from 2.0 V (**Fig. 2-11**, **Fig. 2-12**).

When the electrochemical cell was charged to 3.0 V after the initial discharge (with a capacity equivalent to two fluoride ions), a wide plateau appeared at around 2.0 V and the total charge capacity reached about 250 mAh/g (**Fig. 2-12a**). The subsequent discharge process delivered a large capacity of 190 mAh/g, twice the capacity of the initial discharge process. This excess electrochemical fluorination is also topotactic; the XRD pattern of the 3.0 V charged $La_{1.2}Sr_{1.8}Mn_2O_{7-\delta}F_2$ oxyfluoride cathode is similar to that of the pristine cathode (**Fig. 2-12b**), and the ADF images of these cathodes show regular cation arrangements (**Fig. 2-14**). Furthermore, the atomic-resolution EELS mapping in the 3.0 V charged cathode (**Fig. 2-14**) shows an excess of fluoride ions in the perovskite block, in addition to the interstitial site in the rock-salt slabs. The XRD pattern of the 3.0 V charged cathode is close to that of the pristine $La_{1.2}Sr_{1.8}Mn_2O_{7-\delta}F_2$ oxyfluoride. The following discharge process led to the de-fluorinated $La_{1.2}Sr_{1.8}Mn_2O_{7-\delta}$, as confirmed by XRD and EELS (**Fig. 2-12b**, **Fig. 2-14**). Due to the inherent robustness of the perovskite-based structure, the volume of $La_{1.2}Sr_{1.8}Mn_2O_{7-\delta}F_2$ oxyfluoride changed reversibly between 1st charged and 1st discharged with an expansion of at most 6% (**Fig. 2-15**), which is smaller than the reported cathode materials of FIBs (e.g., CuF_2 (193%), BiF_3 (49%), $LaSrMnO_4F_{2-x}$ (17%)[36], $La_2CoO_4F_{2-x}$ (13%)[39]).

The capacity of each cycle provides about 200 mAh/g (four electrons reaction), and the capacity reversibility of the charge/discharge remains close to 100% as shown in **Fig. 2-16a**, except for the first discharge/charge process at 80% efficiency. The irreversible charge capacity on the 1st cycle may be attributed to multiple side reactions including the negligibly slight oxidation of the solid electrolyte $La_{0.9}Ba_{0.1}F_{2.9}$ (**Fig. 2-11**); slight fluorination of VGCF, which was confirmed by galvanostatic measurement and X-ray photoelectron spectroscopy (**Fig. 2-17**); and partial oxygen release, which is supported by Mn *L*-edge XAS discussed later, as seen in Li-excess metal oxide cathodes of LIBs[58, 59]. Discharge capacities increase gradually with the charge-discharge cycle and remain stable for at least 30 cycles without obvious decrease in capacity, and the reversible capacity amounts to 200 mAh/g. The average charge and discharge voltages during the 30 cycling were almost constant (**Fig. 2-18**).

The interfacial resistance between cathode and electrolyte ($R_{int, ca}$) measured by EIS was almost constant during cyclings (**Fig. 2-19**), indicating that the interface between cathode and electrolyte is stable without the generation of by-products. Moreover, our material with a fluorine content varying between x = 0 and 4 has a relatively high rate capability (200 mAh/g at 100 mA/g, **Fig. 2-16b**), which is significantly superior to the previous studies such as Sr_2MnO_3F[37] (17 mAh/g at 100 mA/g) and $Sr_3Fe_2O_5F_2$[38] (75 mAh/g at 100 mA/g). Apparent diffusion coefficient of fluoride ion (D_{F-}) for the $La_{1.2}Sr_{1.8}Mn_2O_{7-\delta}F_2$ oxyfluoride estimated by galvanostatic intermittent titration technique was 10^{-13}– 10^{-11} cm^2/s (**Fig. 2-20**), which is comparable to that of lithium ion for $LiCoO_2$ (10^{-12}– 10^{-11} cm^2/s)[60]. Therefore, the high rate capability of the $La_{1.2}Sr_{1.8}Mn_2O_{7-\delta}F_2$ oxyfluoride is possibly related to the rapid fluoride ion diffusion in the bulk. As shown in **Fig. 2-16c**, the obtained capacity is much higher than that of typical LIB cathode materials and, in terms of volumetric energy density, is comparable to that of recently investigated active materials using anion redox[5,9,61,62]. A full-cell with $La_{1.2}Sr_{1.8}Mn_2O_{7-\delta}F_2$ oxyfluoride cathode, $La_{2.9}Ba_{0.1}F_{2.9}$ and La foil used, respectively, as cathode, solid electrolyte and anode was tested for electrochemical performance. (**Fig. 2-21**) Although the current density of the full cell test was lower than that of the half-cell test, the full-cell exhibited similar charge/discharge curve's shape to the half-cell's one. Since the conditions of the cathode composite electrode are exactly the same for half cells and full cells, the relatively small current density (i.e. relatively large polarization) may be caused by the La foil anode due to the lack of optimization of the fabrication conditions. Although the fabrication conditions need to be improved, based on the active materials, the full cell showed a gravimetric energy density of 365 Wh kg^{-1}, which is close to a typical $LiCoO_2$/graphite cell (432 Wh kg^{-1}), and the volumetric energy density of 2156 Wh L^{-1} is considerably larger (vs. 1550 Wh L^{-1}) (**Table 2-2**).

2.3.3. Anionic redox reactions

The charge compensation mechanisms of (de)fluorination were examined by synchrotron hard/soft X-ray absorption spectroscopy (XAS). While the La *L* and Sr *K* absorption edges are unchanged, the energy of the Mn *K* absorption edge shifts to higher energies in the early stage of fluoride ion insertion ($x < 2$), but then remains unchanged in the later stage ($2 < x < 4$) (**Fig. 2-22**). A similar result was obtained from the energy change at the pre-edge peak (**Fig. 2-23**). The EXAFS analysis of the Mn *K*-edge for the first coordination shell (**Fig. 2-24**) shows that the bond length decreases up to $x = 2.4$ and then decreases only slightly up to $x = 4.8$. The change in the early stage of fluoride ion insertion reflects Mn oxidation, consistent with the Mn *K*-edge XANES results. In addition, the decrease in the intensity of the second-nearest-neighbor peak with the insertion of fluoride ions implies an increase in the Debye-Waller factor (i.e., increase in local distortion) of the Mn-La, Mn-Sr, and Mn-Mn bonds. The Mn *L*-edge spectrum of $La_{1.2}Sr_{1.8}Mn_2O_{7-\delta}F_2$ oxyfluoride (**Fig. 2-25a**) shifts to higher energy from $x = 0$ to $x = 2.0$ but not from $x = 2.0$ to $x = 4.8$, indicating that Mn ions are oxidized from Mn^{3+} to Mn^{4+} in the early process, but remain Mn^{4+} in the later process. After discharge, the Mn *L*-

edge spectrum (discharged) shifts to lower energy comparted to the sample of $x = 0$ (**Fig. 2-26**), indicating that Mn ions are reduced by partial oxygen release during the first charge/discharge process.

In the O *K*-edge spectrum, a broad peak, which is attributed to the transitions from the O 1*s* level to the hybridized states of the Mn 3*d* and O 2*p* orbitals[63, 64], was observed around 530 eV before charging ($x \sim 0$). The intensity at 529 eV increased in the early stage of fluoride ion insertion ($x < 2$) (**Fig. 2-25b**, **Fig. 2-27**), which is explained by the crystalline field stabilization energy via oxidation of Mn^{3+} (d^4, high spin) to Mn^{4+} (d^3). The same behavior is seen in the Mn *L*-edge spectra (**Fig. 2-25a**). On the other hand, further fluoride ion insertion beyond $x \sim 2$ resulted in the emergence of a new O *K*-edge peak at around 530.8 eV, and this peak increases its intensity with *x*, while it reversibly disappears upon fluoride ion extraction. The increase in the O *K*-edge peak and the unchanged oxidation of manganese for $2 < x < 4$ strongly suggests that oxidized oxygen species are involved in charge compensation, as observed in the lithium-rich cathodes[2,7,9,64]. Upon fluoride ion insertion beyond $x > 2$, the pre-edge region of F *K*-edge spectra (**Fig. 2-28**) exhibit a small peak that can be attributed to metal-fluorine bond[65], with its intensity increasing with *x*, suggesting the formation of Mn-F bonds in the perovskite blocks, as supported by STEM-EELS (**Fig. 2-14**). To examine the possibility of hole formation into Mn 3*d*-F 2*p* hybridized orbitals, we calculated the partial density of states (pDOS) of a $LaSr_2Mn_2O_7F_2$, which approximates the $La_{1.2}Sr_{1.8}Mn_2O_{7-\delta}F_2$ oxyfluoride, by first principles calculation, and found that only Mn 3*d* and O 2*p* orbitals exist near the Fermi level, with F 2*p* at a very low energy compared to these orbitals (**Fig. 2-29**). These results imply that hole formation does not occur in the F 2*p* orbital when excess fluoride ions are inserted into the cathode; the change in the F *K*-edge pre-edge may be due to the formation of a hole in the O 2*p* orbital, which changes the 3*d* orbital of the neighboring Mn, which in turn changes the F 2*p* orbital adjacent to Mn. To experimentally confirm the electronic structure of fluorine in the charged $La_{1.2}Sr_{1.8}Mn_2O_{7-\delta}F_x$ oxyfluoride cathode, it is useful to combine K-edge XANES and emission spectroscopy measurements of fluorine with RIXS measurements.[66] However, in this system, it is difficult to extract information from the above measurements because of the mixing of $La_{0.9}Ba_{0.1}F_{2.9}$ solid electrolyte at the composite electrode.

To further elucidate the nature of oxidized oxygen species, resonant inelastic X-ray scattering (RIXS) measurements from 528.5 to 533.0 eV in O *K*-edge XAS spectra were performed in vacuum (**Fig. 2-30**). The obtained RIXS spectra at 530.8 eV (**Fig. 2-31**) exhibited discrete energy-loss peaks around the elastic line from 5 to 0 eV, representing several vibrational levels of the ground state potential energy surface[67]. The frequency of the first vibrational level was 1591 cm^{-1}, similar to the molecular O_2 (approximately 1600 cm^{-1}), which has recently been observed in charged $Na_{0.75}[Li_{0.25}Mn_{0.75}]O_2$ and $Li_{1.2}Ni_{0.13}Co_{0.13}Mn_{0.54}O_2$ during charge process by RIXS under vacuum[2,3]. Since inorganic $La_{0.9}Ba_{0.1}F_{2.9}$ was used for the electrolyte in this study, the O–O species cannot be formed by side reactions between cathode and organic electrolyte[68]. The additional features in the 1-2 eV range are not due to the presence of PDOS but rather result from the intensity modulation of the vibrational progression caused by lifetime vibrational interference[67, 69–71]. This result indicates that O–O bond is formed in charged $La_{1.2}Sr_{1.8}Mn_2O_{7-\delta}F_2$ oxyfluoride. After discharge, this vibration disappears, which means that the O–O bond formation/breaking is reversible. It appears that the O-O bond formation not only accounts for charge compensation (anion redox), but also creates additional vacancies for excess fluoride ions to be filled. Assuming the O-O bond formation as expected from the RIXS result, charge compensation of two electrons adds 0.5 vacancy sites ($O^{2-} \rightarrow 1/2O_2 + 2e^-$), a significant amount of fluoride ions should be occupied at irregular anion sites. We tried to determine the structure of the charged-$La_{1.2}Sr_{1.8}Mn_2O_{7-\delta}F_2$ oxyfluoride cathode during O–O bond formation using microscopic analysis of ABF-STEM (**Fig. 2-32**). Clear image to determine the structure was not obtained probably because the structure is highly distorted. Galvanostatic intermittent titration technique (**Fig. 2-33**) showed that polarization and hysteresis of open-circuit-voltage are larger for $x > 2$ than $0 < x < 2$ and the larger polarization for $x > 2$ may be caused by the formation of oxygen-oxygen bond that could involve local distortions. A similar non-negligible polarization has been observed in the compound including the formation of oxygen molecules associated with the electrochemical deintercalation of sodium ions[3].

The XRD pattern of the fully charged-$La_{1.2}Sr_{1.8}Mn_2O_{7-\delta}F_2$ oxyfluoride hardly changed from the pristine $La_{1.2}Sr_{1.8}Mn_2O_{7-\delta}F_2$ oxyfluoride (**Fig. 2-12b**), which may be due to the following two reasons. One is due to the fact that the fluoride ion insertion site has changed from a two-dimensional interlattice position in the rock-salt phase to a random site associated with the O–O bond formation site in the perovskite layer. It has also been reported for LIBs that the lattice volume change is very small in the insertion and extraction of lithium ions into random percolation sites in the rock salt structure compared to the lattice volume expansion associated with the insertion and extraction of lithium ions into the two-dimensional layered rock salt oxide cathode (e.g. layered

$LiCoO_2$ (3.6%)[72], cation disordered rocksalt $Li_{1.25}Nb_{0.25}V_{0.5}O_2$ oxide (1%)[73] and $Li_{1.25}V_{0.55}Nb_{0.2}O_{1.9}F_{0.1}$ oxyfluoride (0.7%)[74]. This is due to the larger Coulomb attraction/repulsion forces associated with insertion/extraction into two-dimensional sites. The other is due to the introduction of holes into the 2*p* orbitals of oxygen, i.e., the ionic radii of the oxide ions becoming small as they are oxidized. As noted above, although how the O–O bond formed and excess fluoride ion are present in the charged $La_{1.2}Sr_{1.8}Mn_2O_{7-\delta}F_2$ oxyfluoride is not clear, these results indicate that the molecular-like O_2 and excess fluoride ion may be present in some cavities in the structure, as found in the lithium-rich cathode material[2] or the N_2-intercalated WO_3[75], and the formation of molecular-like O_2 may have created the irregular site of fluoride ion.

2.4. Conclusion

We demonstrated electrochemical intercalation of fluoride ions with excellent reversibility, cyclability and rate capability, using the double-layered Ruddlesden-Popper type perovskite oxyfluoride $La_{1.2}Sr_{1.8}Mn_2O_{7-\delta}F_x$. Interestingly, in addition to the conventional Mn redox at $0 < x < 2$, this oxyfluoride can incorporate excess fluoride ions ($2 < x < 4$) into the perovskite blocks by forming O–O (anion redox). Although the $La_{1.2}Sr_{1.8}Mn_2O_{7-\delta}F_x$ shows high capacity by using O–O bond formation, the capacity is still comparable to Li-excess metal oxide cathodes. Therefore, development of new cathodes with higher capacity than the $La_{1.2}Sr_{1.8}Mn_2O_{7-\delta}F_x$ by using same reaction mechanism. It should be emphasized that, like the LIBs, the current FIBs have room for further improvement in terms of electrochemical properties such as cycle stability, rate characteristics, and fluoride ion diffusion; available strategies include chemical substitution with other transition metals, oxygen vacancy control, optimization of composition in an electrode mixture, tuning particle morphologies and controlling interfacial contact between electrode and electrolyte. The battery performance was measured at 140°C this time mainly because of the low fluoride ion conductivity of the solid electrolyte used. Therefore, development of new solid electrolyte with high ionic conductivity and electrochemical window is necessary. Given the variety of structures and compositions known for conventional perovskite materials, the ability to capture excess fluorine ion through the formation of O–O bond adds a new dimension to perovskite engineering not only for battery research but also for other disciplines. In fact, formation of molecular-like O_2 in perovskite ABO_3 with the 'closed packed' structure is not obvious and could be an interesting research topic in general. Furthermore, this study sufficiently raises awareness that electrochemistry is a powerful tool for obtaining novel oxyfluorides and, more generally, mixed-anion compounds[76] that could have an impact on a variety of physical and chemical functions.

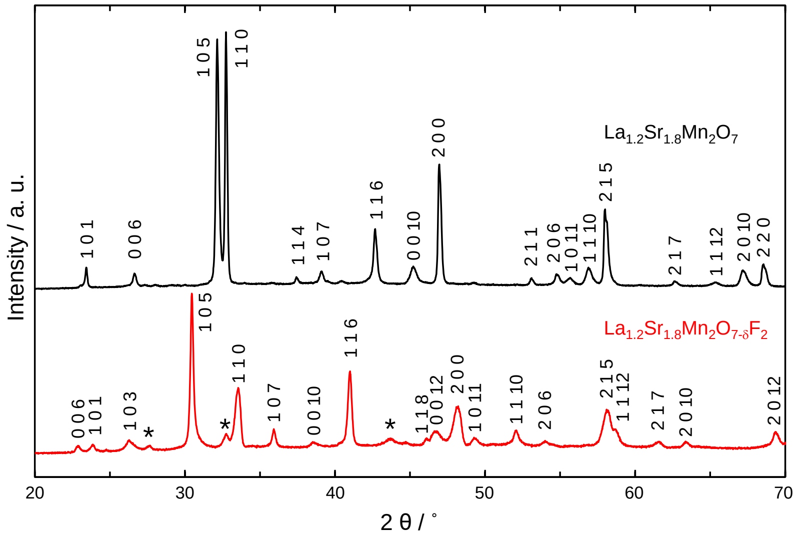

Fig. 2-1. X-ray diffraction patterns of (upper) as-prepared $La_{1.2}Sr_{1.8}Mn_2O_7$ and (lower) $La_{1.2}Sr_{1.8}Mn_2O_{7-δ}F_2$. $La_{1.2}Sr_{1.8}Mn_2O_{7-δ}F_2$ was prepared by chemical fluorination of $La_{1.2}Sr_{1.8}Mn_2O_7$ using polyvinylidene difluoride. Asterisks denote an unidentified impurity. The lattice constants are $a = 3.88065(7)$ Å, $c = 20.1203(4)$ Å for $La_{1.2}Sr_{1.8}Mn_2O_7$ and $a = 3.7956(3)$ Å, $c = 23.349(2)$ Å for $La_{1.2}Sr_{1.8}Mn_2O_{7-δ}F_2$.

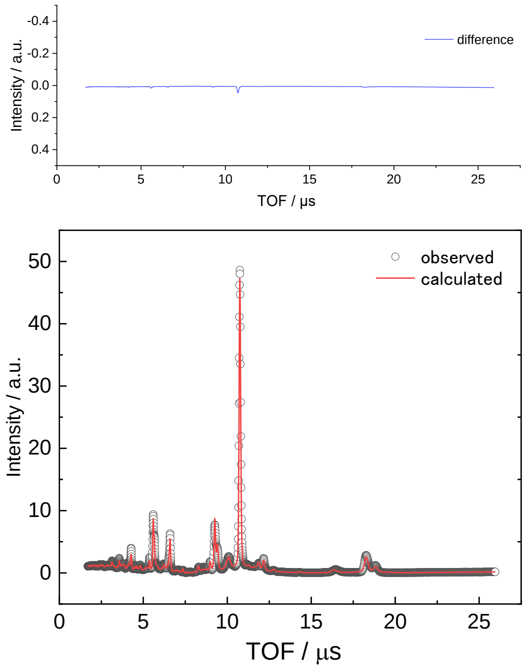

Fig. 2-2. Rietveld analysis results of $La_{1.2}Sr_{1.8}Mn_2O_{7-δ}F_2$ oxyfluoride. Observed (circle), calculated (red line), and difference (observed minus calculated), which is located at the top of the figure in blue.

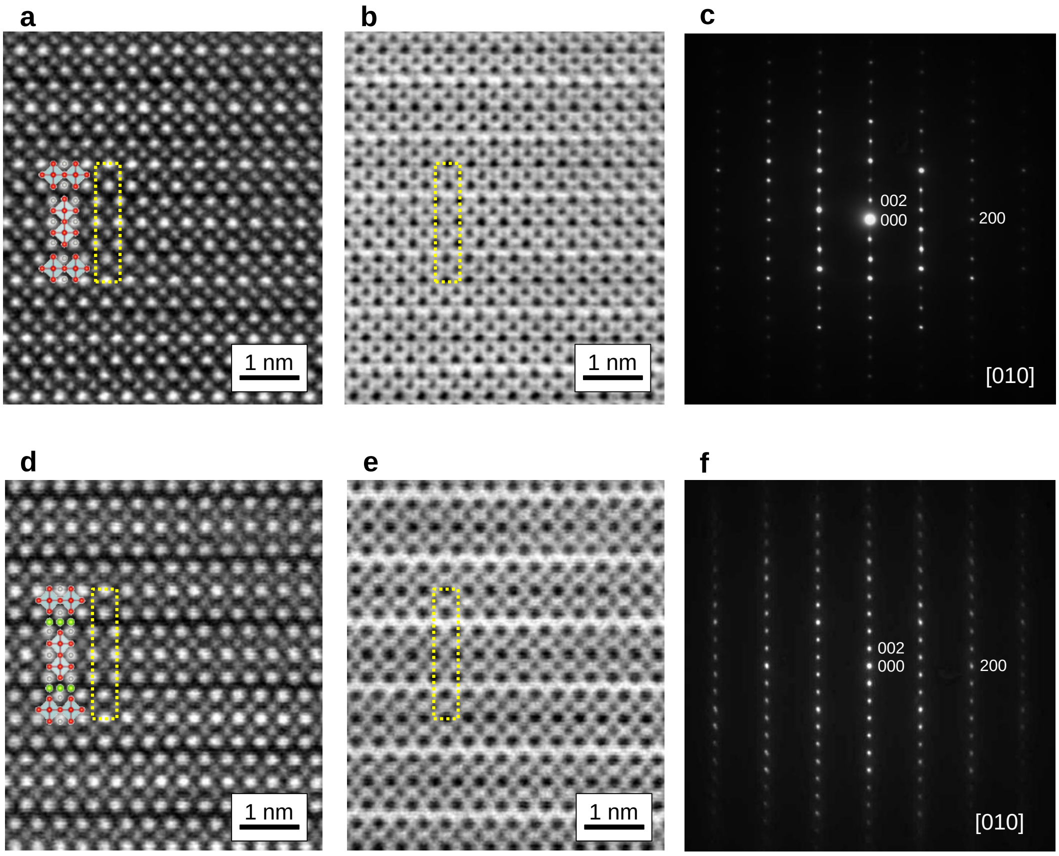

Fig. 2-3. Spherical Aberration (Cs) corrected Scanning Transmission Electron Microscope (Cs-STEM) observations. **a, b, c,** $La_{1.2}Sr_{1.8}Mn_2O_7$ oxide and **d, e, f,** $La_{1.2}Sr_{1.8}Mn_2O_{7-\delta}F_2$ oxyfluoride. **a, d,** High-magnification images of high-angle annular dark-field (HAADF) observation. **b, e,** High-magnification images of annular bright-field (ABF) observation. **c, f,** Selected-area electron diffraction (SAED) patterns. These observations were viewed along [010]. The insets of **a, d,** the ideal structures of $La_{1.2}Sr_{1.8}Mn_2O_7$ oxide and $La_{1.2}Sr_{1.8}Mn_2O_{7-\delta}F_2$ oxyfluoride. The ideal structures are shown for simplicity.

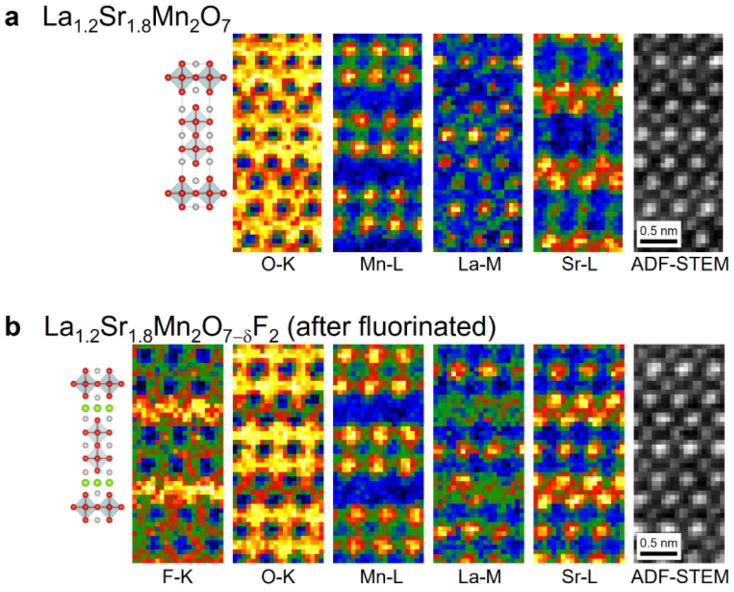

Fig. 2-4. Atomic resolution STEM-EELS mapping images of La$_{1.2}$Sr$_{1.8}$Mn$_2$O$_7$ oxide and La$_{1.2}$Sr$_{1.8}$Mn$_2$O$_{7-\delta}$F$_2$ oxyfluoride. **a,** La$_{1.2}$Sr$_{1.8}$Mn$_2$O$_7$ oxide and **b,** fluorinated La$_{1.2}$Sr$_{1.8}$Mn$_2$O$_{7-\delta}$F$_2$ oxyfluoride, viewed along [010], where the ideal structures are shown for simplicity.

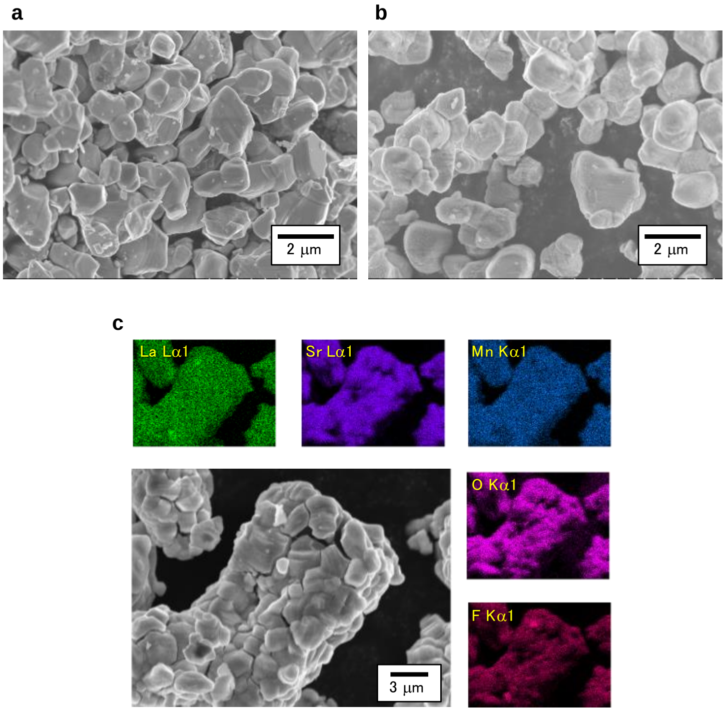

Fig. 2-5. SEM observation and SEM-EDX mapping of La$_{1.2}$Sr$_{1.8}$Mn$_2$O$_7$ and La$_{1.2}$Sr$_{1.8}$Mn$_2$O$_{7-\delta}$F$_2$. SEM images of **a,** La$_{1.2}$Sr$_{1.8}$Mn$_2$O$_7$ and **b,** La$_{1.2}$Sr$_{1.8}$Mn$_2$O$_{7-\delta}$F$_2$. **c,** SEM-EDX mapping of La$_{1.2}$Sr$_{1.8}$Mn$_2$O$_{7-\delta}$F$_2$.

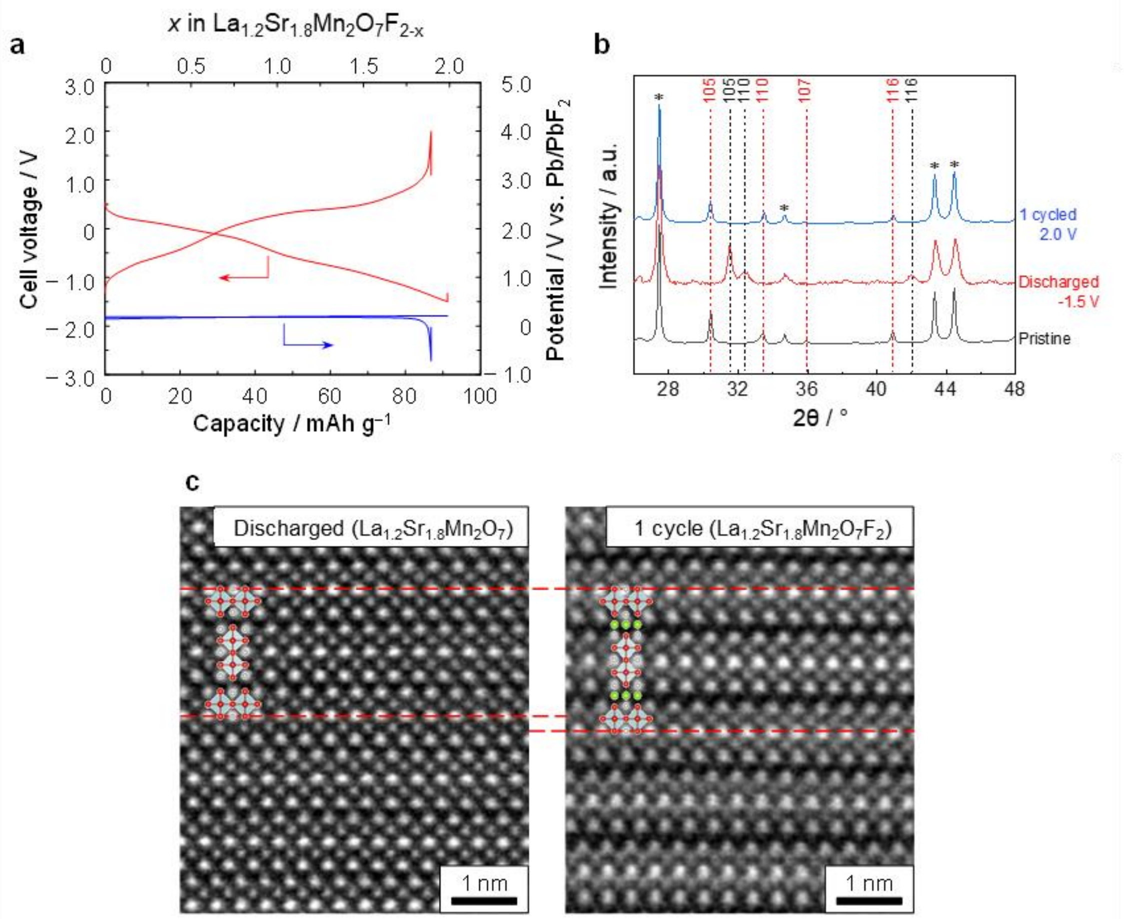

Fig. 2-6. Electrochemical performance of La$_{1.2}$Sr$_{1.8}$Mn$_2$O$_{7-\delta}$F$_2$ oxyfluoride and structural changes after discharge/charge process. **a**, Discharge/charge curves at a rate of 10 mA/g at 140 ˚C, where red and blue lines show, respectively, cell voltage and potential of counter electrode. **b**, XRD patterns of cathode composites containing La$_{1.2}$Sr$_{1.8}$Mn$_2$O$_{7-\delta}$F$_2$ oxyfluoride before and after galvanostatic discharge/charge. Red and black broken lines are peaks of La$_{1.2}$Sr$_{1.8}$Mn$_2$O$_{7-\delta}$F$_2$ oxyfluoride and La$_{1.2}$Sr$_{1.8}$Mn$_2$O$_7$, respectively. Asterisk marks La$_{0.9}$Ba$_{0.1}$F$_{2.9}$ (solid electrolyte). **c**, High-angle annular dark-field (HAADF) STEM images of La$_{1.2}$Sr$_{1.8}$Mn$_2$O$_{7-\delta}$F$_2$ oxyfluoride after discharge and 1 cycle viewed along [010].

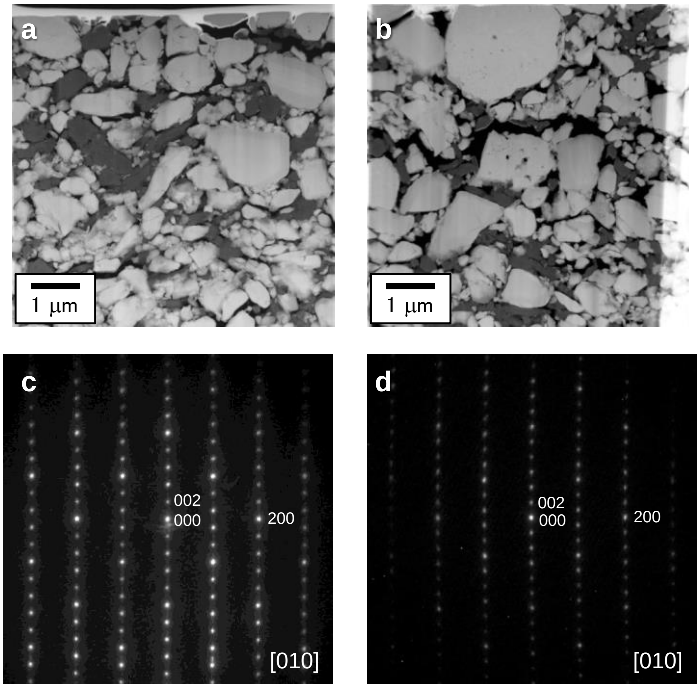

Fig. 2-7. Cs-STEM observation of $La_{1.2}Sr_{1.8}Mn_2O_{7-\delta}F_2$ oxyfluoride at discharge state and after 1 cycle. **a, b**, Low-magnification images of samples: a, discharged $La_{1.2}Sr_{1.8}Mn_2O_{7-\delta}F_2$ oxyfluoride and b, 1-cycled $La_{1.2}Sr_{1.8}Mn_2O_{7-\delta}F_2$ oxyfluoride. **c, d**, SAED patterns of samples: c, discharged $La_{1.2}Sr_{1.8}Mn_2O_{7-\delta}F_2$ (a = 3.90 Å, c = 20.6 Å) and d, 1-cycled $La_{1.2}Sr_{1.8}Mn_2O_{7-\delta}F_2$ oxyfluoride (a = 3.78 Å, c = 23.2 Å). These observations were viewed along [010].

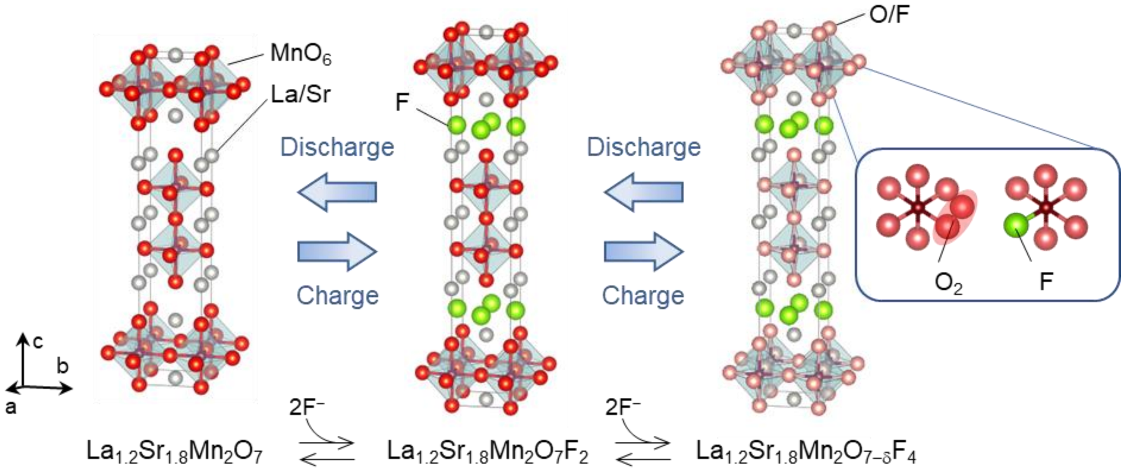

Fig. 2-8. Discharge/charge scheme of $La_{1.2}Sr_{1.8}Mn_2O_{7-\delta}F_2$ oxyfluoride. It has not been clear where O–O bond and excess fluoride ions are in the charged $La_{1.2}Sr_{1.8}Mn_2O_{7-\delta}F_2$ oxyfluoride

a Pristine ($La_{1.2}Sr_{1.8}Mn_2O_{7-\delta}F_2$)

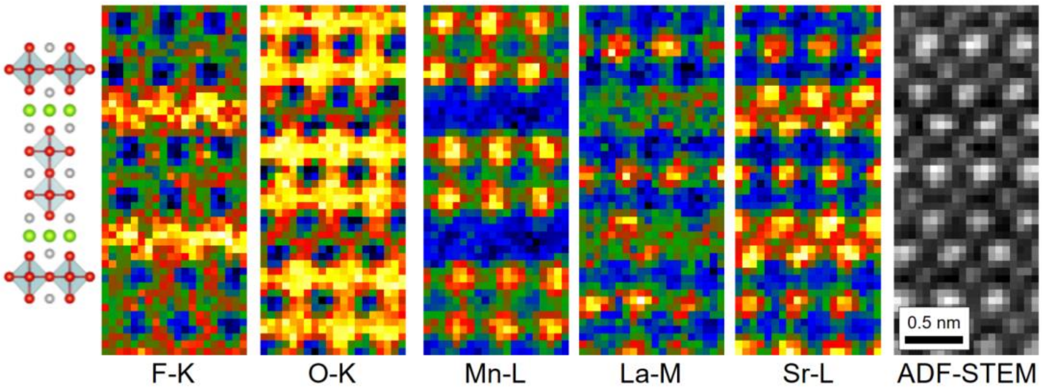

b After 1 cycle ($La_{1.2}Sr_{1.8}Mn_2O_{7-\delta}F_2$)

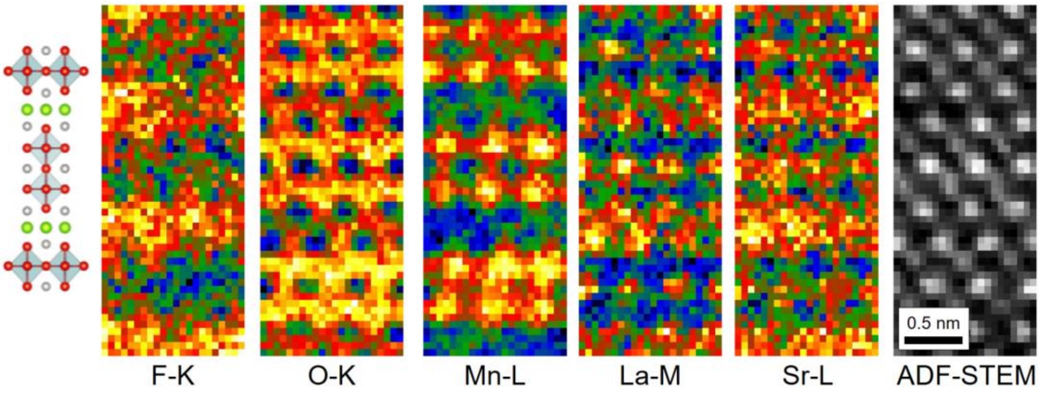

Fig. 2-9. Atomic resolution STEM-EELS mapping images of $La_{1.2}Sr_{1.8}Mn_2O_{7-\delta}F_2$ oxyfluoride active material in the electrodes. **a**, Pristine $La_{1.2}Sr_{1.8}Mn_2O_{7-\delta}F_2$ oxyfluoride and **b**, $La_{1.2}Sr_{1.8}Mn_2O_{7-\delta}F_2$ oxyfluoride after 1-cycle, viewed along [010]. For simplicity, the ideal structures are shown. It is possible that a partial anion (F^-/O^{2-}) mixing occurs in the perovskite blocks after the electrochemical process. The mixing of the anion sites by oxide and fluoride anions sometimes makes the oxyfluoride energetically more stable, as in $Sr_3Fe_2O_{5.44}F_{1.56}$, $Pb_2Ti_2O_{6-\delta}F_{2\delta}$, and $Ag_3Mo(O_3F_3)$.

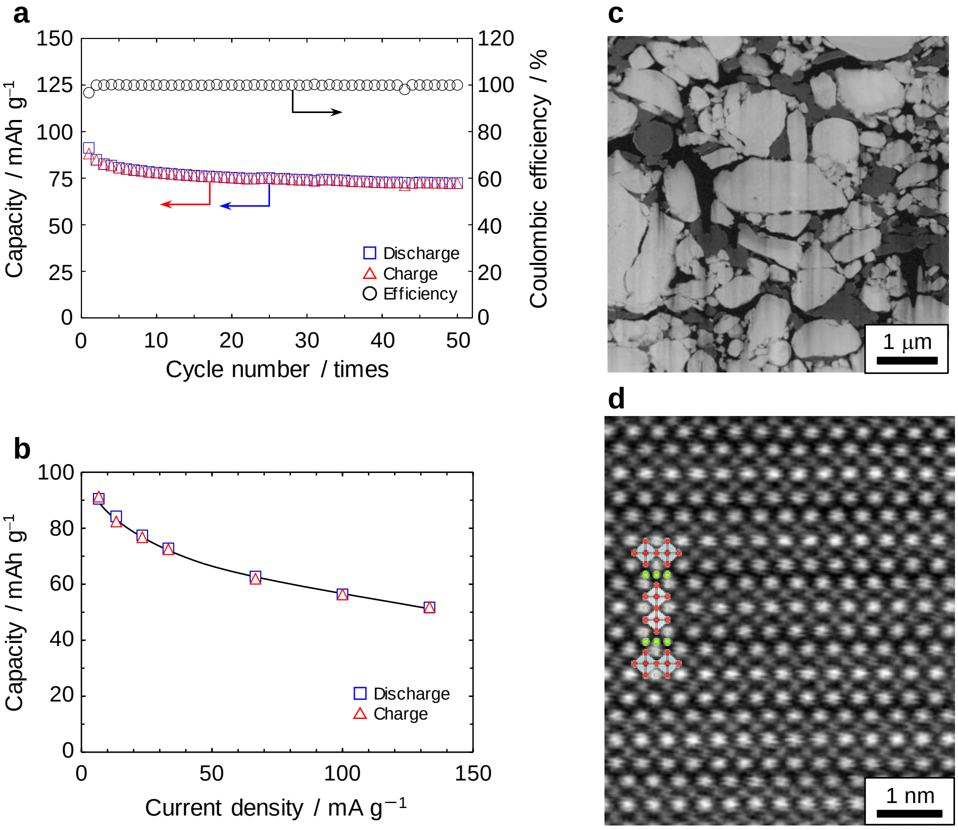

Fig. 2-10. Cycle stability and rate performance of $La_{1.2}Sr_{1.8}Mn_2O_{7-\delta}F_2$ oxyfluoride. **a**, Cycle performance of the discharge and charge capacities and the efficiencies. The efficiencies are estimated by dividing charge capacities by discharge capacities in the same cycle. **b**, Rate capability of $La_{1.2}Sr_{1.8}Mn_2O_{7-\delta}F_2$ oxyfluoride, which was charged to 2.0 V at different rates and then discharged to –1.5 V at the same rate as the charge process. **c, d**, HAADF-STEM images of charged $La_{1.2}Sr_{1.8}Mn_2O_{7-\delta}F_2$ oxyfluoride after 50 cycles, viewed along [010]. The ideal structures are shown for simplicity.

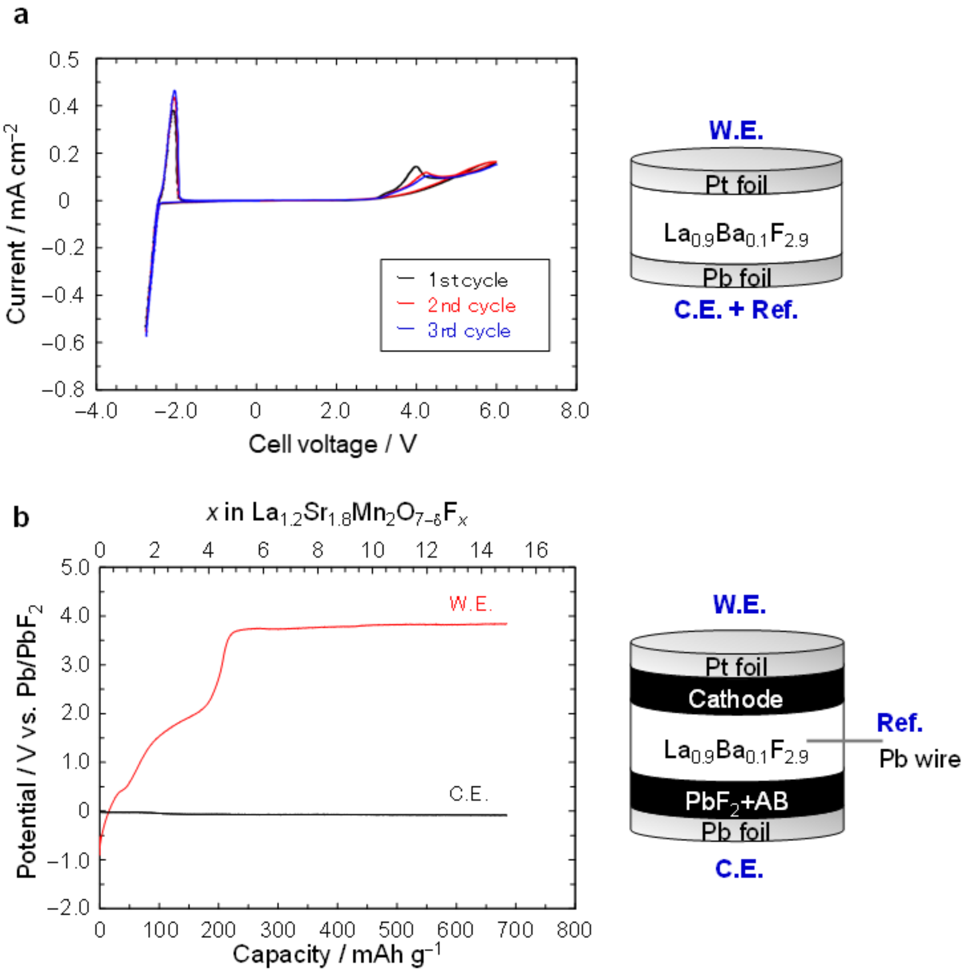

Fig. 2-11. Electrochemical stability of $La_{0.9}Ba_{0.1}F_{2.9}$ as a solid electrolyte. **a**, Cyclic voltammetry curves of $La_{0.9}Ba_{0.1}F_{2.9}$ in the potential window between –2.8 V to 6.0 V at the rate of 1.0 mV s^{-1}. **b**, Charge profiles of cathode composite, composed of $La_{1.2}Sr_{1.8}Mn_2O_{7-\delta}F_2$ oxyfluoride, $La_{0.9}Ba_{0.1}F_{2.9}$ and VGCF, after initial discharge to –1.5 V at a rate of 10 mA/g at 140 ˚C. In **Fig. 2-11a,** redox currents attributed to La metal deposition/dissolution reactions were observed at -2.5 V (vs. Pb) and the current attributed to oxidation of the $La_{0.9}Ba_{0.1}F_{2.9}$ was observed above 3.05 V (vs. Pb). In the galvanostatic measurement by using three-electrode cell (**Fig. 2-11b**), a potential plateau was observed at 3.7 V (vs. Pb/PbF$_2$) even when the capacity of cathode reached over 600 mA/g. This potential plateau may be attributed to oxidation of the $La_{0.9}Ba_{0.1}F_2$. Therefore, the electrochemical measurements of $La_{1.2}Sr_{1.8}Mn_2O_{7-\delta}F_2$ oxyfluoride and $La_{1.2}Sr_{1.8}Mn_2O_7$ oxide cathode were performed within –1.5 ~ 3.0 V (vs. Pb), in which the $La_{0.9}Ba_{0.1}F_{2.9}$ does not undergo the reactions.

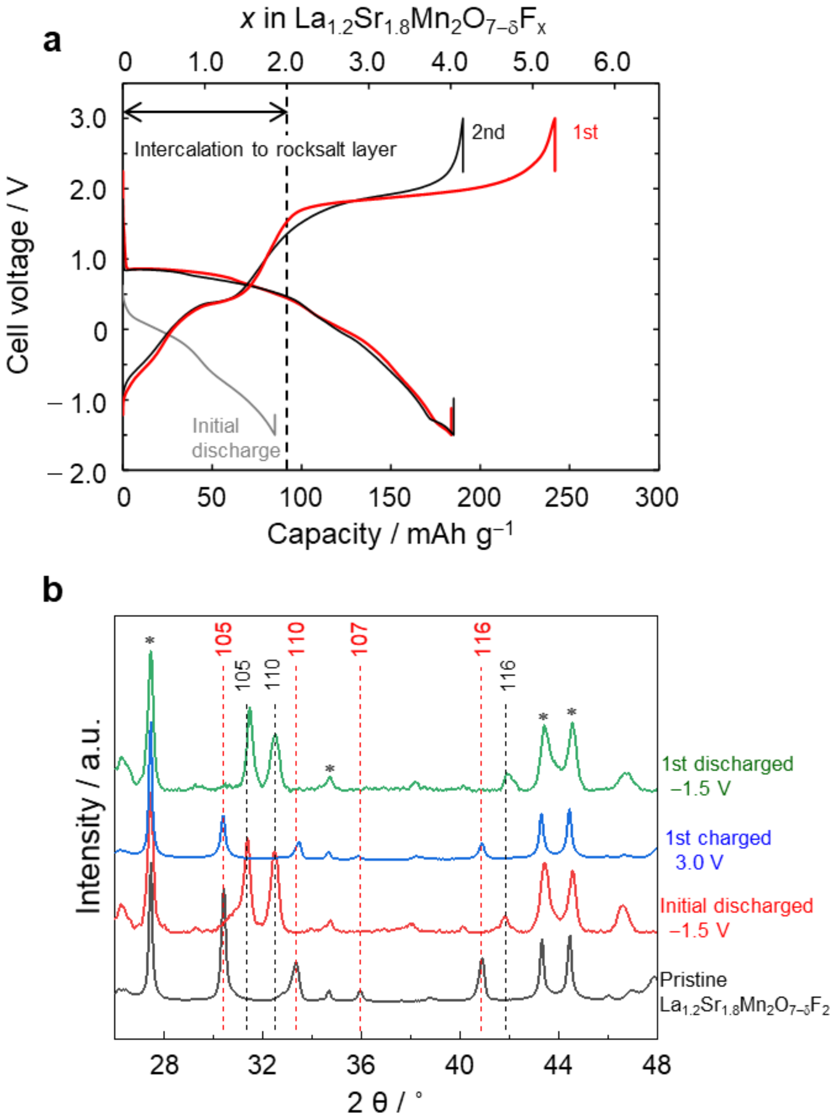

Fig. 2-12. Charge/discharge properties and structural changes of $La_{1.2}Sr_{1.8}Mn_2O_{7-\delta}F_2$ oxyfluoride upon charging at higher potential. **a**, Charge/discharge curves at a rate of 10 mA/g at 140 ˚C, where PbF_2/AB composite was included in the anode side between solid electrolyte and Pb foil as a fluorine source. **b**, XRD patterns of cathode composites containing $La_{1.2}Sr_{1.8}Mn_2O_{7-\delta}F_2$ oxyfluoride before and after galvanostatic charge/discharge. Red and black broken lines correspond, respectively, to $La_{1.2}Sr_{1.8}Mn_2O_{7-\delta}F_2$ oxyfluoride and $La_{1.2}Sr_{1.8}Mn_2O_7$. Asterisks denote $La_{0.9}Ba_{0.1}F_{2.9}$ electrolyte. Note that in order to obtain clearer diffraction peaks for $La_{1.2}Sr_{1.8}Mn_2O_{7-\delta}F_2$ oxyfluoride, we used a cathode composite with higher active material content (~60 wt%) (**Fig. 2-13**).

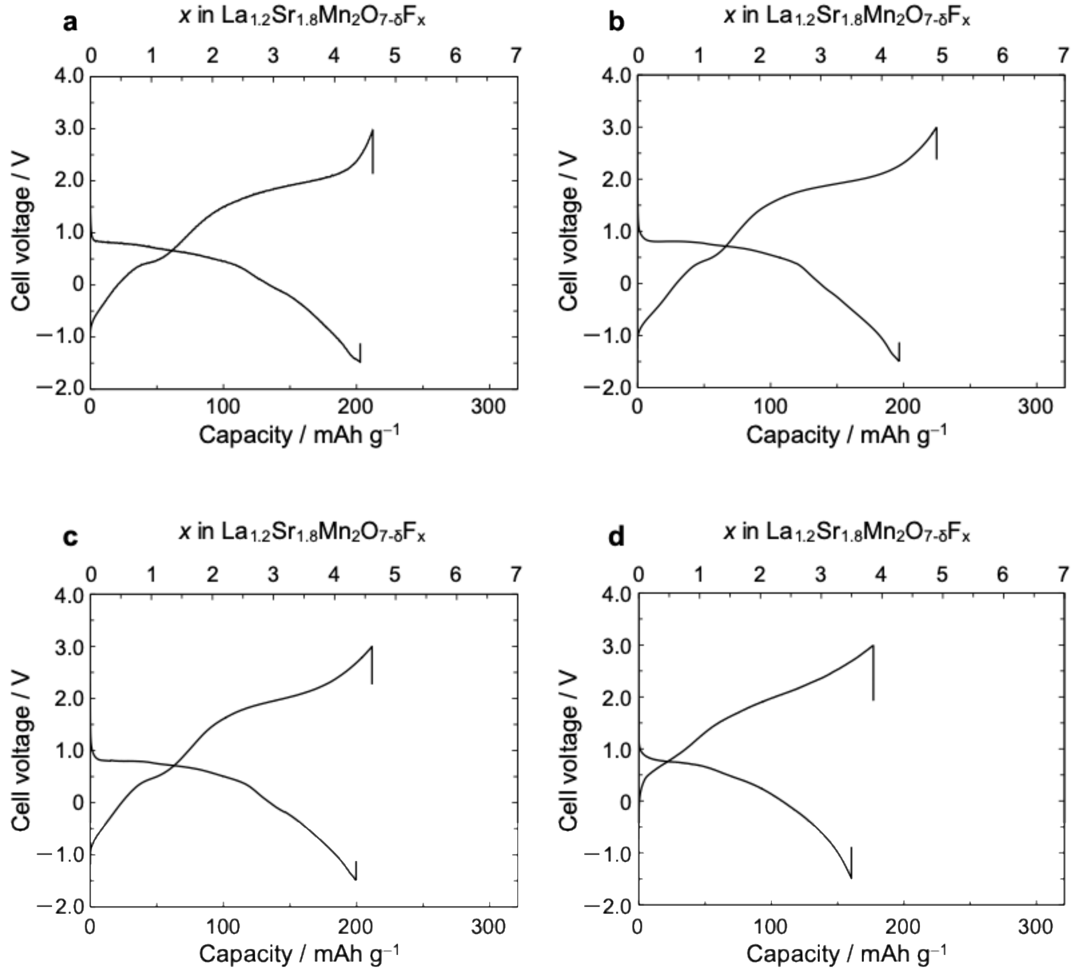

Fig. 2-13. Charge/discharge profiles of $La_{1.2}Sr_{1.8}Mn_2O_{7-\delta}F_2$ oxyfluoride upon charging at higher potential with various active material content. Charge/discharge curve of $La_{1.2}Sr_{1.8}Mn_2O_{7-\delta}F_2$ oxyfluoride cathode mixture, composed of the active material, $La_{0.9}Ba_{0.1}F_{2.9}$ and VGCF in the weight ratio of **a**; 30:60:10, **b**; 50:43:7, **c**; 60:34:6, **d**; 70:25:5. 10 mg of the cathode composites were introduced, and PbF_2/AB composite was also introduced in the anode side between solid electrolyte and Pb foil as a fluorine source. All cells were first discharged/charged between –1.5 V and 1.5 V for 3 cycles and then examined between –1.5 V and 3.0 V at a current rate of 30 μA cm^{-2} at 140 ˚C.

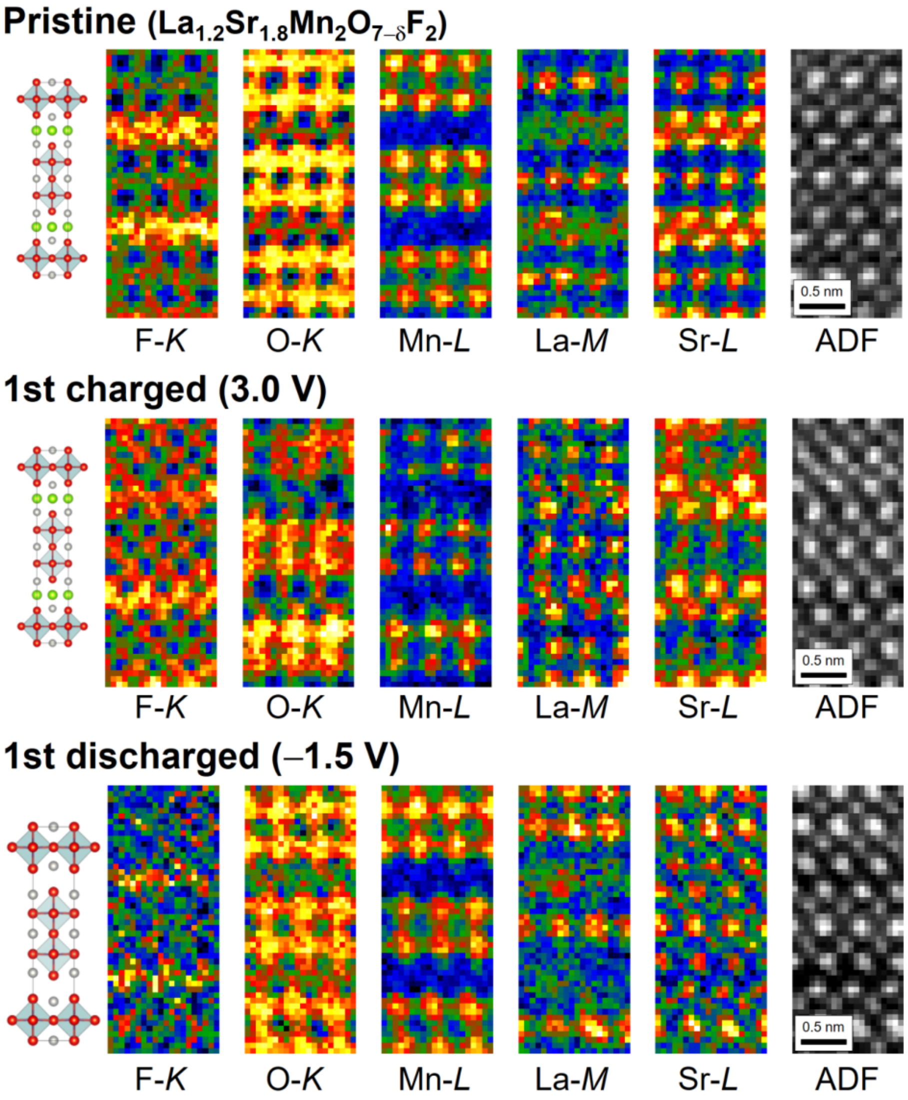
Pristine ($La_{1.2}Sr_{1.8}Mn_2O_{7-\delta}F_2$)

1st charged (3.0 V)

1st discharged (–1.5 V)

Fig. 2-14. Atomic resolution STEM-EELS mapping images of $La_{1.2}Sr_{1.8}Mn_2O_{7-\delta}F_2$ oxyfluoride before and after galvanostatic charge/discharge along [010]. For simplicity, the ideal structures are shown[57].

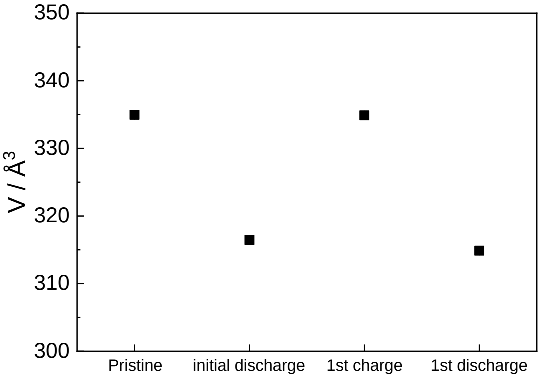

Fig. 2-15. The lattice volume change of the $La_{1.2}Sr_{1.8}Mn_2O_{7-\delta}F_2$ oxyfluoride during 1st cycling in the voltage range between –1.5 V and 3.0 V. The data includes error bars, which are smaller than the symbols and not visible.

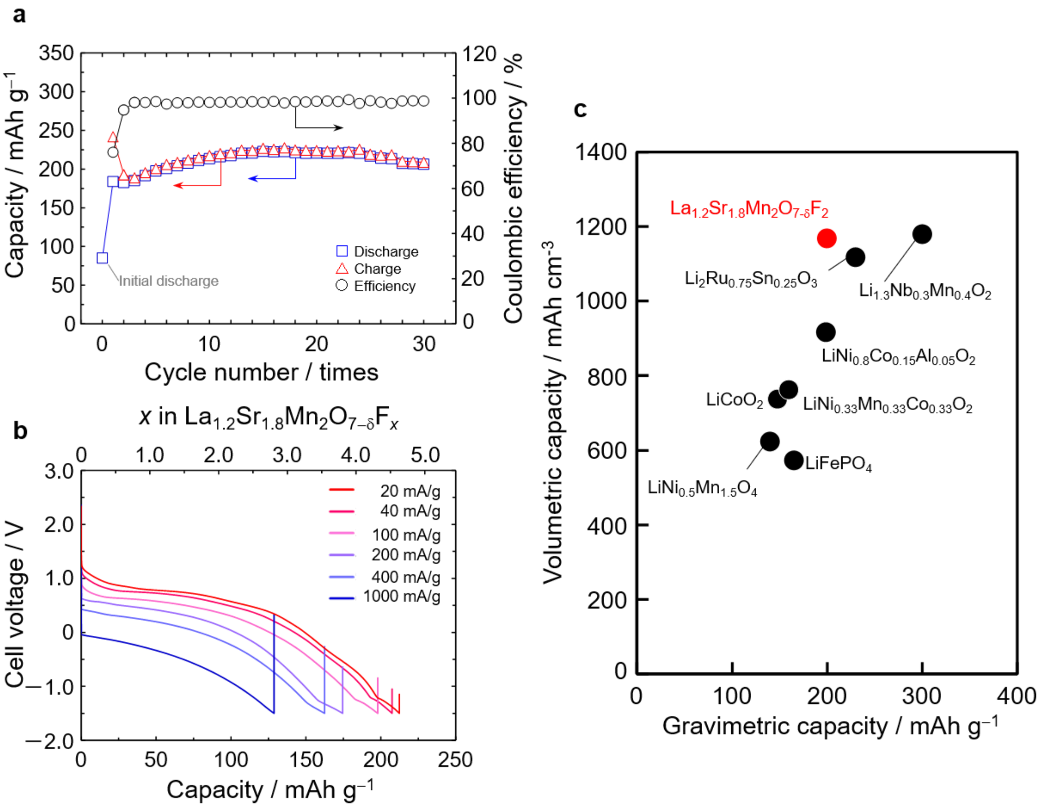

Fig. 2-16. Electrochemical properties of $La_{1.2}Sr_{1.8}Mn_2O_{7-\delta}F_2$ oxyfluoride upon further fluorination. **a**, Cycle performance of discharge/charge capacities and the efficiency. The efficiency was calculated as follows: the *n*-th discharge capacity divided by the *n*-th charge capacity. **b**, Discharge curves with different current rates for $La_{1.2}Sr_{1.8}Mn_2O_{7-\delta}F_2$ oxyfluoride after 15 cycles. The same conditions were adopted for charging, with an upper limit potential of 3.0 V and a current rate of 10 mA/g. **c**, Plots of the volumetric/gravimetric capacities for $La_{1.2}Sr_{1.8}Mn_2O_{7-\delta}F_2$ oxyfluoride and cathode materials reported in LIBs[5,9,61,62].

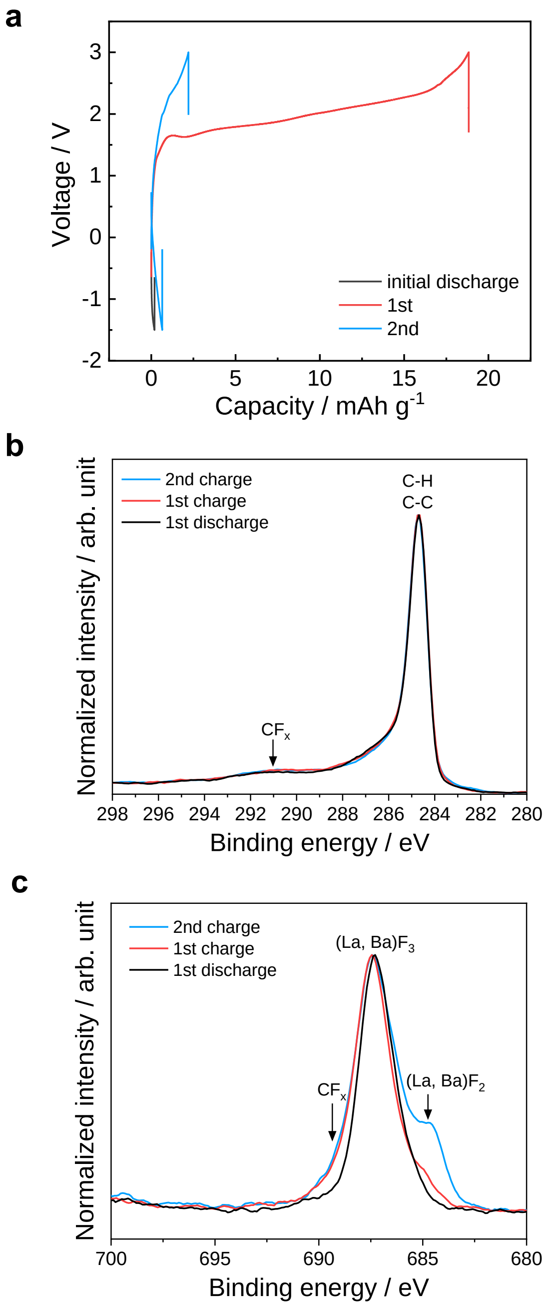

Fig. 2-17. a, Charge/discharge curves of a composite electrode consisting only of VGCF and La$_{0.9}$Ba$_{0.1}$F$_{2.9}$ in a weight ratio of 60:10, at a rate of 10 mA/g at 140℃. XPS spectra of **b**, C 1s and **c**, F 1s for the VGCF composite electrode after charge/discharge measurements.

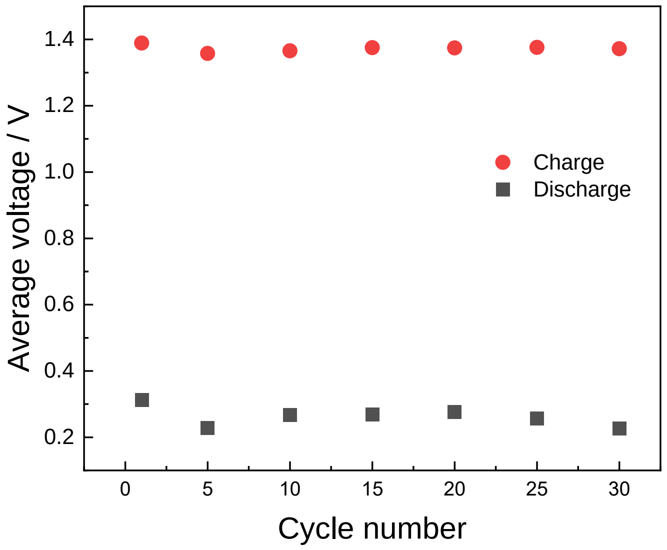

Fig. 2-18. The average voltage of the $La_{1.2}Sr_{1.8}Mn_2O_{7-\delta}F_2$ oxyfluoride cathode during 30 charge/discharge cycling.

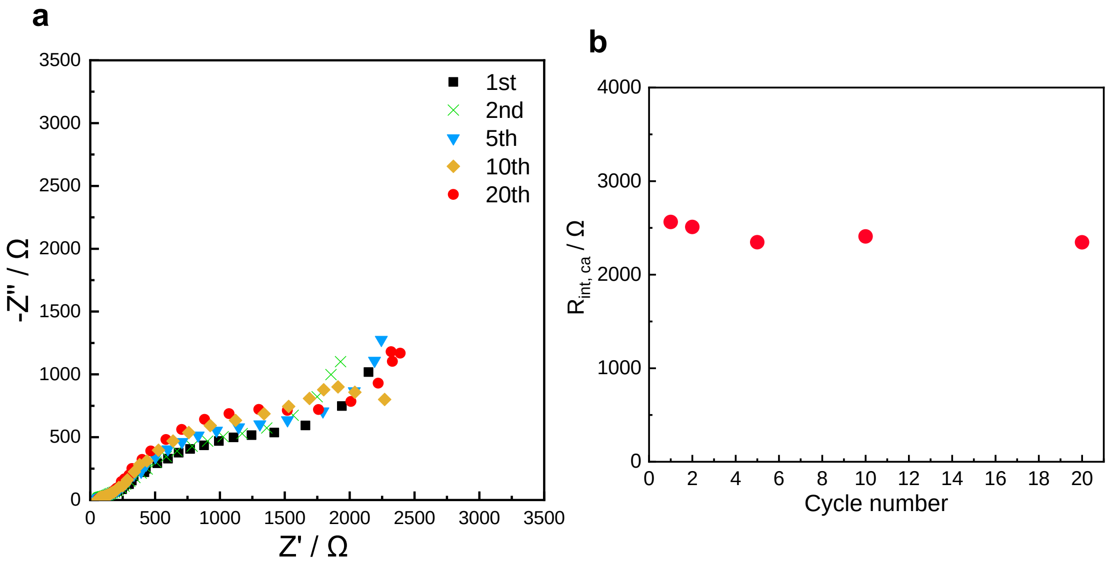

Fig. 2-19. a, The Nyquist plots of the $La_{1.2}Sr_{1.8}Mn_2O_{7-\delta}F_2$ cathode at discharged state during several cyclings, **b,** the interfacial resistance between cathode and electrolyte ($R_{int, ca}$) during charge/discharge cycling. The small and large semicircles in high and low frequency region were assigned to the interfacial resistances between anode and electrolyte interface ($R_{int, an}$), and $R_{int, ca}$, respectively because the fitted capacitance values with an equivalent circuit were around 10^{-6} –10^{-5} μF and the $R_{int, an}$ should be smaller than the $R_{int, ca}$.

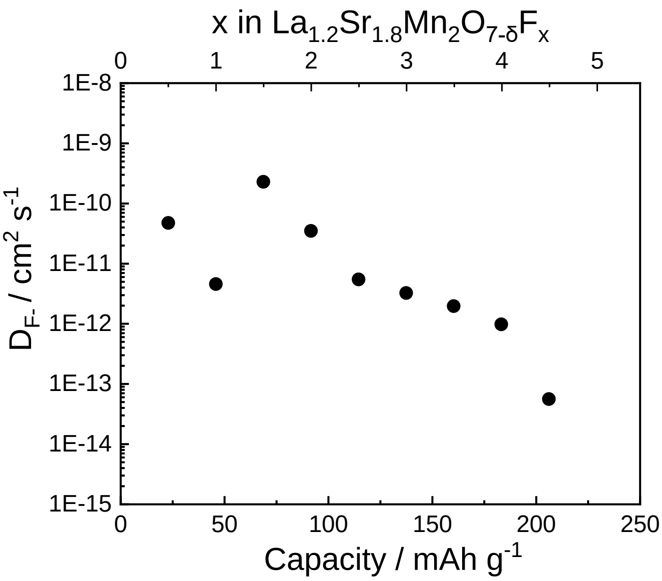

Fig. 2-20. Apparent diffusion coefficient of fluoride ion (D_{F-}) for $La_{1.2}Sr_{1.8}Mn_2O_{7-\delta}F_2$ oxyfluoride during charge process.

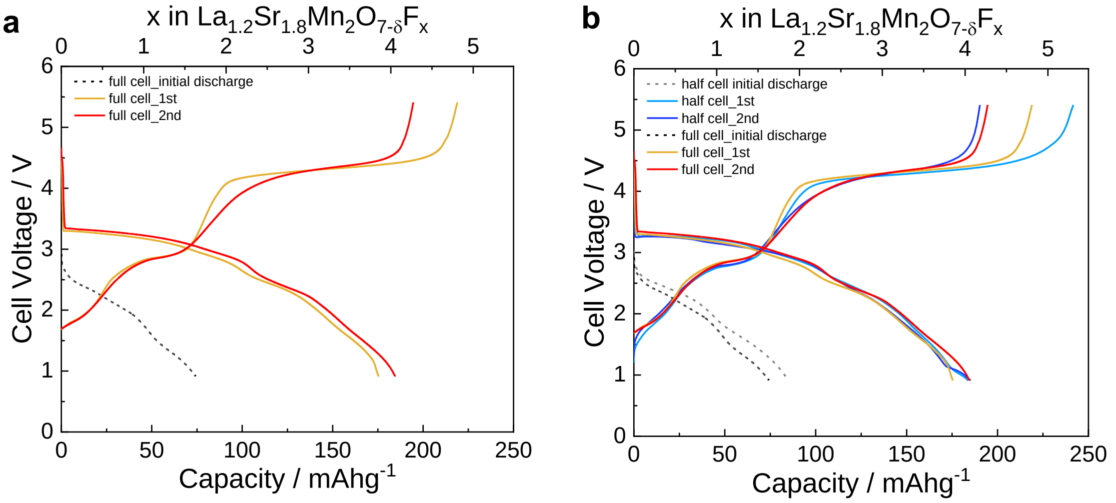

Fig. 2-21. a, Charge/discharge profiles of $La_{1.2}Sr_{1.8}Mn_2O_{7-\delta}F_2$ oxyfluoride cathode/$La_{0.9}Ba_{0.1}F_{2.9}$/La full-cell at a rate of 5 mA/g under 140 °C. The cathode mixture consists of $La_{1.2}Sr_{1.8}Mn_2O_{7-\delta}F_2$, $La_{0.9}Ba_{0.1}F_{2.9}$ and VGCF in a weight ratio of 30:60:10. The anode reaction is the fluorination and defluorination of La metal. Assuming full utilization of the anode, the gravimetric and volumetric energy densities based on the active materials were estimated in **Table 2-2**. **b**. A comparison of full cell data with the half-cell data as shown in **Fig. 2-12a**, in which the data for the half-cell voltage are shown with an offset of 2.41 V since the La deposition/dissolution potential is 2.41 V vs. Pb/PbF_2.

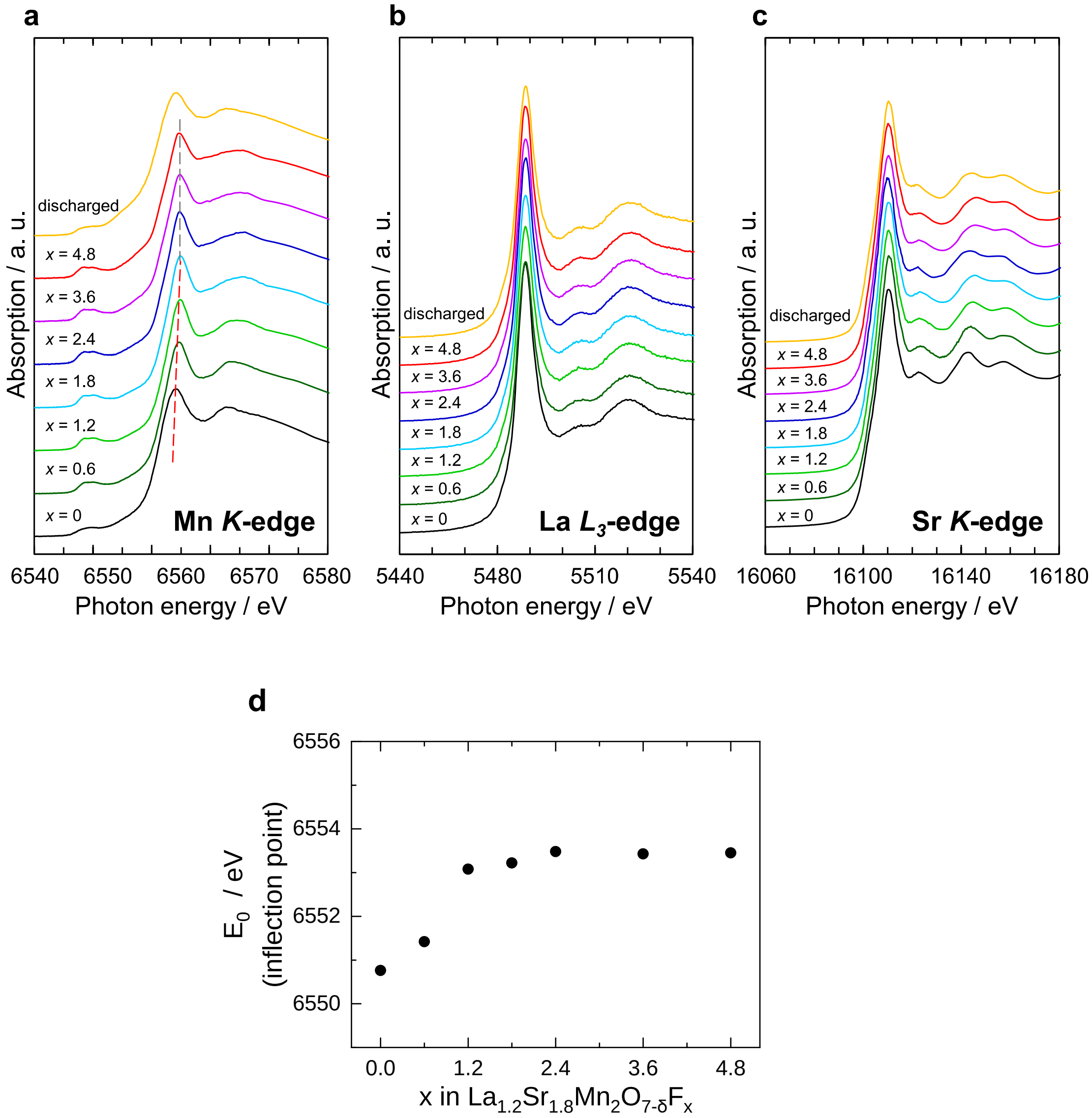

Fig. 2-22. Changes in electronic structures for $La_{1.2}Sr_{1.8}Mn_2O_{7-\delta}F_2$ oxyfluoride on 1st charge/discharge process. Changes in XAS spectra collected for various states in charge/discharge profiles shown in **Fig. 2-12a**. **a**, Mn *K*-edge absorption, **b**, La L_3-edge absorption **c**, Sr *K*-edge absorption and **d**, the energy at the inflection point of the Mn *K*-edge absorption. The *x* in the figure represents the fluorine content (*x* in $La_{1.2}Sr_{1.8}Mn_2O_{7-\delta}F_x$ oxyfluoride).

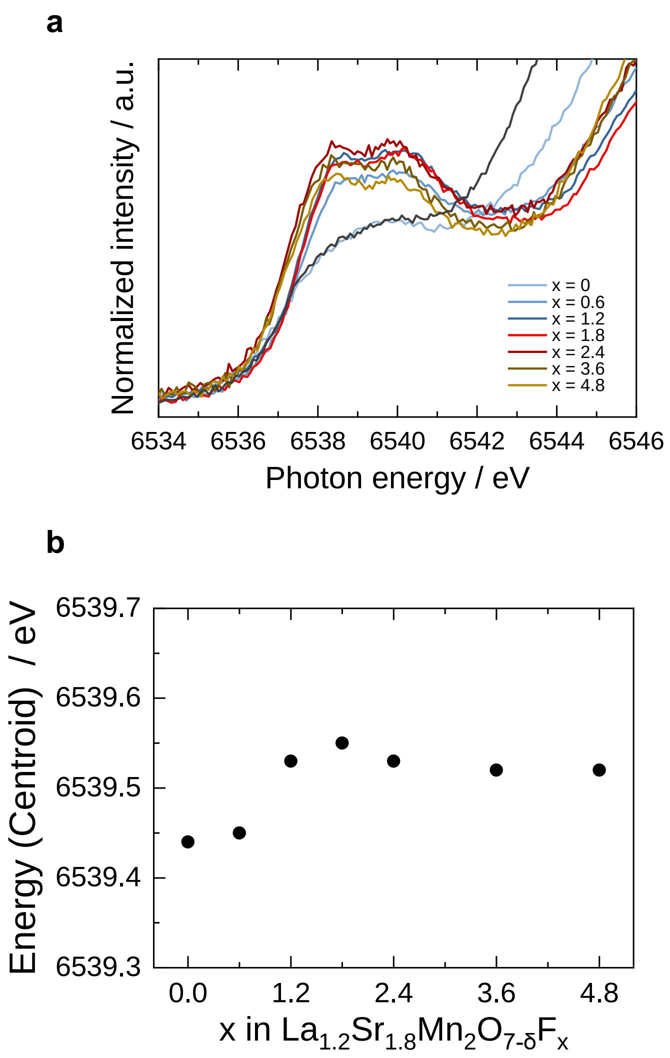

Fig. 2-23. **a**, XAS of Mn *K*-edge in the pre-edge region for $La_{1.2}Sr_{1.8}Mn_2O_{7-\delta}F_2$ oxyfluoride on 1st charge/discharge process, **b**, the pre-edge centroid calculated from the average position of the pseudo-Voigt functions, weighted by their respective integrated region, after subtracting baseline continuum.

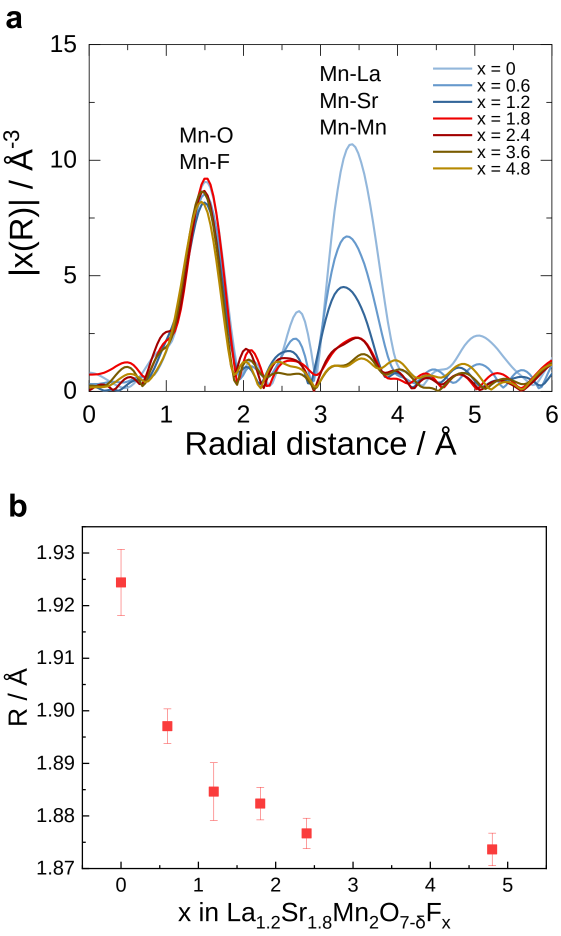

Fig. 2-24. **a**, Fourier transformed EXAFS oscillation of Mn *K*-edge, **b**, the bond length of the first coordination shell obtained from Mn *K*-edge EXAFS analysis of $La_{1.2}Sr_{1.8}Mn_2O_{7-\delta}F_2$ oxyfluoride before and after fluorination in the first charging process. In **Fig. 2-22a**, there is a peak around 1.5 Å, which is attributed to Mn-O/Mn-F bonds. Since it is difficult to distinguish between Mn-O and Mn-F bonds, EXAFS analysis was performed assuming that the first coordination peak at 1.5 Å is due to Mn-O bond. This approximation holds as the small difference in the backscattering power of both O and F. It can be seen from **Fig. 2-22b** that the bond length decreases significantly from $x = 0$ to $x = 2.4$, and then decreases slightly from $x = 2.4$ to $x = 4.8$. The rapid decrease for $0 < x < 2.4$ is consistent with oxidation of Mn, whereas the gradual decrease for $2.4 < x < 4.8$ implies that perhaps the coordination structure around Mn is changing due to molecular O_2 formation. In addition, the second-nearest-neighbor peak at around 3.5 Å is attributed to Mn-La, Mn-Sr, and Mn-Mn bonds. Again, it is difficult to distinguish between these bonds, the reduction of the intensity with the insertion of fluoride ions qualitatively suggests that an increase in the Debye-Waller factor (i.e., increase in local distortion) for these bonds.

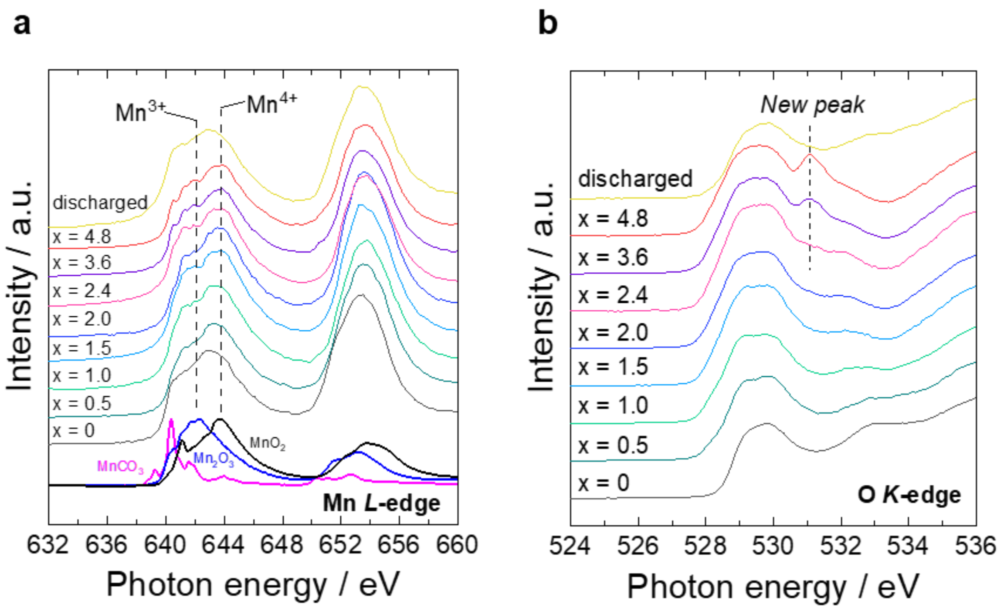

Fig. 2-25. Changes in electronic structures for $La_{1.2}Sr_{1.8}Mn_2O_{7-\delta}F_2$ oxyfluoride on 1st charge/discharge process. **a, b,** Changes in XAS spectra collected for various states in charge/discharge profiles shown in **Fig. 2-12a**. **a**, Mn *L*-edge absorption and **b**, O *K*-edge absorption. The x in the figure represents the fluoride content (x in $La_{1.2}Sr_{1.8}Mn_2O_{7-\delta}F_x$).

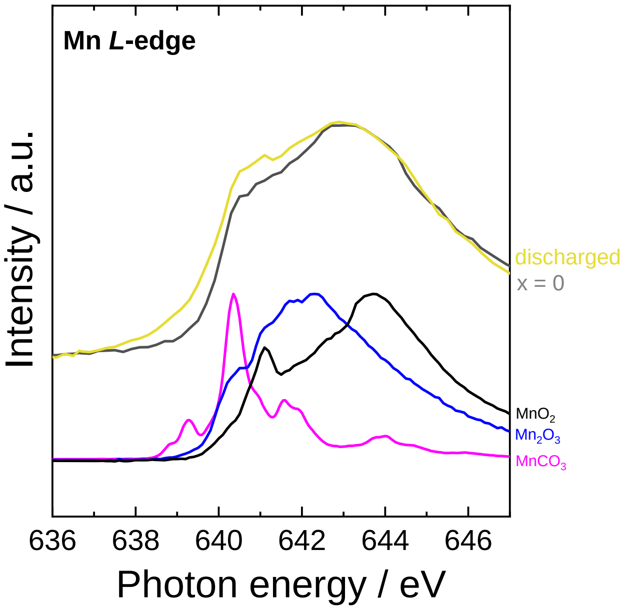

Fig. 2-26. Mn *L*-edge XAS spectra of $La_{1.2}Sr_{1.8}Mn_2O_{7-\delta}F_2$ oxyfluoride after initial discharge and 1st discharge ($x = 0$), taken from **Fig. 2-25a**.

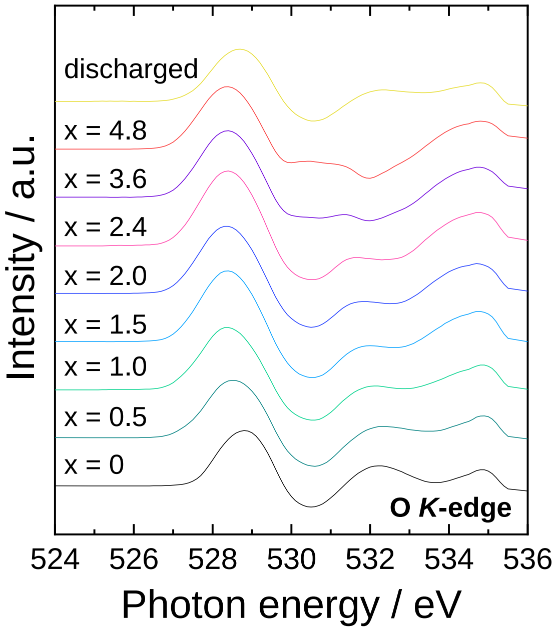

Fig. 2-27. First derivative of **Fig. 2-25b** (O *K*-edge XAS). The *x* in the figure represents the fluoride content (*x* in $La_{1.2}Sr_{1.8}Mn_2O_{7-\delta}F_x$ oxyfluoride)

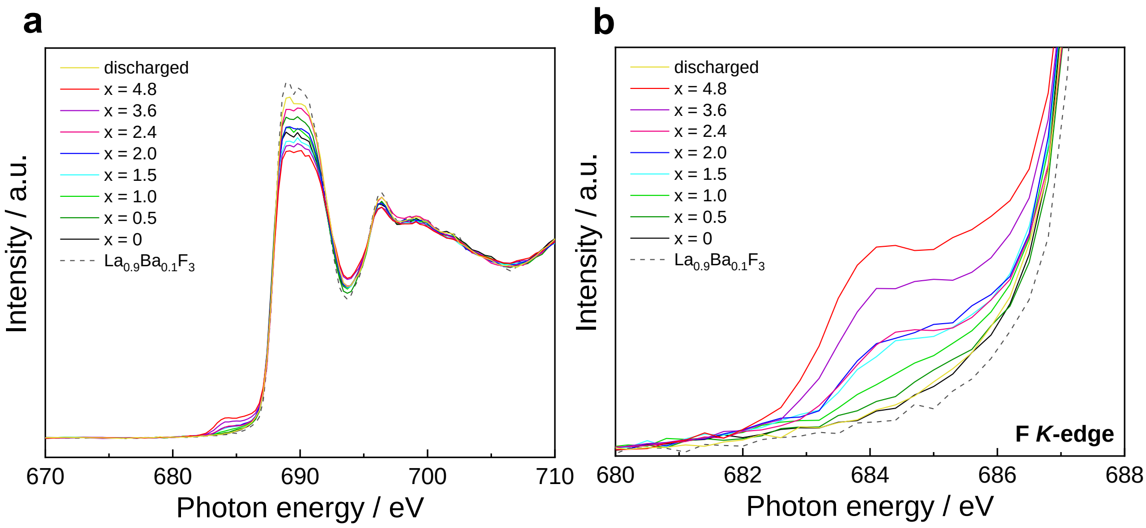

Fig. 2-28. F *K*-edge absorption spectra for $La_{1.2}Sr_{1.8}Mn_2O_{7-\delta}F_2$ oxyfluoride on 1st charge/discharge process. The *x* in the figure represents the fluorine content (*x* in $La_{1.2}Sr_{1.8}Mn_2O_{7-\delta}F_x$ oxyfluoride). F *K*-edge absorption at $x > 2$, indicates the formation of Mn-F bond.

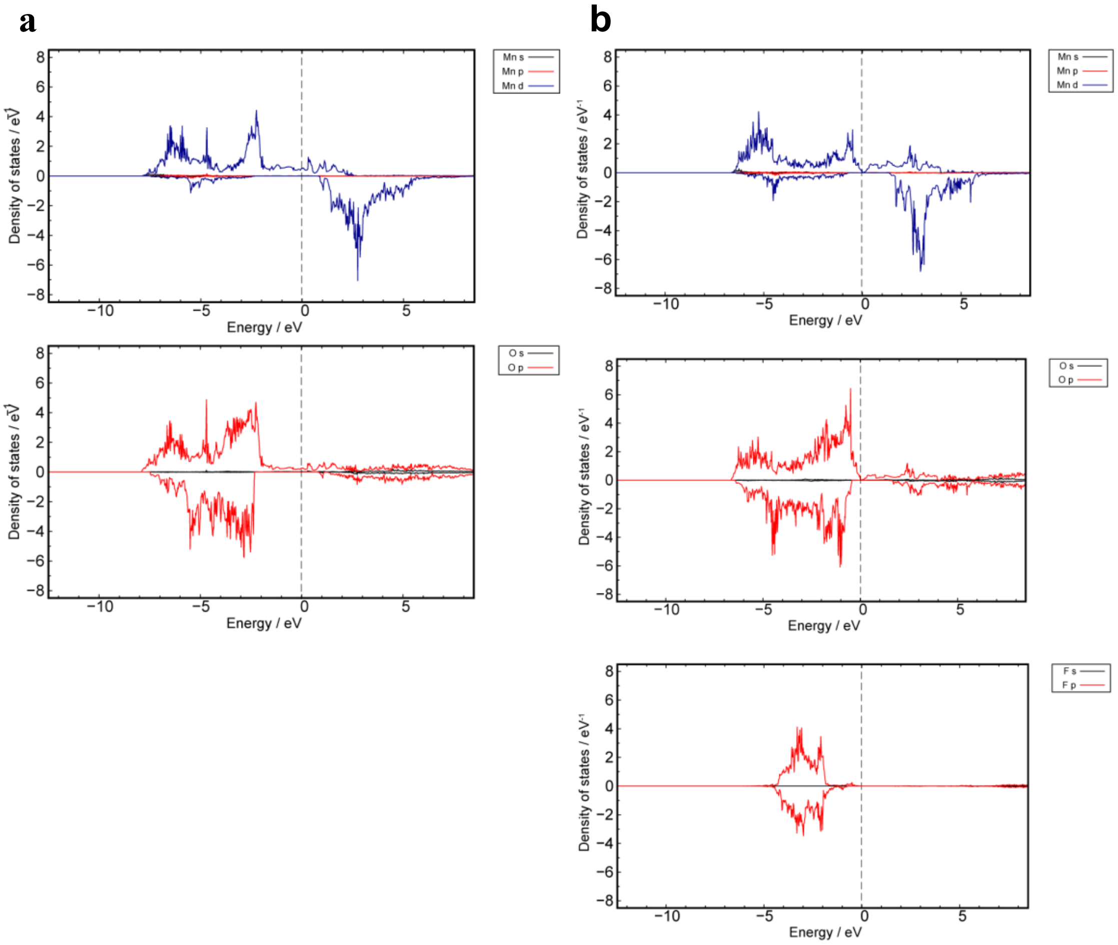

Fig. 2-29. Density of states of O, F, Mn elements for **a** $LaSr_2Mn_2O_{6.5}$ and **b** $LaSr_2Mn_2O_{6.5}F_2$.

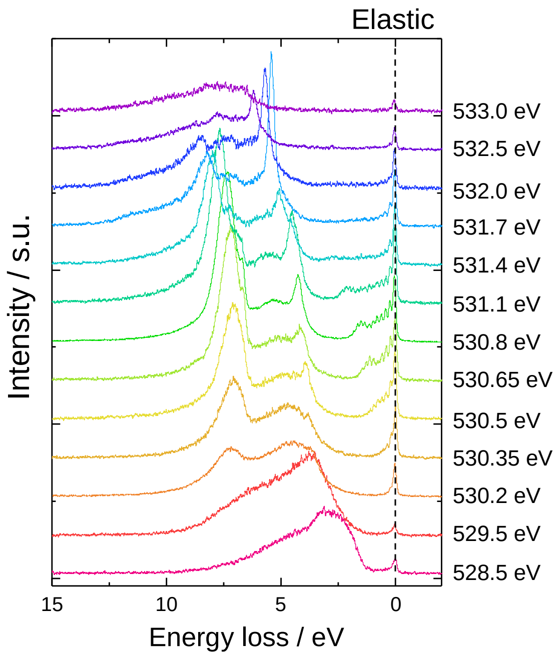

Fig. 2-30. Oxygen *K*-edge RIXS spectra recorded at an excitation energy from 528.5 to 533.0 eV for charged (3.0 V) states.

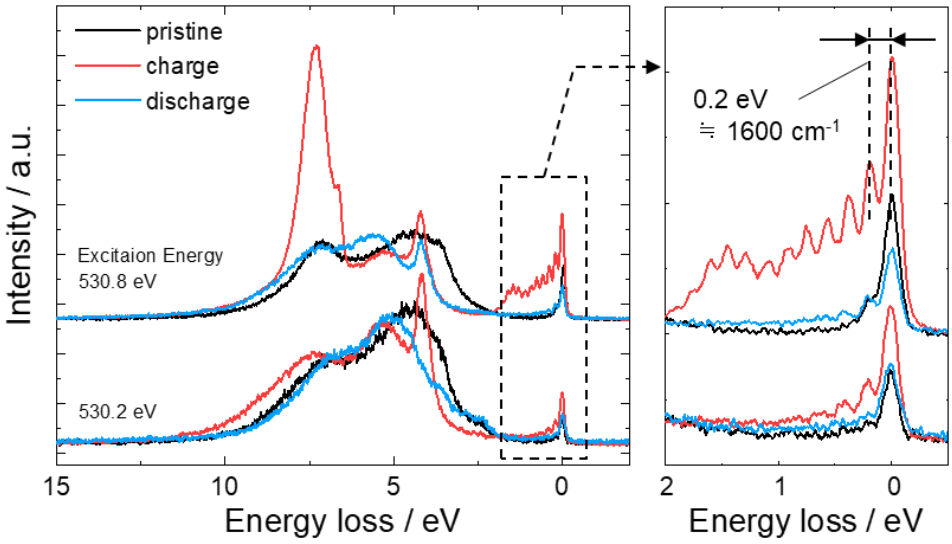

Fig. 2-31. Oxygen *K*-edge XAS and high-resolution RIXS spectra recorded at excitation energies of 530.2 and 530.8 eV for in pristine, charged (3.0 V) and discharged (–1.5 V) states, respectively. The vibrational frequency of around 1600 cm^{-1} indicates the presence of O–O bond.

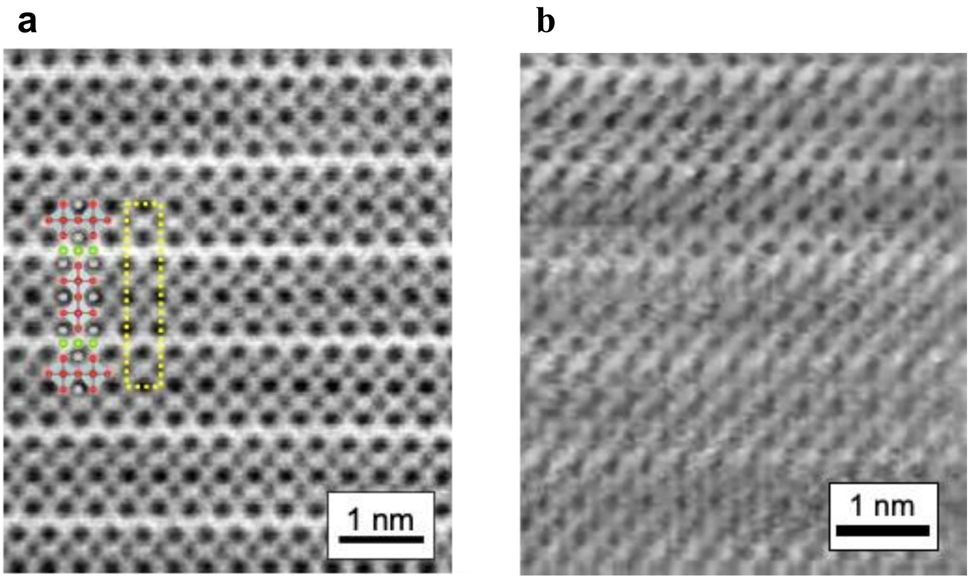

Fig. 2-32. High-magnification images of ABF-STEM observation along [010] of **a** the $La_{1.2}Sr_{1.8}Mn_2O_{7-\delta}F_2$ oxyfluoride cathode and **b** the $La_{1.2}Sr_{1.8}Mn_2O_{7-\delta}F_2$ oxyfluoride cathode after charging to 3.0 V.

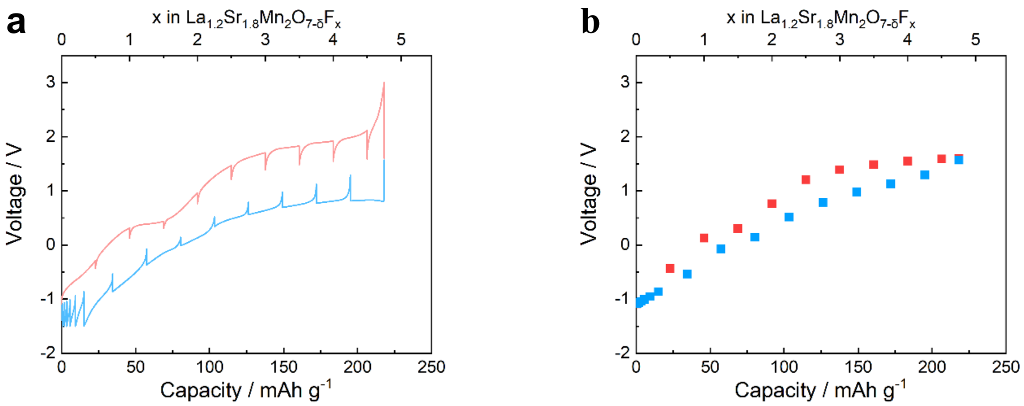

Fig. 2-33. a, Voltage/capacity profile of $La_{1.2}Sr_{1.8}Mn_2O_{7-\delta}F_2$ oxyfluoride obtained by galvanostatic intermittent titration technique and **b,** open-circuit-voltage (OCV) profile obtained from Figure a. To extract structural information of the active material from the voltage change, it is necessary to eliminate such kinetic factors as much as possible. It is seen that the OCV between charge and discharge processes is smaller than 0.5 V, meaning that the observed voltage hysteresis in **Fig. 2-12a** is largely influenced by some resistances in the cathode, the electrolyte, and the anode.

Table 2-1. Structural parameters for $La_{1.2}Sr_{1.8}Mn_2O_{7-\delta}F_2$ oxyfluoride determined from the Rietveld structural analysis.

Atom	**Wyckoff position**	**x**	**y**	**z**	**Occupancy**	**U (Å^2)**
La1	**4e**	**0**	**0**	**0.3198(4)**	**0.38(5)**	**0.007(13)**
Sr1	**4e**	**0**	**0**	**0.3198**	**0.62**	**0.022(14)**
La2	**2b**	**0**	**0.5**	**0.5**	**0.45**	**0.007**
Sr2	**2b**	**0**	**0**	**0.5**	**0.55**	**0.022**
Mn1	**4e**	**0**	**0**	**0.0796(14)**	**1**	**0.007(3)**
O1	**8g**	**0**	**0.5**	**0.4148(5)**	**0.94(2)**	**0.017(2)**
O2	**2a**	**0**	**0**	**0**	**1**	**0.017**
F1	**4d**	**0**	**0.5**	**0.25**	**1**	**0.081(8)**
O3	**4e**	**0**	**0**	**0.1649(9)**	**0.89(4)**	**0.017**

Space group: *I*4/*mmm*; R_p = 8.25%, R_{wp} = 10.72%, R_F = 2.36%, R_{Fobs} = 4.76%; *a* = *b* = 3.8037(5) Å; *c* = 23.208(5) Å.

Table 2-2 Comparison of energy density based on active materials between LIB and FIB

Battery	LIB	FIB
Cathode	$LiCoO_2$	$La_{1.2}Sr_{1.8}Mn_2O_{7-\delta}F_2$ oxyfluoride cathode
Capacity / mAh g^{-1}	170	185
Density / g cm^{-3}	5.05	5.84
Anode	Graphite	La
Capacity / mAh g^{-1}	372	579
Density / g cm^{-3}	2.20	6.16
Utilization ratio / %	100	100
Capacity ratio of anode/cathode	1	1
Weight ratio of anode/cathode	0.457	0.320
Volume ratio of anode/cathode	1.05	0.303
Average Voltage	3.7	2.6
Gravimetric energy density / Wh kg^{-1}	432	365
Volumetric energy density / Wh L^{-1}	1550	2156

2.5. References

1. B. Dunn, H. Kamath, J.-M. Tarascon. Electrical Energy Storage for the Grid: A Battery of Choices. *Science* 2011, **334**, 928–935.

2. R. A. House, G. J. Rees, M. A. Pérez-Osorio, J.-J. Marie, E. Boivin, A. W. Robertson, A. Nag, M. Garcia-Fernandez, K.-J. Zhou, P. G. Bruce. First-cycle voltage hysteresis in Li-rich 3d cathodes associated with molecular O_2 trapped in the bulk. *Nat. Energy*, **2020**, 5, 777–785.

3. R. A. House, U. Maitra, M. A. Pérez-Osorio, J. G. Lozano, L. Jin, J. W. Somerville, L. C. Duda, A. Nag, A. Walters, K.-J. Zhou, M. R. Roberts, P. G. Bruce. Superstructure control of first-cycle voltage hysteresis in oxygen-redox cathodes. *Nature* **2020**, 577, 502–508.

4. G. Assat, J.-M. Tarascon. Fundamental understanding and practical challenges of anionic redox activity in Li-ion batteries. *Nat. Energy* **2018**, 3, 373–386.

5. M. Sathiya, G. Rousse, K. Ramesha, C. P. Laisa, H. Vezin, M. T. Sougrati, M.-L. Doublet, D. Foix, D. Gonbeau, W. Walker, A. S. Prakash, M. B. Hassine, L. Dupont, J.-M. Tarascon. Reversible anionic redox chemistry in high-capacity layered-oxide electrodes. *Nat. Mater.* **2013**, 12, 827–835.

6. E. McCalla, A. M. Abakumov, M. Saubanère, D. Foix, E. J. Berg, G. Rousse, M.-L. Doublet, D. Gonbeau, P. Noval, G. V. Tendeloo, R. Dominko, J.-M. Tarascon. Visualization of O-O peroxo-like dimers in high-capacity layered oxides for Li-ion batteries. *Science* **2015**, 350, 1516–1512.

7. K. Luo, M. R. Roberts, R. Hao, N. Guerrini, D. M. Pickup, Y.-S. Liu, K. Edstrom, J. Guo, A. V. Chadwick, L. C. Duda, P. G. Bruce. Charge-compensation in 3d-transition-metal-oxide intercalation cathodes through the generation of localized electron holes on oxygen. *Nat. Chem.* **2016**, 8, 684–691.

8. D.-H. Seo, J. Lee, A. Urban, R. Malik, S. Kang, G. Ceder. The structural and chemical origin of the oxygen redox activity in layered and cation-disordered Li-excess cathode materials. *Nat. Chem.* **2016**, 8, 692–697.

9. N. Yabuuchi, M. Nakayama, M. Takeuchi, S. Komaba, Y. Hashimoto, T. Mukai, H. Shiiba, K. Sato, Y. Kobayashi, A. Nakao, M. Yonemura, K. Yamanaka, K. Mitsuhara,

T. Ohta. Origin of stabilization and destabilization in solid-state redox reaction of oxide ions for lithium-ion batteries. *Nat. Commun.* **2016**, 7, 13814.

10. P. E. Pearce, A. J. Perez, G. Rousse, M. Saubanère, D. Batuk, D. Foix, E. McCalla, A. M. Abakumov, G. V. Tendeloo, M.-L. Doublet, J.-M. Tarascon. Evidence for anionic redox activity in a tridimensional-ordered Li-rich positive electrode β-Li_2IrO_3. *Nat. Mater.* **2017**, 16, 580–586.

11. M. Ben Yahia, J. Vergnet, M. Saubanère, M.-L. Doublet. Unified picture of anionic redox in Li/Na-ion batteries. *Nat. Mater.* **2019**, 18, 496–502.

12. N. Kamaya, K. Homma, Y. Yamakawa, M. Hirayama, R. Kanno, M. Yonemura, T. Kamiyama, Y. Kato, S. Hama, K. Kawamoto, A. Mitsui. A lithium superionic conductor. *Nat. Mater.* **2011**, 10, 682–686.

13. P. G. Bruce, S. A. Freunberger, L. J. Hardwick, J.-M. Tarascon. Li–O_2 and Li–S batteries with high energy storage. *Nat. Mater.* **2012**, 11, 19–29.

14. J. S. Lee, S. T. Kim, R. Cao, N. S. Choi, M. Liu, K. T. Lee, J. Cho. Metal–Air Batteries with High Energy Density: Li–Air versus Zn–Air. *Adv. Energy Mater.* **2011**, 1, 34–50.

15. J. Winsberg, T. Hagemann, T. Janoschka, M. D. Hager, U. S. Schubert. Redox-Flow Batteries: From Metals to Organic Redox-Active Materials. *Angew. Chem., Int. Ed.* **2017**, 56, 686–711.

16. S. W. Kim, D. H. Seo, X. Ma, G. Ceder, K. Kang. Electrode Materials for Rechargeable Sodium-Ion Batteries: Potential Alternatives to Current Lithium-Ion Batteries. *Adv. Energy Mater.* **2012**, 2, 710–721.

17. D. Aurbach, Z. Lu, A. Schechter, Y. Gofer, H. Gizbar, R. Turgeman, Y. Cohen, M. Moshkovich, E. Levi. Prototype systems for rechargeable magnesium batteries. *Nature* **2000**, 407, 724–727.

18. X. Zhao, S. Ren, M. Bruns, M. Fichtner. Chloride ion battery: A new member in the rechargeable battery family. *J. Power Sources* 2014, 245, 706–711.

19. V. K. Davis, C. M. Bates, K. Omichi, B. M. Savoie, N. Momčilović, Q. Xu, W. J. Wolf, M. A. Webb, K. J. Billings, N. H. Chou, S. Alayoglu, R. K. McKenney, I. M. Darolles, N. G. Nair, A. Hightower, D. Rosenberg, M. Ahmed, C. J. Brooks, T. F. Miller III, R. H. Grubbs, S. C. Jones. Room-temperature cycling of metal fluoride

electrodes: Liquid electrolytes for high-energy fluoride ion cells. *Science* **2018**, 362, 1144–1148.

20. M. A. Reddy, M. Fichtner. Batteries based on fluoride shuttle. *J. Mater. Chem.* **2011**, 21, 17059–17062.

21. F. Gschwind, G. Rodriguez-Garcia, D. J. S. Sandbeck, A. Gross, M. Weil, M. Fichtner, N. Hormann. Fluoride ion batteries: Theoretical performance, safety, toxicity, and a combinatorial screening of new electrodes. *J. Fluorine Chem.* **2016**, 182, 76−90.

22. D. T. Thieu, M. H. Fawey, H. Bhatia, T. Diemant, V. S. K. Chakravadhanula, R. J. Behm, C. Kübel, M. Fichtner. CuF_2 as Reversible Cathode for Fluoride Ion Batteries. *Adv. Funct. Mater.* **2017**, 27, 1701051.

23. C. Rongeat, M. A. Reddy, T. Diemant, R. J. Behm, M. Fichtner. Development of new anode composite materials for fluoride ion batteries. *J. Mater. Chem. A* **2014**, 2, 20861−20872.

24. D. Zhang, K. Yamamoto, A. Ochi, Y. Wang, T. Yoshinari, K. Nakanishi, H. Nakano, H. Miki, S. Nakanishi, H. Iba, T. Uchiyama, T. Watanabe, Y. Orikasa, K. Amezawa, Y. Uchimoto. Understanding the reaction mechanism and performances of 3d transition metal cathodes for all-solid-state fluoride ion batteries. *J. Mater. Chem. A*, **2021**, 9, 406–412.

25. H. Nakano, T. Matsunaga, T. Mori, K. Nakanishi, Y. Morita, K. Ide, K. Okazaki, Y. Orikasa, T. Minato, K. Yamamoto, Z. Ogumi, Y. Uchimoto. Fluoride-Ion Shuttle Battery with High Volumetric Energy Density. *Chem. Mater.* **2021**, 33, 459–466.

26. T. Yoshinari, D. Zhang, K. Yamamoto, Y. Kitaguchi, A. Ochi, K. Nakanishi, H. Miki, S. Nakanishi, H. Iba, T. Uchiyama, T. Watanabe, T. Matsunaga, K. Amezawa, Y. Uchimoto. Kinetic analysis and alloy designs for metal/metal fluorides toward high rate capability for all-solid-state fluoride-ion batteries. *J. Mater. Chem. A*, **2021**, 9, 7018–7024.

27. D. Zhang, T. Yoshinari, K. Yamamoto, Y. Kitaguchi, A. Ochi, K. Nakanishi, H. Miki, S. Nakanishi, H. Iba, T. Watanabe, T. Uchiyama, Y. Orikasa, K. Amezawa, Y. Uchimoto. Cu–Pb Nanocomposite Cathode Material toward Room-Temperature Cycling for All-Solid-State Fluoride-Ion Batteries. *ACS Appl. Energy Mater.* **2021**, 4, 3352–3357.

28. A. J. Bard, R. Parsons, J. Jordan, *Standard potentials in aqueous solution.* New York, M. Dekker **1985**.

29. Y. Tsujimoto, K. Yamaura, E. Takayama-Muromachi. Oxyfluoride Chemistry of Layered Perovskite Compounds. *Appl. Sci.* **2012**, 2, 206–219.

30. C. Greaves, J. L. Kissick, M. G. Francesconi, L. D. Aikens, L. J. Gillie. Synthetic strategies for new inorganic oxide fluorides and oxide sulfates. *J. Mater. Chem.* **1999**, 9, 111–116.

31. R. K. Li, C. Greaves. Double-layered ruthenate $Sr_3Ru_2O_7F_2$ formed by fluorine insertion into $Sr_3Ru_2O_7$. *Phys. Rev. B* **2000**, 62, 3811–3815.

32. T. Sivakumar, J. B. Wiley. Topotactic route for new layered perovskite oxides containing fluorine: $Ln_{1.2}Sr_{1.8}Mn_2O_7F_2$ (Ln = Pr, Nd, Sm, Eu, and Gd). *Mater. Res. Bull.* **2009**, 44, 74–77.

33. R. Zhang, G. Read, F. Lang, T. Lancaster, S. J. Blundell, M. A. Hayward. $La_2SrCr_2O_7F_2$: A Ruddlesden−Popper Oxyfluoride Containing Octahedrally Coordinated Cr4+ Centers. *Inorg. Chem*. **2016**, 55, 3169−3174.

34. K. Mizushima, P. C. Jones, P. J. Wiseman, J. B. Goodenough. Li_xCoO_2 (0<x<-1): A new cathode material for batteries of high energy density. *Mater. Res. Bull.* **1980**, 15, 783–789.

35. N. Yabuuchi, T. Ohzuku. Novel lithium insertion material of $LiCo_{1/3}Ni_{1/3}Mn_{1/3}O_2$ for advanced lithium-ion batteries. *J. Power Sources* **2003**, 119-121, 171–174.

36. M. A. Nowroozi, K. Wissel, J. Rohrer, A. R. Munnangi, O. Clemens. $LaSrMnO_4$: Reversible Electrochemical Intercalation of Fluoride Ions in the Context of Fluoride Ion Batteries. *Chem. Mater.* **2017**, 29, 3441–3453.

37. Y. Wang, K. Yamamoto, Y. Tsujimoto, T. Matsunaga, D. Zhang, Z. Cao, K. Nakanishi, T. Uchiyama, T. Watanabe, T. Takami, H. Miki, S. Nakanishi, H. Iba, K. Maeda, H. Kageyama, Y. Uchimoto. Anion Substitution at Apical Sites of Ruddlesden–Popper-type Cathodes toward High Power Density for All-Solid-State Fluoride-Ion Batteries. *Chem. Mater.* **2022**, 34, 609–616.

38. Y. Wang, T. Takami, Z. Li, K. Yamamoto, T. Matsunaga, T. Uchiyama, T. Watanabe, H. Miki, T. Inoue, H. Iba, U. Mizutani, H. Sato, K. Maeda, H. Kageyama, Y. Uchimoto. Oxyfluoride Cathode for All-Solid-State Fluoride-Ion Batteries with

Small Volume Change Using Three-Dimensional Diffusion Paths. *Chem. Mater.* **2022**, 34, 10631–10638.

39. M. A. Nowroozi, S. Ivlev, J. Rohrer, O. Clemens. La_2CoO_4: a new intercalation based cathode material for fluoride ion batteries with improved cycling stability. *J. Mater. Chem. A* **2018**, 6, 4658–4669.

40. S. Vasala, A. Jakob, K. Wissel, A. I. Waidha, L. Alff, O. Clemens. Reversible Tuning of Magnetization in a Ferromagnetic Ruddlesden–Popper-Type Manganite by Electrochemical Fluoride-Ion Intercalation. *Adv. Electron. Mater.* **2020**, 6, 1900974–9.

41. M. A. Nowroozi, K. Wissel, M. Donzelli, N. Hosseinpourkahvaz, S. Plana-Ruiz, U. Kolb, R. Schoch, M. Bauer, A. M. Malik, J. Rohrer, S. Ivlev, F. Kraus, O. Clemens. High cycle life all-solid-state fluoride ion battery with La_2NiO_{4+d} high voltage cathode. *Commun. Mater.* **2020**, 1, 27.

42. L. D. Aikens, L. J. Gillie, R. K. Li, C. Greaves. Staged fluorine insertion into manganese oxides with Ruddlesden–Popper structures: $LaSrMnO_4F$ and $La_{1.2}Sr_{1.8}Mn_2O_7F$. *J. Mater. Chem.* **2002**, 12, 264–267.

43. C. Rongeat, M. A. Reddy, R. Witter, M. Fichtner. Solid Electrolytes for Fluoride Ion Batteries: Ionic Conductivity in Polycrystalline Tysonite-Type Fluorides. *ACS Appl. Mater. Interfaces* **2014**, 6, 2103–2110.

44. S. Torii, M. Yonemura, T. Yulius Surya Panca Putra, J. Zhang, P. Miao, T. Muroya, R. Tomiyasu, T. Morishima, S. Sato, H. Sagehashi, Y. Noda, T. Kamiyama. Super High Resolution Powder Diffractometer at J-PARC. *J. Phys. Soc. Jpn.* **2011**, 80, SB020.

45. T. Hattori, Y. Katayama, A. Machida, T. Otomo, K. Suzuya. For high-pressure experiments using total scattering spectrometer NOVA at J-PARC. *J. Phys.: Conf. Ser.* **2010**, 215, 012024.

46. S. Kawaguchi, M. Takemoto, K. Osaka, E. Nishibori, C. Moriyoshi, Y. Kubota, Y. Kuroiwa, K. Sugimoto. High-throughput powder diffraction measurement system consisting of multiple MYTHEN detectors at beamline BL02B2 of SPring-8. *Rev. Sci. Instrum.* **2017**, 88, 085111.

47. Y. Harada, M. Kobayashi, H. Niwa, Y. Senba, H. Ohashi, T. Tokushima, Y. Horikawa, S. Shin, M. Oshima. Ultrahigh resolution soft x-ray emission spectrometer at BL07LSU in SPring-8. *Rev. Sci. Instrum.* **2012**, 83, 013116.

48. P. E. Blöchl. Projector augmented-wave method. *Phys. Rev. B*, **1994**, 50, 17953–17979.

49. G. Kresse, D. Joubert. From ultrasoft pseudopotentials to the projector augmented-wave method. *Phys. Rev. B*, **1999**, 59, 1758–1775.

50. G. Kresse, J. Hafner. *Ab initio* molecular dynamics for liquid metals. *Phys. Rev. B*, **1993**, 47, 558–561.

51. G. Kresse, J. Furthmüller. Efficiency of ab-initio total energy calculations for metals and semiconductors using a plane-wave basis set. *Comp. Mater. Sci.*, **1996**, 6, 15–50.

52. G. Kresse, J. Furthmüller. Efficient iterative schemes for *ab initio* total-energy calculations using a plane-wave basis set. *Phys. Rev. B*, **1996**, 54, 11169–11186.

53. J. P. Perdew, A. Ruzsinszky, G. I. Csonka, O. A. Vydrov, G. E. Scuseria, L. A. Constantin, X. Zhou, K. Burke. Restoring the Density-Gradient Expansion for Exchange in Solids and Surfaces. *Phys. Rev. Lett.* **2008**, 100, 136406.

54. S. L. Dudarev, G. A. Botton, S. Y. Savrasov, C. J. Humphreys, A. P. Sutton. Electron-energy-loss spectra and the structural stability of nickel oxide: An LSDA+U study. *Phys. Rev. B*, **1998**, 57, 1505–1509.

55. M. Ležaić, N. A. Spaldin. High-temperature multiferroicity and strong magnetocrystalline anisotropy in 3*d*-5*d* double perovskites. *Phys. Rev. B*, **2011**, 83, 024410.

56. H. J. Monkhorst, J. D. Pack. Special points for Brillouin-zone integrations. *Phys. Rev. B*, **1976**, 13, 5188.

57. K. Momma, F. Izumi. *VESTA 3* for three-dimensional visualization of crystal, volumetric and morphology data. *J. Appl. Crystallogr.*, **2011**, 44, 1272–1276.

58. R. Xiao, H. Li, L. Chen. Density Functional Investigation on Li_2MnO_3. *Chem. Mater.* **2012**, 24, 4242–4251.

59. R. A. House, U. Maitra, L. Jin, J. G. Lozano, J. W. Somerville, N. H. Rees, A. J. Naylor, L. C. Duda, F. Massel, A. V. Chadwick, S. Ramos, D. M. Pickup, D. E.

McNally, X. Lu, T. Schmitt, M. R. Roberts, P. G. Bruce. What Triggers Oxygen Loss in Oxygen Redox Cathode Materials?. *Chem. Mater.* **2019**, 31, 3293–3300.

60. J. Xie, N. Imanishi, T. Matsumura, A. Hirano, Y.o Takeda, O. Yamamoto, Orientation dependence of Li–ion diffusion kinetics in $LiCoO_2$ thin films prepared by RF magnetron sputtering, *Solid State Ionics* **2008**, 179, 362–370.

61. N. Nitta, F. Wu, J. T. Lee, G. Yushin. Li-ion battery materials: present and future. *Materials Today* **2015**, 18, 252–264.

62. C. M. Julien, A. Mauger. Review of 5-V electrodes for Li-ion batteries: status and trends. *Ionics* **2013**, 19, 951–988.

63. W.-S. Yoon, M. Balasubramanian, K. Y. Chung, X.-Q. Yang, J. McBreen, C. P. Grey, D. A. Fischer. Investigation of the Charge Compensation Mechanism on the Electrochemically Li-Ion Deintercalated $Li_{1-x}Co_{1/3}Ni_{1/3}Mn_{1/3}O_2$ Electrode System by Combination of Soft and Hard X-ray Absorption Spectroscopy. *J. Am. Chem. Soc.* **2005**, 127, 17479–17487.

64. K. Yamamoto, Y. Zhou, N. Yabuuchi, K. Nakanishi, T. Yoshinari, T. Kobayashi, Y. Kobayashi, R. Yamamoto, A. Watanabe, Y. Orikasa, K. Tsuruta, J. Park, H. R. Byon, Y. Tamenori, T. Ohta, Y. Uchimoto. Charge Compensation Mechanism of Lithium-Excess Metal Oxides with Different Covalent and Ionic Characters Revealed by *Operando* Soft and Hard X-ray Absorption Spectroscopy. *Chem. Mater.* **2020**, 32, 139–147.

65. J. Wang, Y. Shin, E. M. Arenholz, B. M. Lefler, J. M. Rondinelli, S. J. May. Effect of fluoropolymer composition on topochemical synthesis of $SrMnO_{3-\delta}F_{\gamma}$ oxyfluoride films. *J. Phys. Rev. Mater*. **2018**, 2, 073407.

66. N. H. Bashian, M. Zuba, A. Irshad, S. M. Becwar, J. Vinckeviciute, W. Rahim, K. J. Griffith, E. T. McClure, J. K. Papp, B. D. McCloskey, D. O. Scanlon, B. F. Chmelka, A. V. Ven, S. R. Narayan, L. F. J. Piper, B. C. Melot, Electrochemical Oxidative Fluorination of an Oxide Perovskite, *Chem. Mater.* **2021**, 33, 5757−5768

67. F. Hennies, A. Pietzsch, M. Berglund, A. Fohlisch, T. Schmitt, V. Strocov, H. O. Karlsson, J. Andersson, J. E. Rubensson. Resonant Inelastic Scattering Spectra of Free Molecules with Vibrational Resolution. *Phys. Rev. Lett.* **2010**, 104, 193002.

68. A. R. Genreith-Schriever, H. Banerjee, A. S. Menon, E. N. Bassey, L. F.J. Piper, C. P. Grey and A. J. Morris, Oxygen hole formation controls stability in LiNiO$_2$ cathodes, *Joule* **2023**, 7, 1623–1640.

69. T. X. Carroll and T. D. Thomas, Deexcitation electron spectroscopy of core ‐ excited O$_2$, *J. Chem. Phys.* **1990**, 92, 7171−7177.

70. M. Neeb, J.-E. Rubensson, M. Biermann, W. Eberhardt, K.J. Randall, J. Feldhaus, A.L.D. Kilcoyne, A.M. Bradshaw, Z. Xu, P.D. Johnson, Y. Ma. Effects of time evolution of coherently excited vibrations in molecular core—hole decay spectra of O$_2$, *Chem. Phys. Lett.* **1993**, 212, 205.

71. S. L. Sorensen, R. Fink, R. Feifel, M. N. Piancastelli, M. Bassler, C. Miron, H. Wang, I. Hjelte, O. Björneholm, S. Svensson, High-resolution excitation-energy-dependent study of the Auger decay of the O 1s－1π_g core-excited state in oxygen, *Phys. Rev. A* **2001**, 64, 012719.

72. Q. Liu, X. Su, D. Lei, Y. Qin, J. Wen, F. Guo, Y. A. Wu, Y. Rong, R. Kou, X. Xiao, F. Aguesse, J. Bareño, Y. Ren, W. Lu, Y. Li. Approaching the capacity limit of lithium cobalt oxide in lithium ion batteries via lanthanum and aluminium doping. *Nat. Energy* **2018**, 3, 936–943.

73. M. Nakajima, N. Yabuuchi. Lithium-Excess Cation-Disordered Rocksalt-Type Oxide with Nanoscale Phase Segregation: $Li_{1.25}Nb_{0.25}V_{0.5}O_2$. *Chem. Mater.* **2017**, 29, 6927－6935.

74. X. Zhao, Y. Tian, Z. Lun, Z. Cai, T. Chen, B. Ouyang, G. Ceder. Design principles for zero-strain Li-ion cathodes. *Joule* **2022**, 6, 1654–1671.

75. Q. Mi, Y. Ping, Y. Li, B. Cao, B. S. Brunschwig, P. G. Khalifah, G. A. Galli, H. B. Gray, N. S. Lewis. Thermally Stable N$_2$-Intercalated WO$_3$ Photoanodes for Water Oxidation. *J. Am. Chem. Soc.* **2012**, 134, 18318－18324.

76. H. Kageyama, K. Hayashi, K. Maeda, J. Paul Attfield, Z. Hiroi, J. M. Rondinelli, K. R. Poeppelmeier. Expanding frontiers in materials chemistry and physics with multiple anions. *Nat. Commun.* **2018**, 9, 772.

Chapter 3.

Transient Phase Change of Ruddlesden-Popper type Perovskite on Fluoride-ion Intercalation Reaction

Abstract

Ruddlesden-Popper type perovskites are recognized as a promising active material for fluoride-ion batteries (FIBs) due to the intercalation of fluoride ions into the crystal structure. However, the precise reaction mechanism has not been thoroughly elucidated. In this study, we examined the phase transition mechanism of electrochemical F^- intercalation into $La_{1.2}Sr_{1.8}Mn_2O_7$ (LSMO) oxide. The phase transition behavior during F^- intercalation into LSMO follows the two stages. In the first stage from $x = 0$ to $x = 1.0$ of $La_{1.2}Sr_{1.8}Mn_2O_7F_x$, the fluorination proceeds in a two-phase reaction between the LSMO phase (space group; $I4/mmm$) and the $La_{1.2}Sr_{1.8}Mn_2O_7F$ (LSMOF1) phase (space group; $P4/nmm$). The lattice constant c of the LSMOF1 phase gradually increased with increasing x amount. In the second stage from $x = 1.0$ to $x = 2.0$ of $La_{1.2}Sr_{1.8}Mn_2O_7F_x$, the fluorination proceeds in a two-phase coexistence reaction of the LSMOF1 phase and $La_{1.2}Sr_{1.8}Mn_2O_7F_2$ (LSMOF2) phase. In this stage, the lattice constants of the LSMOF1 phase and LSMOF2 phase are independent of the x amount of $La_{1.2}Sr_{1.8}Mn_2O_7F_x$. The apparent diffusion coefficients of fluoride ions in the first stage are larger than those in the second stage maybe because the lattice mismatch between the two phases is reduced by the gradual change in the lattice constant of the LSMOF1 phase in the first stage. This finding is useful for understanding the reaction mechanism of intercalation-type cathode materials for FIBs and improving the electrochemical performances.

3.1. Introduction

To realize green and sustainable energy society in future, much effort has been devoted to the development of an efficient energy storage system. Rechargeable lithium-ion batteries (LIBs) are widely used as a power source for various applications due to their high energy density, light weight, and long. life span. However, developments of larger scale electric power sources, which will be utilized for applications such as electric vehicles with longer drive distances and grid energy storage[1], are needed. To fulfill these requirements, various types of secondary batteries have been proposed[2-7]. Among them, fluoride ion batteries (FIBs), in which fluoride-ion works as a carrier, have a tremendous amount of potential for delivering high theoretical energy density because the high electronegativity of fluorine leads to high voltage of cell[8]. In addition, multivalent reactions using the transformation of metals to their fluorides lead to a large theoretical capacity. In this case, the reaction proceeds by the migration of fluoride ions, which are monovalent anions, rather than the migration of multivalent cations, which have smaller mobility.

The working of solid-state type FIBs was demonstrated in the last decade[2, 9, 10]. In the reports, metal fluorides such as CuF_2, SnF_2, and BiF_3 are electrochemically de-fluorinated/fluorinated as active materials in the batteries[2, 11, 12]. In these fluoride cathodes, a two-phase reaction occurs between metal and metal fluorides[11, 12]. The electronic conductivity in the electrodes changes drastically during charge-discharge because the active materials change between metals and their insulating fluorides. Additionally, in the charge/discharge reaction between metals and their fluorides, the crystal structure change drastically and cause a large volume change. These two factors make the rate capability of metal fluoride cathodes significantly low. To alleviate these issues, one possibility is to search for the material in which fluoride ions can be intercalated topochemically without a significant change of host lattice like $LiCoO_2$ in the LIBs.

Chemical topotactic intercalation of fluorine has been studied in various layered perovskites, especially Ruddlesden-Popper type structure, which has been stacked a rocksalt unit and a perovskite unit alternately along with *c*-axis direction[13]. Fluorine can be inserted in a large space between the rocksalt and perovskite layers. These materials are also possible candidates for electrochemical fluoride-ion intercalation materials. Our recent work has demonstrated that the Ruddlesden-Popper layered perovskite $La_{1.2}Sr_{1.8}Mn_2O_{7-\delta}F_2$ exhibits unprecedentedly good electrochemical performance for FIBs[14]. Thus, topochemical insertion/extraction materials that can accommodate fluoride ions have been discovered to serve as highly efficient cathodes for FIBs. However, unlike the topochemical insertion/extraction of LIBs, the precise reaction mechanism has not been thoroughly elucidated in many cases.

In this study, we focus on the phase transition during the fluoride ion intercalation reaction of $La_{1.2}Sr_{1.8}Mn_2O_7$ and attempt to clarify the mechanism by detailed analysis. The crystal structure of each state of charge is reproduced by synthesizing materials with various compositions by a chemical method and conducting precise structural analysis and studied the mechanism of phase change.

3.2. Experimental

3.2.1. Synthesis of Materials

$La_{1.2}Sr_{1.8}Mn_2O_7$ was synthesized following previous studies[15, 16]. Reagent-grade La_2O_3 (99.99%, obtained from Kojundo Chemical Laboratory), $SrCO_3$ (99.9%, obtained from WAKO pure chemical industries, ltd.), and MnO_2 (99.5%, obtained from WAKO pure chemical industries, ltd.) were mixed in the stoichiometric ratio and thoroughly blended in a planetary ball mill for 10 hours. The resulting mixture was then pelletized and annealed at 1400°C for 20 hours in an air atmosphere. After annealing, the pellets were ground in a mortar and pestle, re-pelletized, and subjected to the same annealing conditions to obtain the final material. The chemical fluorination of $La_{1.2}Sr_{1.8}Mn_2O_7$ was conducted by referring to previous literature[15], using polyvinylidene difluoride (PVdF; Aldrich, average molecular weight: ~180,000, average Mn: ~71,000) for oxidative fluorination. $La_{1.2}Sr_{1.8}Mn_2O_7$ powder and PVdF were placed in separate alumina boats, and heated at 400°C for 10 hours under air atmosphere in an electric furnace to obtain $La_{1.2}Sr_{1.8}Mn_2O_7F_x$. The value of x was controlled by the weight of PVdF. The solid electrolyte $La_{0.9}Ba_{0.1}F_{2.9}$ with fluoride-ion conductivity was synthesized by mixing LaF_3 (99.9%, obtained from Kojundo Chemical Laboratory) and BaF_2 (99.9%, obtained from Kojundo Chemical Laboratory) in a molar ratio of 9:1, ball milling them at 600 rpm for 12 hours in an Ar atmosphere, and then annealing the mixture at 600°C for 10 hours under an Ar atmosphere.

3.2.2. Assembly of the Electrochemical Cell

The cathode composite was composed of $La_{1.2}Sr_{1.8}Mn_2O_7$ powder, $La_{0.9}Ba_{0.1}F_{2.9}$ powder, and Vapor-Grown Carbon Fiber (VGCF, battery grade) in a weight ratio of 30:60:10. They were mixed by ball-milling for 10 hours at 100 rpm in an Ar atmosphere. $La_{0.9}Ba_{0.1}F_{2.9}$ was used as the separator layer. PbF_2/acetylene black (AB) composite was used as the anode. The composite was prepared by ball-milling for 3 hours at 600 rpm in an Ar atmosphere. Additionally, a Pb foil was stacked on top of the anode composite to assist in its reversibility. The electrochemical cells were assembled by first forming the separator layer into a pellet, then applying pressure to stack 10 mg of cathode and 50 mg of PbF_2/AB composite, forming the all-solid-state battery. All fabrication processes of these electrochemical cells were conducted in a glovebox under an argon atmosphere.

3.2.3. Electrochemical Measurement

For the electrochemical measurement assembled cells were put in a sealed container without being exposed to the air atmosphere. Charge and discharge experiments of the all-solid-state fluoride ion cells were conducted in a voltage range -1.0~1.5 V vs. Pb/PbF_2 at 140 °C with a current density of 10 mA g^{-1}. Galvanostatic intermittent titration technique (GITT) for the charge process was obtained by repeating the electrochemical process consisting of current pulses at 10 mA g^{-1}. The electrochemical properties of the electrochemical test cells were collected using a potentiostat/galvanostat apparatus (VMP3, Bio-Logic Science Instruments).

3.2.4. Materials Characterization

X-ray diffraction (XRD) patterns were obtained using Rigaku Ultima IV using Cu Kα radiation with 40 kV of tube voltage and 40 mA of current. Synchrotron XRD measurements were performed at beamlines BL02B2 and BL19B2 at SPring-8, Japan. Corrector-spherical aberration scanning transmission electron-microscope (Cs-STEM) observation was performed using JEM-ARM200F (JEOL) to characterize the crystal structure of the sample after electrochemical measurement. In order to observe the cross-sectional direction of the electrode, thin sections were extracted using the cryo-focused ion beam (cryo-FIB) micro-sampling technique with the nanoDUE'T NB5000 (HITACHI). The cryo functionality was utilized during the processing to minimize damage to the sample. Confirmation of the insertion and removal of fluoride ions in the crystal structure was carried out using atomic-resolution electron energy loss spectroscopy (EELS) mapping.

3.3. Results and Discussion

3.3.1. Crystal Structure during *Electrochemical* Fluorination

The crystal structure of as-prepared $La_{1.2}Sr_{1.8}Mn_2O_7$ oxide was examined by XRD. All of the Bragg peaks were assigned using the space group *I*4/*mmm*, and the lattice constants were a = 3.87478 Å, c = 20.17931 Å (**Fig. 3-1**). This result is in good agreement with previously reported values[15]. The particle size of as-prepared $La_{1.2}Sr_{1.8}Mn_2O_7$ oxide was a few micrometers, which was confirmed by SEM (**Fig. 3-2**).

In order to examine the electrochemical properties of the $La_{1.2}Sr_{1.8}Mn_2O_7$ cathode, the Pb/PbF_2 anode was used in this study. The Pb/PbF_2 is one of most popular anode materials with ideal non-polarizing electrode behavior. The potential is always constant because the reaction proceeds in a two-phase routine[17-19] and it does not change even when a small current flows due to the large exchange current density. Therefore, the Pb/PbF_2 anode is useful to examine accurate electrochemical behavior on the $La_{1.2}Sr_{1.8}Mn_2O_7$ cathode. Charge/discharge curves of the $La_{1.2}Sr_{1.8}Mn_2O_7$ cathode at second cycle and cycle performance for initial 20cycles are shown in **Fig. 3-3**. The cathode provided a charge capacity of 79 mAh g^{-1}, corresponding to the capacity of 1.6 mol of F^- in the cathode with a voltage slope around 0.5 V and a flat plateau around 0.9 V, and the subsequent discharge capacity was 72 mAh g^{-1}. The larger charge capacity than the theoretical capacity (59 mAh g^{-1}) estimated from the formal valence of Mn may be due to the introduction of holes into the 2p orbitals of oxygen during F- intercalation, as in previous reports[14]. Open-circuit voltages (OCVs) at various F contents during charge for the $La_{1.2}Sr_{1.8}Mn_2O_7$ cathode are shown in **Fig. 3-4a**. The OCV gradually increased in the voltage slope region around 0.5 V but became significantly flat in the voltage plateau region around 0.9 V. Potential flat regions are well observed in the case of two-phase reactions, as typified by $LiFePO_4$[20]. Apparent F^- diffusion coefficient (D_{F-}) were estimated by the GITT method. D_{F-} at various F contents during charge for the $La_{1.2}Sr_{1.8}Mn_2O_7$ cathode are shown in **Fig. 3-4b**. The D_{F-} was approximately 10^{-10} cm^2 s^{-1} until the F content of 1.0 whereas it largely decreased to 10^{-11} cm^2 s^{-1} above the F content of 1.0.

Fig. 3-5 shows the results of *ex-situ* XAFS measurements during the charging process. In Mn L_3-edge, the peak confirmed at 643 eV is derived from Mn^{3+}, and the peak confirmed at 644 eV is attributed to Mn^{4+}. As charging progresses, it can be confirmed that the component of the Mn^{4+} peak is increased compared to Mn^{3+}, which suggests that fluorination is charge-compensated by Mn^{4+}/Mn^{3+} redox. After the discharge, the peak intensity derived from Mn^{3+} component appears to increase again, suggesting that the discharge process is also charge-compensated by Mn^{4+}/Mn^{3+} redox. On the other hand, in the potential range of -1.5 to 1.5 V vs. Pb/PbF_2, the spectrum change that suggests anionic redox of the oxide ion as described in the previous study (Chapter 2.) is not confirmed from the O K-edge spectrum. That is, only Mn^{4+}/Mn^{3+} redox will contribute to charge compensation in at least the second cycle.

The crystal structural change of the $La_{1.2}Sr_{1.8}Mn_2O_7$ cathode during charge process was examined by synchrotron XRD (**Fig. 3-6**). Although the XRD patterns of each sample shows strong Bragg peaks at 7.3°, 7.8°, 9.2° attributed to $La_{0.9}Ba_{0.1}F_{2.9}$ solid electrolyte, several Bragg peaks attributed to the $La_{1.2}Sr_{1.8}Mn_2O_7$ cathode in the charged states can be distinguished from the $La_{0.9}Ba_{0.1}F_{2.9}$ peaks. Unfortunately, the peak intensity due to the active material is small because the peak intensity due to the solid electrolyte is large. Before charging, the Bragg peaks attributed to 105 and 110 planes of the $La_{1.2}Sr_{1.8}Mn_2O_7$ phase (LSMO) were observed at 8.4° and 8.7°, respectively. When the $La_{1.2}Sr_{1.8}Mn_2O_7$ cathode was charged from the initial state ($x = 0$) to $x = 0.45$ of $La_{1.2}Sr_{1.8}Mn_2O_7F_x$, the peak intensity attributed to 105 and 110 planes of the $La_{1.2}Sr_{1.8}Mn_2O_7$ phase decreased whereas the peaks attributed to the 105 and 110 planes of $La_{1.2}Sr_{1.8}Mn_2O_7F$ phase (LSMOF, space group: *P*4/*nmm*) appeared at 8.2° and 8.8°, respectively[21]. In the subsequent charge from $x = 0.45$ to $x = 1.22$ of $La_{1.2}Sr_{1.8}Mn_2O_7F_x$, the peaks attributed to the 105 and 110 planes of $La_{1.2}Sr_{1.8}Mn_2O_7F$ phase shifted to the lower and higher angles, respectively. In addition, the peaks attributed to 105 and 110 planes of the $La_{1.2}Sr_{1.8}Mn_2O_7$ phase disappeared whereas the peaks attributed to the 105 and 110 planes of

$La_{1.2}Sr_{1.8}Mn_2O_7F_2$ phase (LSMOF2, space group: *I*4/*mmm*) [16] appeared at 8.1° and 8.9°, respectively. In the further charge from $x = 1.22$ to $x = 1.61$ of $La_{1.2}Sr_{1.8}Mn_2O_7F_x$, the intensity of the $La_{1.2}Sr_{1.8}Mn_2O_7F$ phase-derived peaks decreased while that of the $La_{1.2}Sr_{1.8}Mn_2O_7F_2$ phase-derived peaks increased. Atomic-resolution STEM–EELS mapping, HAADF-STEM and ABF-STEM images confirmed formation of the $La_{1.2}Sr_{1.8}Mn_2O_7F_2$ phase, where fluoride ions are occupied at the interstitial site of the rock-salt slabs (**Fig. 3-7**). These results indicate that the $La_{1.2}Sr_{1.8}Mn_2O_7$ cathode undergoes phase transition to the $La_{1.2}Sr_{1.8}Mn_2O_7F_2$ phase via the $La_{1.2}Sr_{1.8}Mn_2O_7F$ phase during charge process.

3.3.2. *Chemical* Fluorinated $La_{1.2}Sr_{1.8}Mn_2O_{7-\delta}F_x$ ($0 < x < 2$)

The approximate phase transition behavior of the $La_{1.2}Sr_{1.8}Mn_2O_7$ oxide via electrochemical fluorination was examined by synchrotron XRD. However, it is difficult to observe a more detailed phase transition behavior of $La_{1.2}Sr_{1.8}Mn_2O_7$ oxide by electrochemical fluorination because the peak intensity attributed to the active material is significantly weak due to the small amount (30 wt%) of the active material in the cathode composite. Therefore, chemically fluorinated $La_{1.2}Sr_{1.8}Mn_2O_7$ with different fluorine content x was synthesized to examine a detailed phase transition and compare it to that of electrochemical fluorination. **Fig. 3-8a** shows the XRD patterns for chemically fluorinated $La_{1.2}Sr_{1.8}Mn_2O_7$ with different fluorine content x. Before chemical fluorination, Bragg peaks attributed to 105 and 110 planes of the $La_{1.2}Sr_{1.8}Mn_2O_7$ phase (LSMO) were observed at 32.0° and 32.6°, respectively. When the $La_{1.2}Sr_{1.8}Mn_2O_7$ cathode was chemically fluorinated from the initial state ($x = 0$) to $x = 1.0$ of

$La_{1.2}Sr_{1.8}Mn_2O_7F_x$, the intensity of peaks attributed to the 105 and 110 planes of $La_{1.2}Sr_{1.8}Mn_2O_7F$ phase (LSMOF, space group: *P*4/*nmm*) at 31.3° and 33.2° increased and their positions shifted to the lower and higher angles, respectively, respectively[21]. On the other hand, the intensity of the peaks attributed to 105 and 110 planes of the $La_{1.2}Sr_{1.8}Mn_2O_7$ phase decreased and finally ($x = 1.0$ of $La_{1.2}Sr_{1.8}Mn_2O_7F_x$) disappeared. whereas the peaks attributed to the 105 and 110 planes of $La_{1.2}Sr_{1.8}Mn_2O_7F_2$ phase (LSMOF2, space group: *I*4/*mmm*) [16] appeared at 30.4° and 33.7°, respectively. In the further fluorination from $x = 1.0$ to $x = 2.0$ of $La_{1.2}Sr_{1.8}Mn_2O_7F_x$, the intensity of the $La_{1.2}Sr_{1.8}Mn_2O_7F$ phase-derived peaks decreased keeping the positions while the peaks attributed to the 105 and 110 planes of $La_{1.2}Sr_{1.8}Mn_2O_7F_2$ phase at 30.4° and 33.7° increased, and finally ($x = 2.0$ of $La_{1.2}Sr_{1.8}Mn_2O_7F_x$) only the peaks attributed to the $La_{1.2}Sr_{1.8}Mn_2O_7F_2$ phase existed. These results indicate that the $La_{1.2}Sr_{1.8}Mn_2O_7$ undergoes phase transition by chemical fluorination to the $La_{1.2}Sr_{1.8}Mn_2O_7F_2$ phase via the $La_{1.2}Sr_{1.8}Mn_2O_7F$ phase, and that the lattice constant of the $La_{1.2}Sr_{1.8}Mn_2O_7F$ phase varies with the fluoride ion insertion amount. These results are in good agreement with the trend in the electrochemical fluorination results (**Fig. 3-6**).

To quantitatively examine the crystal structural change, the lattice constants of each phase for electrochemically fluorinated $La_{1.2}Sr_{1.8}Mn_2O_7$ and chemically fluorinated $La_{1.2}Sr_{1.8}Mn_2O_7$ were estimated (**Fig. 3-8b**). In the chemically fluorinated $La_{1.2}Sr_{1.8}Mn_2O_7$, the $La_{1.2}Sr_{1.8}Mn_2O_7$ phase was observed from $x = 0$ to $x = 0.8$ of $La_{1.2}Sr_{1.8}Mn_2O_7F_x$, and its lattice constants *a* and *c* were constant regardless of increment of *x*. The $La_{1.2}Sr_{1.8}Mn_2O_7F$ phase was observed from $x = 0.2$ to $x = 1.8$ of $La_{1.2}Sr_{1.8}Mn_2O_7F_x$, and its lattice constant *a* was constant regardless of increment of *x*. On the other hand, its lattice constant *c* increased continuously from $x = 0.2$ to $x = 1.0$ and was constant from $x = 1.0$ to $x = 1.8$ of $La_{1.2}Sr_{1.8}Mn_2O_7F_x$. The $La_{1.2}Sr_{1.8}Mn_2O_7F_2$ phase was observed from $x = 1.0$ to $x = 2.0$ of $La_{1.2}Sr_{1.8}Mn_2O_7F_x$, and its lattice constants a and c were constant regardless of increment of x. The lattice constants of $La_{1.2}Sr_{1.8}Mn_2O_7F_2$ phase are in good agreement with those reported in the literature[15]. The electrochemically fluorinated $La_{1.2}Sr_{1.8}Mn_2O_7$ showed the same trend as the chemically fluorinated $La_{1.2}Sr_{1.8}Mn_2O_7$. These results suggest that the fluorination of $La_{1.2}Sr_{1.8}Mn_2O_7$ proceeds in the following two stages. In the first stage from $x = 0$ to $x = 1.0$ of $La_{1.2}Sr_{1.8}Mn_2O_7F_x$, the fluorination proceeds in a two-phase reaction between the $La_{1.2}Sr_{1.8}Mn_2O_7$ phase and the $La_{1.2}Sr_{1.8}Mn_2O_7F$ phase with lattice constant change. In the second stage from $x = 1.0$ to $x = 2.0$ of $La_{1.2}Sr_{1.8}Mn_2O_7F_x$, the fluorination proceeds in a two-phase coexistence reaction of the $La_{1.2}Sr_{1.8}Mn_2O_7F$ phase without lattice constant change and $La_{1.2}Sr_{1.8}Mn_2O_7F_2$ phase. Such two-phase reactions with lattice parameter changes have been reported in other systems, e.g., Mg^{2+} insertion into $MgMn_2O_4$ spinel oxide[23] and $LiFePO_4$ during electrochemical lithium-ion extraction[24]. As shown in **Fig. 3-9**, the volume expansion ratio of $La_{1.2}Sr_{1.8}Mn_2O_7$/$La_{1.2}Sr_{1.8}Mn_2O_7F_2$ phases was 9.4%, which is larger than that of cathode materials in LIBs such as $LiFePO_4$/$FePO_4$ (6.6%)[25]. However, the volume expansion ratios of $La_{1.2}Sr_{1.8}Mn_2O_7$/$La_{1.2}Sr_{1.8}Mn_2O_7F$ and $La_{1.2}Sr_{1.8}Mn_2O_7F$ /$La_{1.2}Sr_{1.8}Mn_2O_7F_2$ phases were 4.4% and 4.8%, which are smaller than that of $LiFePO_4$/$FePO_4$. Furthermore, since the lattice constant c of $La_{1.2}Sr_{1.8}Mn_2O_7F$ phase becomes smaller with decrease of x in the range of $0.2 \leq x \leq 1$ of $La_{1.2}Sr_{1.8}Mn_2O_7F_x$, the lattice mismatch of $La_{1.2}Sr_{1.8}Mn_2O_7$/$La_{1.2}Sr_{1.8}Mn_2O_7F$ becomes smaller. The relationship between lattice mismatch and ion diffusion coefficient has been studied extensively in the case of lithium ions, and it has been shown that lattice mismatch suppresses lithium-ion diffusion. For example, in $LiFePO_4$, a typical cathode material in which the reaction proceeds in a two-phase reaction, it has been reported that the smaller the lattice volume difference between the two phases of $LiFePO_4/FePO_4$, the higher the phase transition rate and lithium-ion insertion/extraction rate[26]. In the $La_{1.2}Sr_{1.8}Mn_2O_7$ cathode of this study, the lattice volume difference between $La_{1.2}Sr_{1.8}Mn_2O_7$/ $La_{1.2}Sr_{1.8}Mn_2O_7F$ is smaller than that between $La_{1.2}Sr_{1.8}Mn_2O_7F/La_{1.2}Sr_{1.8}Mn_2O_7F_2$. Therefore, the phase transition rate between $La_{1.2}Sr_{1.8}Mn_2O_7/La_{1.2}Sr_{1.8}Mn_2O_7F$ becomes faster than that between $La_{1.2}Sr_{1.8}Mn_2O_7F/La_{1.2}Sr_{1.8}Mn_2O_7F_2$. This leads to higher D_{F-} in the voltage slope region ($x \leq 1$) than in the voltage plateau region ($x > 1$) of $La_{1.2}Sr_{1.8}Mn_2O_7F_x$ as seen in **Fig. 3-4b**. Therefore, the $La_{1.2}Sr_{1.8}Mn_2O_7F$ phase reduces the large lattice mismatch of $La_{1.2}Sr_{1.8}Mn_2O_7/La_{1.2}Sr_{1.8}Mn_2O_7F_2$ phases, leading to the high rate performance[14]. In the previous report, neutron diffraction and Rietveld analysis on $La_{1.2}Sr_{1.8}Mn_2O_7$ oxide with chemical insertion of $2F^-$ show that F^- does not occupy the apical site but the interstitial site in the Ruddlesden-Popper structure[14]. This result implies that F- does not diffuse through apical and interstitial sites like O^{2-} diffusion in Ruddlesden-Popper oxide[27]. More detailed analysis of the diffusion path of F^- in the $La_{1.2}Sr_{1.8}Mn_2O_7F_x$ is a subject for future work to develop new cathode materials with high fluoride-ion diffusion.

3.4. Conclusion

The phase transition mechanism of electrochemical F^- intercalation into $La_{1.2}Sr_{1.8}Mn_2O_7$ oxide was examined by electrochemical measurements, synchrotron XRD, STEM-EELS and by comparing the phase transition of chemical F^- intercalation into $La_{1.2}Sr_{1.8}Mn_2O_7$ oxide. The phase transition behavior of the electrochemical F^- intercalation into $La_{1.2}Sr_{1.8}Mn_2O_7$ corresponds to that of chemical F^- intercalation into

$La_{1.2}Sr_{1.8}Mn_2O_7$, including the following two stages. In the first stage from $x = 0$ to $x = 1.0$ of $La_{1.2}Sr_{1.8}Mn_2O_7F_x$, the fluorination proceeded in a two-phase reaction between the $La_{1.2}Sr_{1.8}Mn_2O_7$ phase and the $La_{1.2}Sr_{1.8}Mn_2O_7F$ phase. In this stage, the lattice constant c of the $La_{1.2}Sr_{1.8}Mn_2O_7F$ phase gradually increased with increasing x amount of $La_{1.2}Sr_{1.8}Mn_2O_7F_x$. In the second stage from $x = 1.0$ to $x = 2.0$ of $La_{1.2}Sr_{1.8}Mn_2O_7F_x$, the fluorination proceeded in a two-phase coexistence reaction of the $La_{1.2}Sr_{1.8}Mn_2O_7F$ phase and $La_{1.2}Sr_{1.8}Mn_2O_7F_2$ phase. In contrast to the first stage, the lattice constant c of the $La_{1.2}Sr_{1.8}Mn_2O_7F$ phase in the second stage was independent of the x amount of $La_{1.2}Sr_{1.8}Mn_2O_7F_x$. The apparent diffusion coefficients of fluoride ions in the first stage are larger than those in the second stage maybe because the lattice mismatch between the two phases is reduced by the gradual change in the lattice constant of the $La_{1.2}Sr_{1.8}Mn_2O_7F_2$ phase in the first stage. We believe that this finding is useful to understand the reaction mechanism of intercalation-type cathode materials for FIBs.

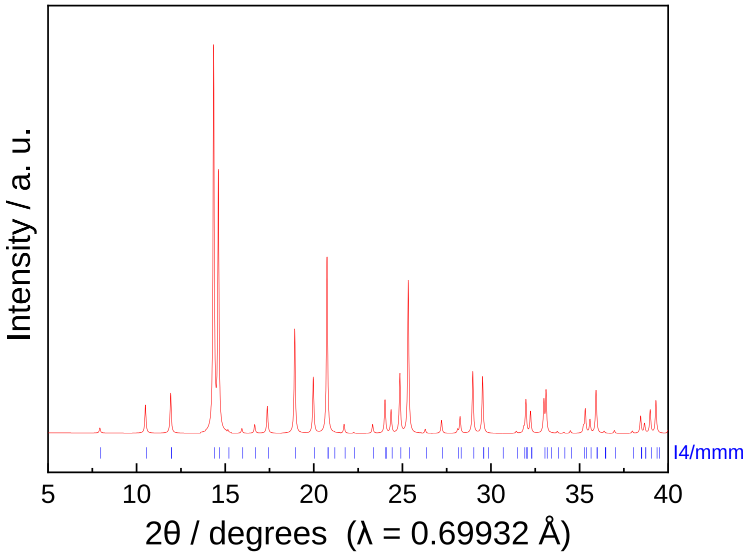

Fig. 3-1. X-ray diffraction pattern of as-prepared $La_{1.2}Sr_{1.8}MnO_7$ oxide.

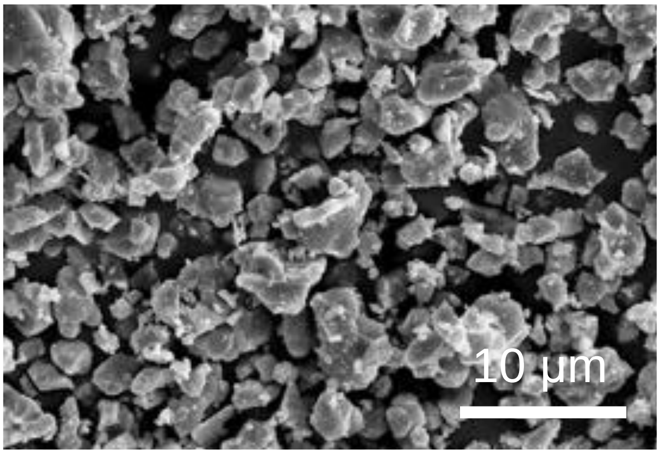

Fig. 3-2. SEM image of as-prepared $La_{1.2}Sr_{1.8}MnO_7$ oxide.

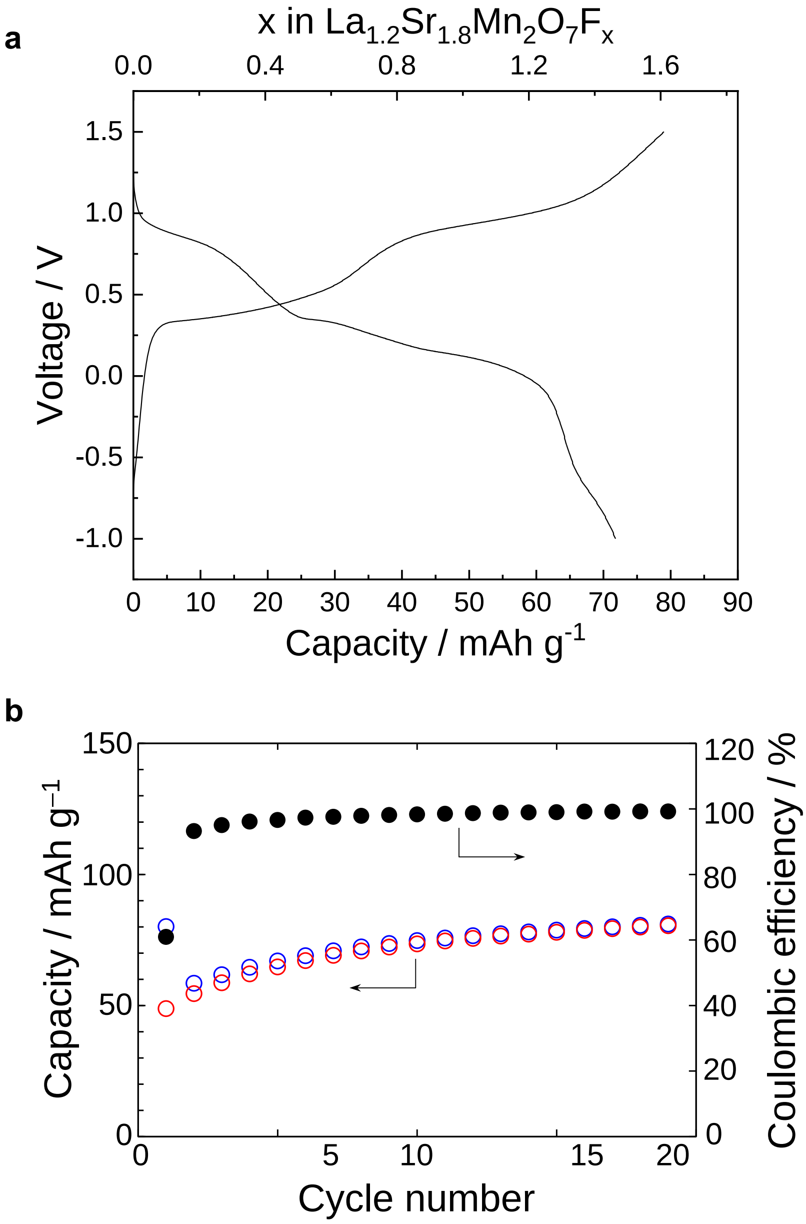

Fig. 3-3. a, Charge-discharge curves of $La_{1.2}Sr_{1.8}Mn_2O_7$ in a voltage range from -1.0 V to 1.5 V vs. Pb/PbF_2 at current density of 10 mA g^{-1}. **b**, Cycle performance for initial 20cycles of $La_{1.2}Sr_{1.8}Mn_2O_7$.

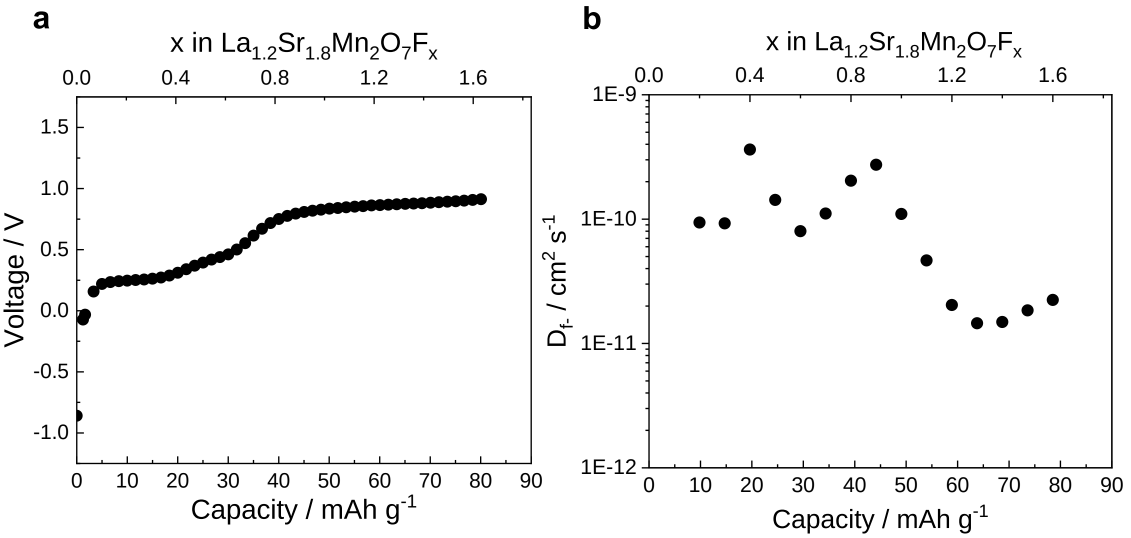

Fig. 3-4. a, OCV of La$_{1.2}$Sr$_{1.8}$Mn$_2$O$_7$ with various F$^-$ contents during charge process. **b**, Apparent diffusion coefficient of fluoride ion (D$_{F^-}$) for La$_{1.2}$Sr$_{1.8}$Mn$_2$O$_7$ cathode during charge process.

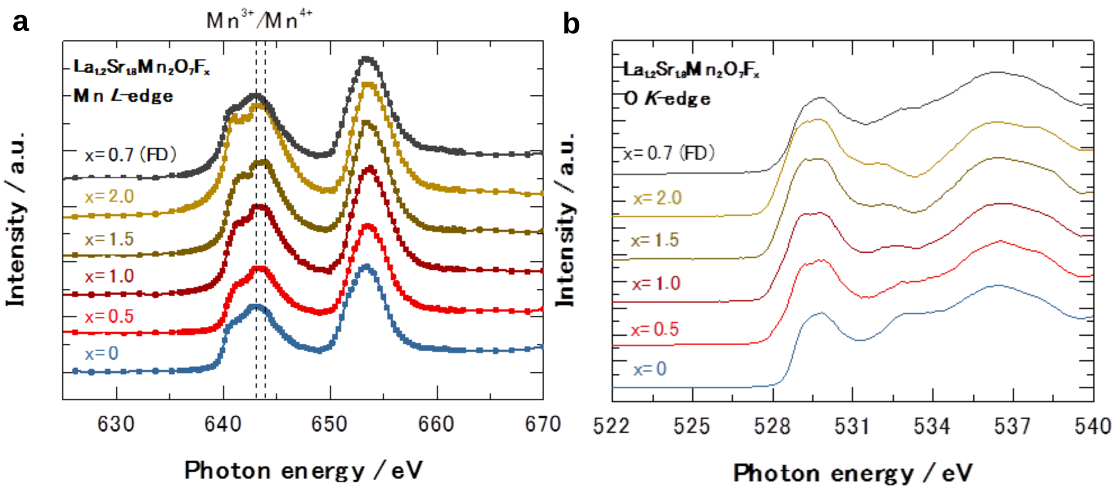

Fig. 3-5. *ex-situ* XANES spectra during charge process. **a,** Mn L-edge and **b,** O K-edge

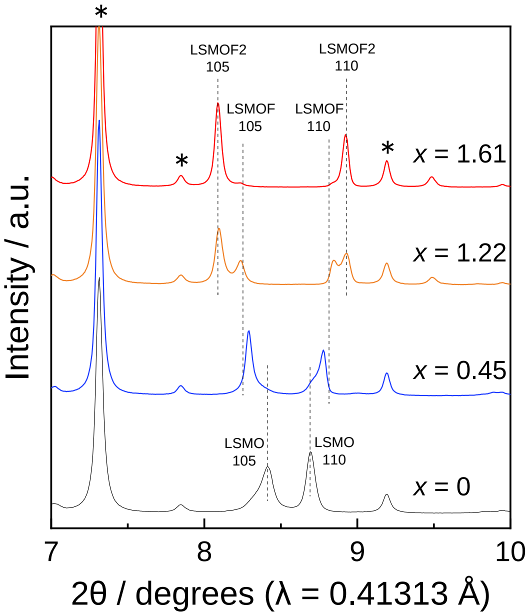

Fig. 3-6. Synchrotron XRD patterns of the $La_{1.2}Sr_{1.8}Mn_2O_7$ cathode during charge process.

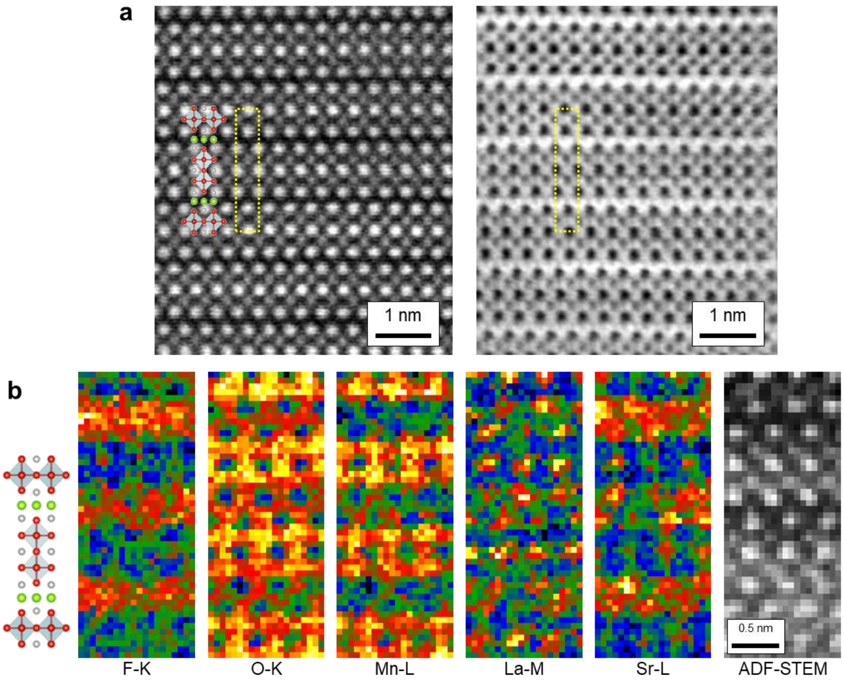

Fig. 3-7. Spherical Aberration (Cs) corrected Scanning Transmission Electron Microscope (Cs-STEM) observations of $La_{1.2}Sr_{1.8}Mn_2O_7$ cathode charged to $x = 1.61$ of $La_{1.2}Sr_{1.8}Mn_2O_7F_x$ viewed along [010]. **a**, High-angle annular dark-field (HAADF) and annular bright-field (ABF) STEM images **b**, Atomic resolution STEM-EELS mapping images. For simplicity, the ideal structures are shown[22].

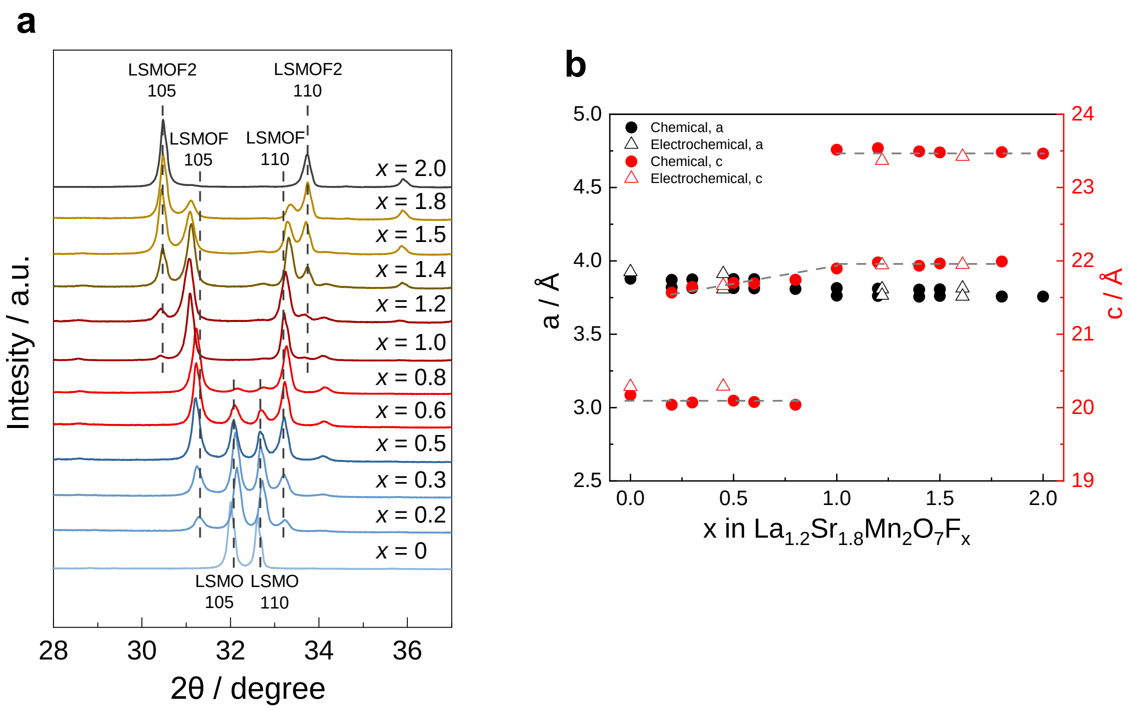

Fig. 3-8. **a**, XRD patterns of $La_{1.2}Sr_{1.8}Mn_2O_7$ oxide after chemical fluorination with different fluorine content *x* of $La_{1.2}Sr_{1.8}Mn_2O_7F_x$. **b**, Lattice constants estimated from XRD patterns of $La_{1.2}Sr_{1.8}Mn_2O_7$ oxide after electrochemical fluorination (**Fig. 3-6**) and chemical fluorination (**Fig. 3-8a**).

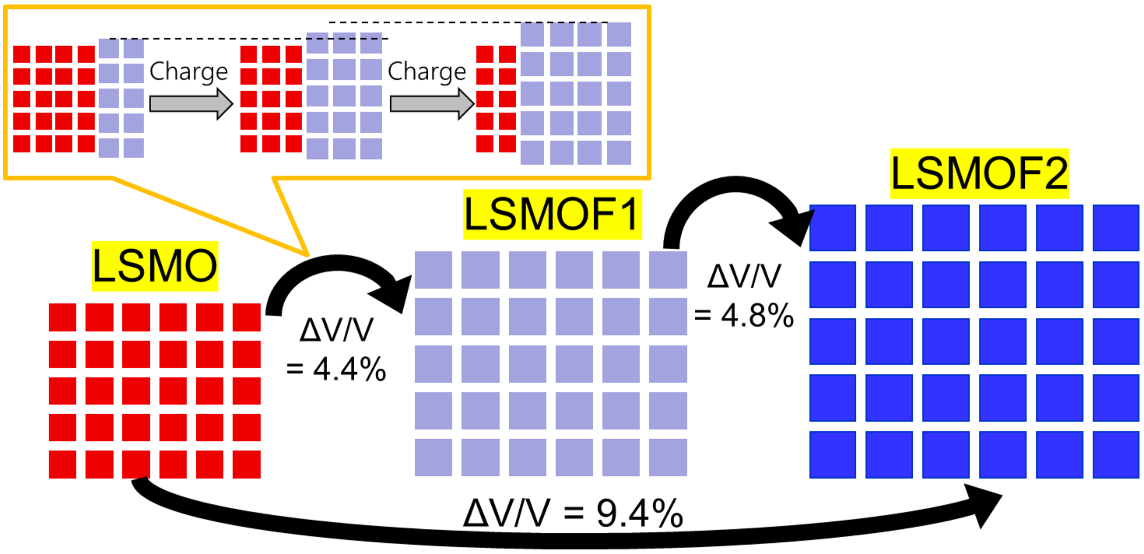

Fig. 3-9. Phase transition scheme during fluoride-ion intercalation reaction of $La_{1.2}Sr_{1.8}Mn_2O_7F_x$ ($0 \leq x \leq 2.0$)

3.5. References

1. M. Armand, J.-M. Tarascon, Building better batteries, *Nature*, **2008**, 451, 652-657.

2. M.A. Reddy, M. Fichtner, Batteries based on fluoride shuttle, *J. Mater. Chem.*, **2011**, 21, 17059-17062.

3. M.D. Slater, D. Kim, E. Lee, C.S. Johnson, Sodium-ion batteries, *Adv. Funct. Mater.*, **2013,** 23, 947-958.

4. P.G. Bruce, S.A. Freunberger, L.J. Hardwick, J.-M. Tarascon, Li-O_2 and Li-S batteries with high energy storage, *Nat. Mater.*, **2012**, 11, 19-29.

5. B. Dunn, H. Kamath, J.-M. Tarascon, Electrical energy storage for the grid: a battery of choices, *Science*, **2011**, 334, 928-935.

6. X. Zhao, S. Ren, M. Bruns, M. Fichtner, Chloride ion battery: a new member in the rechargeable battery family, *J. Power Sources*, **2014**, 245, 706-711.

7. D. Aurbach, Z. Lu, A. Schechter, Y. Gofer, H. Gizbar, R. Turgeman, Y. Cohen, M. Moshkovich, E. Levi, Prototype systems for rechargeable magnesium batteries, *Nature*, **2000**, 407, 724-727.

8. F. Gschwind, G. Rodriguez-Garcia, D. Sandbeck, A. Gross, M. Weil, M. Fichtner, N. Hörmann, Fluoride ion batteries: Theoretical performance, safety, toxicity, and a combinatorial screening of new electrodes, *J. Fluor. Chem.*, **2016**, 182, 76-90.

9. D. T. Thieu, M.H. Fawey, H. Bhatia, T. Diemant, V.S.K. Chakravadhanula, R.J. Behm, C. Kübel, M. Fichtner, CuF_2 as reversible cathode for fluoride ion batteries, *Adv. Funct. Mater.*, **2017**, 27, 1701051.

10. C. Rongeat, M.A. Reddy, T. Diemant, R.J. Behm, M. Fichtner, Development of new anode composite materials for fluoride ion batteries, *J. Mater. Chem. A*, **2014**, 2, 20861-20872.

11. D. Zhang, K. Yamamoto, A. Ochi, Y. Wang, T. Yoshinari, K. Nakanishi, H. Nakano, H. Miki, S. Nakanishi, H. Iba, Understanding the reaction mechanism and

performances of 3d transition metal cathodes for all-solid-state fluoride ion batteries, *J. Mater. Chem. A*, **2021**, 9, 406-412.

12. T. Yoshinari, D. Zhang, K. Yamamoto, Y. Kitaguchi, A. Ochi, K. Nakanishi, H. Miki, S. Nakanishi, H. Iba, T. Uchiyama, Kinetic analysis and alloy designs for metal/metal fluorides toward high rate capability for all-solid-state fluoride-ion batteries, *J. Mater. Chem. A*, **2021**, 9, 7018-7024.

13. Y. Tsujimoto, K. Yamaura, E. Takayama-Muromachi, Oxyfluoride chemistry of layered perovskite compounds, *Appl. Sci*., **2012**, 2, 206-219.

14. H. Miki, K. Yamamoto, H. Nakaki, T. Yoshinari, K. Nakanishi, S. Nakanishi, H. Iba, J. Miyawaki, Y. Harada, A. Kuwabara, Y. Wang, T. Watanabe, T. Matsunaga, K. Maeda, H. Kageyama, Y. Uchimoto, Double-Layered Perovskite Oxyfluoride Cathodes with High Capacity Involving O–O Bond Formation for Fluoride-Ion Batteries, *J. Am. Chem. Soc.* in press, doi.org/10.1021/jacs.3c10871

15. T. Sivakumar, J.B. Wiley, Topotactic route for new layered perovskite oxides containing fluorine: $Ln_{1.2}Sr_{1.8}Mn_2O_7F_2$ (Ln= Pr, Nd, Sm, Eu, and Gd), *Mater. Res. Bull.*, **2009**, 44, 74-77.

16. C. Greaves, J. Kissick, M. Francesconi, L. Aikens, L. Gillie, Synthetic strategies for new inorganic oxide fluorides and oxide sulfates, *J. Mater. Chem.*, **1999**, 9, 111-116.

17. J. Haruyama, K.-i. Okazaki, Y. Morita, H. Nakamoto, E. Matsubara, T. Ikeshoji, M. Otani, Two-Phase Reaction Mechanism for Fluorination and Defluorination in Fluoride-Shuttle Batteries: A First-Principles Study, *ACS Appl. Mater. Interfaces*, **2020**, 12, 428-435.

18. L. Zhang, M.A. Reddy, M. Fichtner, Development of tysonite-type fluoride conducting thin film electrolytes for fluoride ion batteries, *Solid State Ion.*, **2015**, 272, 39-44.

19. C.-X. Zu, H. Li, Thermodynamic analysis on energy densities of batteries, *Energy Environ. Sci*., **2011**, 4, 2614-2624.

20. Y. Zhu, C. Wang, Galvanostatic intermittent titration technique for phase-transformation electrodes, *J. Phys. Chem. C,* **2010**, 114, 2830-2841.

21. L. Aikens, L. Gillie, R. Li, C. Greaves, Staged fluorine insertion into manganese oxides with Ruddlesden–Popper structures: $LaSrMnO_4F$ and $La_{1.2}Sr_{1.8}Mn_2O_7F$, *J. Mater. Chem.*, **2002**, 12, 264-267.

22. K. Momma, F. Izumi. VESTA 3 for three-dimensional visualization of crystal, volumetric and morphology data, *J. Appl. Crystallogr.*, **2011**, 44, 1272–1276.

23. F. Tuerxun, S. Otani, K. Yamamoto, T. Matsunaga, H. Imai, T. Mandai, T. Uchiyama, T. Watanabe, K. Kanamura, Y. Uchimoto, “Phase transition behavior of $MgMn_2O_4$ spinel oxide cathode during magnesium ion insertion”, *Chem. Mater.*, **2021**, 33, 1006–1012.

24. Y. Orikasa, T. Maeda, Y. Koyama, H. Murayama, K. Fukuda, H. Tanida, H. Arai, E. Matsubara, Y. Uchimoto, Z. Ogumi, Transient Phase Change in Two Phase Reaction between $LiFePO_4$ and $FePO_4$ under Battery Operation, *Chem. Mater.*, **2013**, 25, 1032–1039.

25. M. Nishijima, T. Ootani, Y. Kamimura, T. Sueki, S. Esaki, S. Murai, K. Fujita, K. Tanaka, K. Ohira, Y. Koyama, I. Tanaka, Accelerated Discovery of Cathode Materials with Prolonged Cycle Life for Lithium-ion Battery. *Nat. Commun.* **2014**, 5, 4553.

26. T. Yoshinari, K. Yamamoto, M. Nishijima, K. Fukuda, A. Kuwabara, I. Tanaka, K. Maeda, H. Kageyama, Y. Orikasa, and Y. Uchimoto, High rate performance of dual substituted $LiFePO_4$ based on controlling metastable intermediate phase, *ACS Appl. Energy Mater.* **2018**, 1, 6736－6740.

27. M. Yashima, N. Sirikanda, and T. Ishihara, Crystal Structure, Diffusion Path, and Oxygen Permeability of a Pr_2NiO_4-Based Mixed Conductor $(Pr_{0.9}La_{0.1})_2(Ni_{0.74}Cu_{0.21}Ga_{0.05})O_{4+\delta}$, *J. Am. Chem. Soc.* **2010**, 132, 2385–2392.

Chapter 4.

Understanding Ion Diffusion Mechanism and Improving Rate Characteristics in $La_{1.2}Sr_{1.8}Mn_2O_7$

Abstract

In this chapter, we clarified the fluoride-ion diffusion paths and discussed material design guidelines to improve rate characteristics by utilizing their mechanisms. Through precise crystal structure analysis using neutron diffraction and synchrotron X-ray diffraction, we clearly identified the dominant ion diffusion paths from the perspectives of maximum entropy method (MEM), bond valence sum (BVS), and nudged elastic band (NEB) method. As a result, we proposed a new concept that two-dimensional diffusion utilizing only the interstitial sites is advantageous, unlike the conventional O-ion diffusion paths in Ruddlesden-Popper structures[1]. Additionally, we synthesized $La_{1+2x}Sr_{2-2x}Mn_2O_7$ ($0.30 \le x \le 0.48$) with controlled La/Sr ratios to broaden the diffusion paths in the interstitial layers and compared their rate performance. The results showed a good correlation between the interlayer spacing and rate performance, demonstrating that extending the interlayer spacing is an effective means to improve battery performance.

4.1. Introduction

The advanced battery system is a key technology for mitigating carbon dioxide emission for a sustainable society. Presently, the market-dominating lithium-ion batteries (LIBs) are extensively utilized for electrical devices such as superslim microchips, portable phones. By virtue of their high energy density, light weight, and long-term durability, its application is extended in electric vehicles to support the carbon neutral society.[2] However, new rechargeable batteries with higher volumetric energy densities than conventional LIBs are strongly demanded for electric vehicles with longer mileage.

All-solid-state fluoride-ion batteries (FIBs) that use F^- as the charge carrier have attracted a great deal of attention as a next-generation energy storage technology because of their theoretical high volumetric energy density.[3-9] Simple metal/metal fluoride cathodes such as Bi/BiF_3 and Cu/CuF_2 have been much studied as typical cathodes for FIBs.[3-9] However, the inherent large volume change during charge/discharge makes the cycling and rate performance of these materials impractical.[5, 8, 10] Therefore, as with LIBs, the development of materials in which charge/discharge proceeds via topochemical reactions is crucial for FIBs.

Perovskite-related oxides $A_{n+1}B_nO_{3n+1}$ (A: rare-earth or alkaline-earth element; B: transition metal) with Ruddlesden–Popper structure and their oxyfluorides have been investigated as candidates of active cathode materials for FIBs.[11-18] Fluoride-ions can be electrochemically (de)intercalated in the rigid void space between two octahedral layers (so-called interstitial site) of the structure.[11] It has been reported that the volume expansion ratio of such Ruddlesden–Popper intercalation-type cathodes (e.g.,

$LaSrMnO_4$/$LaSrMnO_4F$: 6.22%)[14] is much smaller than that of conversion reaction-type cathodes (e.g., Cu/CuF_2: 195.6%)[8], resulting in superior power density. However, further improvement of the power density of FIBs is required.

We have recently demonstrated that the Ruddlesden-Popper perovskite $La_{1.2}Sr_{1.8}Mn_2O_{7-\delta}F_2$ exhibits high capacity and good cycle performance when used as a cathode in FIBs.[18] Further improvement of its characteristics, particularly in terms of rate performance, is crucial for practical applications. In this study, we focused on ion diffusion in the crystal structure of $La_{1.2}Sr_{1.8}Mn_2O_{7-\delta}F_2$ and investigated the mechanism and enhancement of rate performance. Precise crystal structure analysis was conducted using neutron diffraction and synchrotron X-ray diffraction, which allowed us to visualize the fluoride-ion diffusion paths. The results suggested that two-dimensional diffusion in the interstitial layers is dominant. To enhance the rate performance, we explored the expansion of fluoride-ion pathways. It has been reported that the conductivity of oxide-ion conductors in the Ruddlesden-Popper perovskite structure is improved by substituting the A-site cation.[19] Therefore, we attempted to control the interlayer spacing where fluoride ions are inserted by varying the La/Sr ratio in $La_{2-2x}Sr_{1+2x}Mn_2O_7$, aiming to improve the rate performance. Detailed discussions on the relationship between the results of crystal structure analysis and rate performance will be provided.

4.2. Experimental

4.2.1. Synthesis of Materials

$La_{2-2x}Sr_{1+2x}Mn_2O_7$ (x = 0.25, 0.30, 0.325, 0.35, 0.375, 0.40, 0.48, 0.55) was prepared by using solid-state reaction as previously reported.[20] The lower substitution limit has been reported to be $x \sim 0.25$.[21] La_2O_3 (99.99%, Kojundo Chemical Laboratory), $SrCO_3$ (99.9%, WAKO pure chemical industries, LTD.), and MnO_2 (99.5%, WAKO pure chemical industries, LTD.) were used as starting materials. These materials were mixed with a stoichiometric ratio by hand-mixing. The mixture was then pressed into a pellet and sintered at 1500 °C for 40 h using an aluminum crucible in air to obtain our final product. To prevent direct contact between the crucible and the pellets of the starting material mixture, the powder of the mixture was laid on between the crucible and the pellets. $La_{1.2}Sr_{1.8}Mn_2O_7F$ and $La_{1.2}Sr_{1.8}Mn_2O_7F_2$ intermetallic compounds were synthesized by the chemical fluorination of $La_{1.2}Sr_{1.8}Mn_2O_7$ using thermally evolved F_2 gas from polyvinylidene difluoride (PVDF).[22] That is, 1.0 g of the obtained $La_{1.2}Sr_{1.8}Mn_2O_7$ powder and 1.5 g of PVDF (Aldrich, average M_w: approximately 180,000; average M_n: approximately 71,000) were placed in separate alumina boats and covered with saggar. They were heated at 400 °C for 10 h in air in an electric muffle furnace to generate the two materials. The synthesis of $La_{0.9}Ba_{0.1}F_{2.9}$, which is used as a solid electrolyte, followed the previously reported method[23]. LaF_3 (99.9%, Kojundo Chemical Laboratory) and BaF_2 (99.9%, Kojundo Chemical Laboratory) were used as starting materials, and they were mixed in a molar ratio of 9:1. The mixture was then subjected to ball milling using a planetary ball mill at 600 rpm for 12 hours. Afterward, the obtained mixture was heat-treated at 1000 °C for 4 hours under an argon atmosphere to obtain the sample.

4.2.2. Materials Characterization

Synchrotron X-ray diffraction (SXRD) measurements were performed using the BL02B2 beamline at the Japan Synchrotron Radiation Research Institute (SPring-8). The powders were packed into quartz capillary tubes with an internal diameter of φ0.5. To insulate against the atmosphere, the opening of each capillary was melted and shut using an oxyacetylene frame. High-temperature time-of-flight (TOF) neutron diffraction (ND) measurements were obtained using the special-environment neutron diffractometer super-HRPD located at the BL08 beamline and the total scattering spectrometer NOVA at the BL21 beamline of the Materials and Life Science Experimental Facility, Japan Proton Accelerator Research Complex (J-PARC MLF).[24, 25] The samples were placed in a cylindrical vanadium−nickel-alloy holder (φ6 and t0.1) in a high-purity Ar atmosphere. Rietveld structural refinement and MEM calculations were performed using the analytical programs Jana2006 and Dysnomia.[26, 27] The obtained neutron-scattering length density maps, structural models, and BVS maps were depicted using VESTA.[28]

X-ray diffraction (XRD) measurements of as-prepared materials were performed using Cu Kα radiation at 40 kV and 40 mA (Ultima IV, Rigaku). Rietveld analysis of the obtained XRD profiles was performed using the JANA package.[26] The crystal structure was visualized using the VESTA program.[28] X-ray absorption spectroscopy (XAS) measurements for the Mn *K*-edge were performed at beamline BL14B2 in SPring-8, Japan. All spectra were collected in the transmission mode. The particle morphology of materials was investigated by scanning electron microscopy measurements (S-3400N, HITACHI; JCM-6000, JEOL).

4.2.3. First-Principles Calculations

First-principles total energy calculations based on the density functional theory (DFT) were performed using the projector augmented wave (PAW) method as implemented in the Vienna Ab initio Simulation Package (VASP) code.[29, 30] Valence electron configurations of the PAW potentials were $5s^2$ $5p^6$ $5d^1$ $6s^2$ for La, $4s^2$ $4p^6$ $5s^2$ for Sr, $3s^2$ $3p^6$ $3d^5$ $4s^2$ for Mn, $2s^2$ $2p^4$ for O, and $2s^2$ $2p^5$ for F. Exchange-correlation interactions of electrons was treated based on the framework of the Perdew-Burke-Ernzerhof solid (PBEsol) potential.[31–33] The DFT+U approach was used to account for the strong correlation effects of 3d orbitals with the U value set at 3.0 eV for Mn 3d.[34-36] Because it is difficult to directly compute the structural models of $La_{1.2}Sr_{1.8}Mn_2O_7$ and $La_{1.2}Sr_{1.8}Mn_2O_7F_2$ with partially occupied sites using first-principles calculations, we calculated alternative structural models of $LaSr_2Mn_2O_7$ and $LaSr_2Mn_2O_7F_2$, which are approximate compositions of $La_{1.2}Sr_{1.8}Mn_2O_7$ and $La_{1.2}Sr_{1.8}Mn_2O_7F_2$. Brillouin zones of structural models were sampled using the Monkhorst-Pack scheme.[37] Spacing was 0.3 /Å for energy convergence of 1 me/atom against the numbers of sampling meshes of a Brillouin zone. The cutoff energy for the plane-wave basis set was set to 550 eV. The crystal structures of the calculation models were fully relaxed until all residual forces acting on the atoms were less than 0.02 eV/Å.

First, the La and Sr configurations in $LaSrMn_2O_7$ were determined. The symmetrically independent configurations of a conventional cell of $LaSrMn_2O_7$ were searched using the Clupan code.[38] Six configurations were identified. This process is illustrated in **Fig. 4-1** in the Supplementary Information. A series of total-energy calculations for the $LaSrMn_2O_7$ models shown in **Fig. 4-2** indicates that the models shown in **Fig. 4-1a** was the most stable. We assumed that the cation configurations were not rearranged during electrochemical fluorination. Based on this assumption, the $LaSrMn_2O_7F_2$ model (shown in **Fig. 4-2**) was constructed on the basis of the most stable model of $LaSrMn_2O_7$.

The migration processes of F^- via a vacancy mechanism were investigated using the nudged elastic band (NEB) method.[39] For the NEB calculations, a supercell composed of 3 × 3 × 1-unit cells of $LaSrMn_2O_7F_2$ were constructed. As an initial of F^- ion migration, one F^- vacancy was introduced, and all internal atomic positions were relaxed under the condition that the dimensions of the supercells were fixed. Supercell models of final states of F^- ion migration was constructed in the same manner. The conditions for the electronic structure calculations and optimization of the internal atomic positions were the same as those for the calculations of the unit cell models, except that the cutoff energy for the plane-wave basis was set to 420 eV.

4.2.4. Electrochemical Evaluation

Electrochemical measurements were performed using a pellet-type two-electrode cell. The cathode composite was prepared by mixing the $La_{2-2x}Sr_{1+2x}Mn_2O_7$ powder, the $La_{0.9}Ba_{0.1}F_{2.9}$ powder, and vapor-grown carbon fiber (VGCF) (Showa Denko), with a ratio of 30:60:10 wt%. The cathode composite was prepared by ball-milling $La_{2-2x}Sr_{1+2x}Mn_2O_7$

with $La_{0.9}Ba_{0.1}F_{2.9}$ and VGCF, as used in FIBs.[14,15] The anode composite was prepared by mixing PbF_2 (99.9%, Kojundo Chemical Laboratory Co., LTD.), $La_{0.9}Ba_{0.1}F_{2.9}$, and acetylene black (Showa Denko) with a ratio of 30:60:10 wt%. The cathode composite, the electrolyte, and the anode composite were pressed under a pressure of 40 MPa. The all-solid-state type electrochemical cell was assembled in a glovebox under an Ar atmosphere. The assembled cell was put in a sealed container without air exposure. The charge and discharge measurements were performed at 10–100 mA/g in the voltage range from -1.5 to 1.5 V vs. Pb/PbF_2 at 140 °C (HJ1010SD8, Hokuto Denko Corporation).

4.3. Results and Discussion

4.3.1. Crystal Structure of $La_{2-2x}Sr_{1+2x}Mn_2O_7$

To visualize the ion diffusion pathway in the Ruddlesden-Popper layered perovskite $La_{1.2}Sr_{1.8}Mn_2O_7F_2$, precise crystal structure analysis using ND was conducted. The ND patterns and Rietveld analysis results at 700 K for $La_{1.2}Sr_{1.8}Mn_2O_7F$ (space group: *P4/nmm*) and $La_{1.2}Sr_{1.8}Mn_2O_7F_2$ (space group: *I4/mmm*) are shown in **Fig. 4-3** and **Table 4-1**, and **Fig. 4-4** and **Table 4-2**, respectively. The results were found to be in excellent agreement with the Ruddlesden-Popper layered perovskite structure. $La_{1.2}Sr_{1.8}Mn_2O_7F$ has a structure in which the NaCl layers between the stacked perovskite layers are filled with fluoride ions every other layer, while $La_{1.2}Sr_{1.8}Mn_2O_7F_2$ has a structure in which all layers are filled with fluoride-ions. **Fig. 4-5** shows the results of the MEM analysis based on the ND data. It was revealed that both $La_{1.2}Sr_{1.8}Mn_2O_7F$ and $La_{1.2}Sr_{1.8}Mn_2O_7F_2$ exhibited anisotropic distributions of fluoride ions with spreading along the *ab* plane.

Next, higher temperature measurements were considered to confirm the connectivity of the ion diffusion pathway. However, it was found that sample decomposition occurred above 773 K, so short-time SXRD measurements were performed at high temperatures (**Fig. 4-6~4-8**). As shown in **Fig. 4-9**, the MEM analysis revealed very thin, disk-like distributions of fluoride-ions in the plane at the interlayer gaps in the NaCl slabs of the $La_{1.2}Sr_{1.8}Mn_2O_7F_2$ crystals. This is also in good agreement with the results of the MEM analysis based on the ND measurements. These anion disks were arranged with four-fold rotational symmetry, each one surrounded by the four closest disks located orthogonally, crossing in two diagonal directions. As shown in **Tables 4-1** and **4-2**, the temperature factors determined for fluoride-ions exhibited extremely anisotropic thermal vibrations, with much stronger vibrations in the *ab* plane than along the *c* axis. This strongly suggests that with just a little (electric) energy, fluoride-ions easily move to their closest F atomic positions in the *ab* plane, as also revealed in the MEM maps based on the corresponding neutron scattering length. From the results at 873 K, it appears that when a sufficiently large electric field is applied, fluoride-ions can hop into neighboring anion sites. This conduction mechanism was also verified from the perspective of bond-valence sum (BVS) calculations (**Fig. 4-10**). BVS calculations were performed for $La_{1.2}Sr_{1.8}Mn_2O_7$ (**Table 4-6**). It was shown that fluoride-ions are likely to conduct to closest F anion site along the <110> directions.

Furthermore, we conducted calculations on the ion diffusion barriers using the NEB method. For the calculations, we prepared a model structure called $La_2SrMn_2O_7$ (as described in the experimental section) and performed calculations for both the <110> and

<100> directions. The results of the NEB calculations shown in **Fig. 4-11** clearly indicate that the second pathway required much higher energy than the first one. Therefore, it is believed that fluoride-ion diffusion in $La_{1.2}Sr_{1.8}Mn_2O_7F_n$ (n=0, 1, and 2) occurs through hopping to the nearest neighboring F sites.

One interesting finding from these results so far is that the conduction mechanism of this material involves two-dimensional diffusion through the sites occupied by fluoride-ions. In previous studies on oxide materials with Ruddlesden-Popper structure, it has been reported that excess oxide-ions in the NaCl layers conduct through hopping via apical oxygen sites, which is energetically favorable[1]. In the case of $La_{1.2}Sr_{1.8}Mn_2O_7F$ and $La_{1.2}Sr_{1.8}Mn_2O_7F_2$, however, it was suggested that fluoride-ions conduct through a different mechanism, where apical sites are not directly involved in the anion diffusion in the NaCl layers due to the presence of different anion species and valences.

4.3.2. Crystal Structure of $La_{2-2x}Sr_{1+2x}Mn_2O_7$

Based on the analysis results so far, it has been shown that the diffusion of fluoride-ions is predominantly two-dimensional within the NaCl layers. In order to improve the rate performance, we aimed to expand the pathways for fluoride ions. To achieve this, we synthesized materials by varying the La/Sr ratio in $La_{2-2x}Sr_{1+2x}Mn_2O_7$, with the intention of modifying the interlayer spacing where fluoride ions are inserted. The crystal structures of as-prepared $La_{2-2x}Sr_{1+2x}Mn_2O_7$ were investigated by XRD measurements. **Fig. 4-12a** shows the XRD patterns for representative compositions of x = 0.30, 0.35, 0.40, and 0.48. In the XRD patterns, main peaks were indexed to the tetragonal $I4/mmm$ space group and small impurity peaks were included. The lattice constants of $La_{2-2x}Sr_{1+2x}Mn_2O_7$ are shown in **Fig. 4-12b**, which were calculated by Rietveld analysis (**Fig. 4-13** and **Tables 4-1~4-4**). The lattice constant *c* decreased while the lattice constant *a* remained almost constant with increasing *x*, resulting in a decrease in volume. Such behavior is consistent with previously reported literature.[40] In the Rietveld analysis, deficiencies in La, Sr, and Mn were not identified (**Tables 4-7~4-10**). Both the Mn-O_{ap} and Mn-O_{eq}, which are the distances between Mn and O at apical site and between Mn and O at equatorial site determined from the Rietveld analysis, become shorter with increment of *x* (**Table 4-11**). Moreover, the magnitude of Jahn-Teller distortion Δ_{JT},[41] which is calculated by Mn-O_{ap}/Mn-O_{eq}, decreases with increment of *x* (**Table 4-11**). These results mean that the valence of Mn is increased with increment of *x*. The particle size of the prepared $La_{2-2x}Sr_{1+2x}Mn_2O_7$ was independent of *x* and approximately a few μm, characterized by SEM as shown in **Fig. 4-14**. To examine the electronic state of Mn with the change of La/Sr in $La_{2-2x}Sr_{1+2x}Mn_2O_7$, X-ray absorption near edge structure (XANES) spectra for Mn *K*-edge were collected (**Fig. 4-15**). The XANES spectra for Mn *K*-edge shifted to higher energy with increasing *x*, indicating that the valence state of Mn ions increased with increment of *x*.

4.3.3. Electrochemical Performance of $La_{2-2x}Sr_{1+2x}Mn_2O_7$

Fig. 4-16a and **Fig. 4-17** are the charge/discharge curves of $La_{2-2x}Sr_{1+2x}Mn_2O_7$ with 10 mA g^{-1} at 140 °C. **Fig. 4-16a** shows the charge-discharge curve after activation process by repeating multiple charge-discharge cycles. The charge-discharge curves before and after the activation process are shown in **Fig. 4-17**. The four samples exhibited a large irreversible capacity in the first cycle, followed by a charge-discharge curve with a different shape from that of the first cycle and a reversible charge-discharge capacity. Similar behavior has been observed in Li-rich cathodes in lithium-ion batteries and is referred to as the activation process involving oxygen release and transition metal reduction.[42, 43] The four samples after activation showed a reversible capacity with a plateau of approximately around 0.3 V and 1 V and an additional plateau-like slope below 0.3 V. Since manganese reduction with oxygen release at high voltages occurs during the initial fluoride-ion insertion of $La_{2-2x}Sr_{1+2x}Mn_2O_7$ oxides as in the case of Li-rich cathodes, a plateau may appear below 0.3 V in the charge curve after the activation process. It has been reported that complex phenomena such as oxygen release, transition metal reduction, migration of transition metals, and structure change at the cathode/electrolyte interface occur during the activation process of Li-rich cathodes.[42–45] Since elucidating the mechanism of such a complicated activation process is beyond the scope of this paper, only the electrochemical properties after the activation process are focused on this paper. In $La_{2-2x}Sr_{1+2x}Mn_2O_7$, the theoretical capacity attributed to Mn redox becomes smaller with increase of x value because the valence of Mn increases. However, $La_{1.3}Sr_{1.7}Mn_2O_7$ ($x = 0.35$) showed the highest discharge capacity (57 mAh g^{-1}) among the four samples prepared (**Fig. 4-16a**). The plateaus around 0.3 V and 1 V seen in the four samples indicates possibility of a phase transition. To confirm this, it is reasonable to perform XRD measurements on the samples after electrochemical measurements. However, it was difficult to perform a detailed crystal structural analysis because the $La_{2-2x}Sr_{1+2x}Mn_2O_7$ composite electrode contains twice as much $La_{0.9}Ba_{0.1}F_{2.9}$ solid electrolyte as the $La_{2-2x}Sr_{1+2x}Mn_2O_7$ active material. Therefore, we chemically inserted different amount of fluoride-ion (y) using polyvinylidene difluoride (PVdF) into $La_{1.2}Sr_{1.8}Mn_2O_7$,[46] which is a representative composition, and performed XRD measurements. The results are shown in **Fig. 4-18**. The initial XRD pattern was indexed by the $La_{1.2}Sr_{1.8}Mn_2O_7$ (F=0) phase of space group *I*4/*mmm*. In the XRD pattern at $y = 0.5$, new peaks appeared in addition to the initial state peaks, which were indexed by two phases, $La_{1.2}Sr_{1.8}Mn_2O_7$ (F=0, space group *I*4/*mmm*) and $La_{1.2}Sr_{1.8}Mn_2O_7F$ (F=1, space group *P*4/*nmm*). In the XRD pattern at $y = 1$, the initial $La_{1.2}Sr_{1.8}Mn_2O_7$ (F=0) phase disappeared and only the $La_{1.2}Sr_{1.8}Mn_2O_7F$ (F=1) phase was indexed. The Bragg peak of the $La_{1.2}Sr_{1.8}Mn_2O_7F$ (F=1) phase observed at 31° from $y = 0.5$ to $y = 1.0$ was shifted to the lower angle. These results suggest that from y = 0 to y = 1, a significantly complex phase transition from the $La_{1.2}Sr_{1.8}Mn_2O_7$ (F=0) phase to the $La_{1.2}Sr_{1.8}Mn_2O_7F$ (F=1) phase occurs, which is accompanied by a change in the lattice parameter of the $La_{1.2}Sr_{1.8}Mn_2O_7F$ phase. Although a more detailed analysis of the complex phase transition is a subject for future work, a superlattice structure might be formed in the compositions between $y = 0{\sim}1$. This complex phase transition could trigger the plateau around 0.3 V and 1 V. To examine rate performance of $La_{2-2x}Sr_{1+2x}Mn_2O_7$, the relative capacities, which were obtained by normalizing the capacities at different current densities with the capacity at 10 mA g^{-1}, were compared (**Fig. 4-16b**). As expected the relative capacity was decreased with increasing the current density for $La_{2-2x}Sr_{1+2x}Mn_2O_7$. As depicted in **Fig. 4-16b**, $La_{1.3}Sr_{1.7}Mn_2O_7$ ($x = 0.35$) showed the highest capacity retention at high current density. To be more precise, the $La_{1.3}Sr_{1.7}Mn_2O_7$ ($x = 0.35$) retains almost 60 % of its capacity at 100 mA g^{-1} related to its capacity at 10 mA g^{-1}.

To examine the reason why $La_{1.3}Sr_{1.7}Mn_2O_7$ ($x = 0.35$) shows the highest capacity retention at high current density, the crystal structures of $La_{2-2x}Sr_{1+2x}Mn_2O_7$ were analyzed in detail. The interlayer distance was estimated from the distance between O atoms and La/Sr atoms (**Fig. 4-19a**) based on the results of the Rietveld analysis. Contrary to the monotonous x dependence of the lattice constant c (**Fig. 4-12b**) and Δ_{JT} (**Table 4-5**), the interlayer distance showed a volcano shape to the x value. The interlayer distance firstly increases from 2.35 Å (at $x = 0.30$) to 2.38 Å (at $x = 0.35$). However, with further increases in x, the interlayer distance kept decreasing. The Jahn-Teller distortion becomes continuously smaller with respect to increment of Mn valence (**Table 4-5**), which is favorable for fluoride-ion diffusion. However, the $La_{2-2x}Sr_{1+2x}Mn_2O_7$ with $x = 0.35$ shows the highest capacity retention at high current density (**Fig. 4-16b**), corresponding to the interlayer distance (**Fig. 4-19a**). Therefore, the rate performance is more largely influenced by the interlayer distance than the Jahn-Teller distortion. The expansion of the interlayer distance weakens the coulombic repulsion between fluoride ions and oxide ions, improving kinetics of fluoride-ions intercalation/deintercalation reactions as shown in **Fig. 4-16b** and **Fig. 4-19b**. The relatively large capacity below 0.3 V in the $La_{1.3}Sr_{1.7}Mn_2O_7$ ($x = 0.35$) after the activation as shown in **Fig. 4-16a** and **Fig. 4-17** may be due to the larger interlayer distance compared to the other samples, which facilitates the oxygen release at high voltage, and detail analysis about the activation is a subject for future work.

4.4. Conclusion

We synthesized a series of Ruddlesden-Popper type $La_{2-2x}Sr_{1+2x}Mn_2O_7$ by systematically changing x to control the interlayer distance for improving the kinetics of fluoride-ions intercalation/deintercalation. The interlayer distance showed the maximum at $x = 0.35$, which was proven by X-ray diffraction with detailed Rietveld analysis. The expansion of the interlayer distance suppressed the coulombic repulsion between fluoride ions and oxide ions, promoting the kinetics of fluoride-ions intercalation/deintercalation reactions. Consequently, the $La_{2-2x}Sr_{1+2x}Mn_2O_7$ with $x = 0.35$, shows highest capacity and better rate performance than other cathodes. Our findings would be attributable to the development of active materials with a high-rate performance in FIBs.

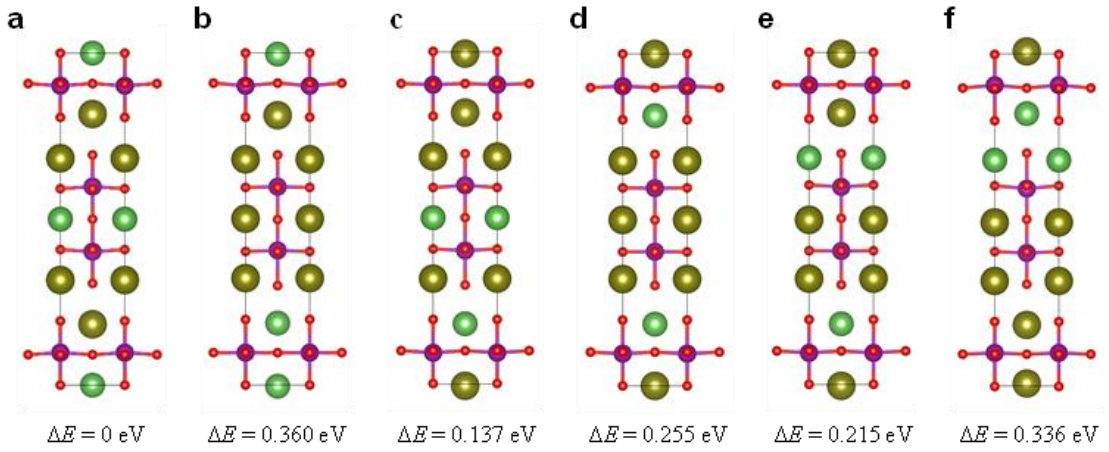

$\Delta E = 0$ eV $\Delta E = 0.360$ eV $\Delta E = 0.137$ eV $\Delta E = 0.255$ eV $\Delta E = 0.215$ eV $\Delta E = 0.336$ eV

Fig. 4-1. Symmetrically independent configurations of La and Sr in the conventional cell of $LaSr_2Mn_2O_7$ searched by the clupan code. ΔE means relative energy per formula unit compared to the most stable configuration shown in the panel **a.**

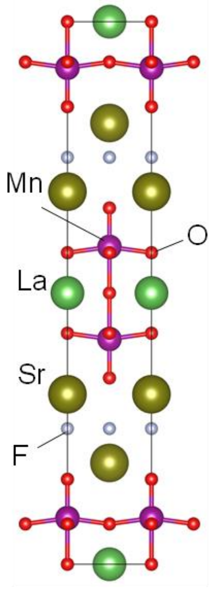

Fig. 4-2. The conventional cell model of $La_{1.2}Sr_{1.8}Mn_2O_7F_2$ in the present study.

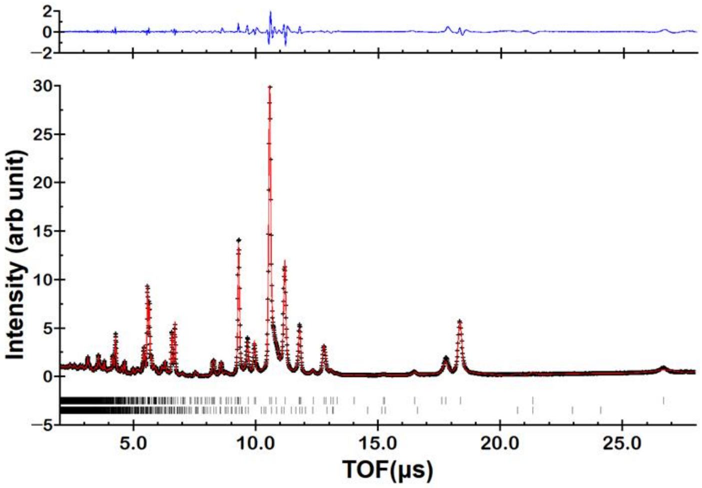

Fig. 4-3. Rietveld analysis results of $La_{1.2}Sr_{1.8}Mn_2O_7F$ performed using neutron diffraction data taken at 700 K. Observed (+), calculated (red line), and difference (observed minus calculated), which appears at the top of the figure in blue. This $La_{1.2}Sr_{1.8}Mn_2O_7F$ specimen contains a small amount of impurity phase; which is $LaSr(MnO_4)F$ itself, or a crystalline material isostructural with $LaSr(MnO_4)F$. The tick marks show the diffraction peak positions of $La_{1.2}Sr_{1.8}Mn_2O_7F$ (upper) and $LaSr(MnO_4)F$ (lower).

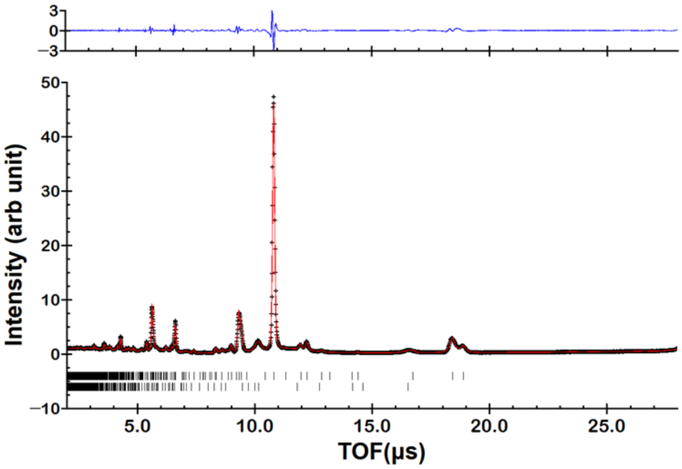

Fig. 4-4. Rietveld analysis results of $La_{1.2}Sr_{1.8}Mn_2O_7F_2$ performed using neutron diffraction data taken at 700 K. Observed (+), calculated (red line), and difference (observed minus calculated), which appears at the top of the figure in blue. This $La_{1.2}Sr_{1.8}Mn_2O_7F_2$ specimen contains, as well in $La_{1.2}Sr_{1.8}Mn_2O_7F$, a small amount of impurity phase, which is FLaO itself, or a crystalline material isostructural with FLaO. The tick marks are the diffraction peak positions of $La_{1.2}Sr_{1.8}Mn_2O_7F_2$ (upper) and FLaO (lower).

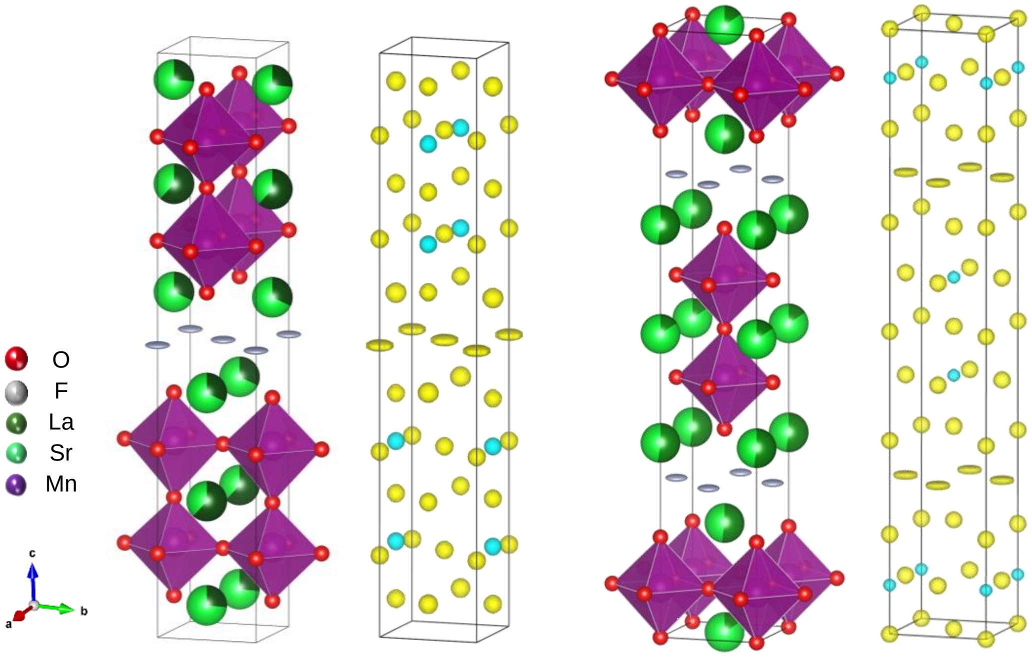

(a) (b) (c) (d)

Fig. 4-5. (a), (c) Crystal structures of $La_{1.2}Sr_{1.8}Mn_2O_7F$ and $La_{1.2}Sr_{1.8}Mn_2O_7F_2$ determined with ND data obtained at 700 K. Thermal ellipsoids are shown only for F. (b), (d) MEM analysis results (isosurface level = 5.0 fm/$\mathbf{a_0^3}$). Mn has negative scattering length, which is shown in light blue.

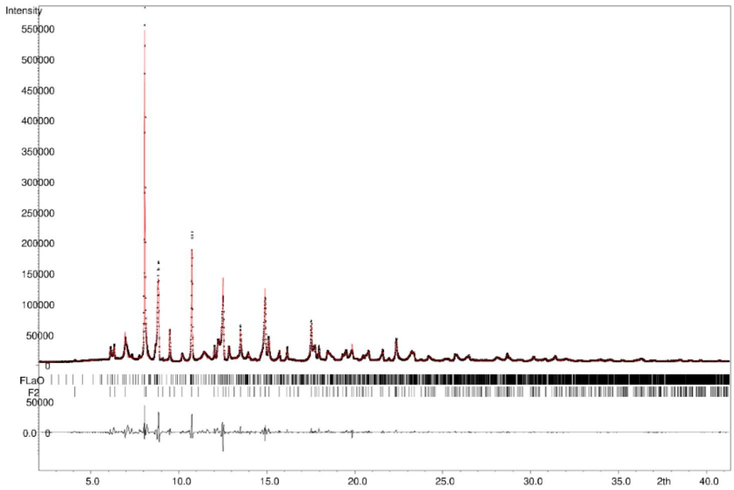

Fig. 4-6. Rietveld analysis results of $La_{1.2}Sr_{1.8}Mn_2O_7F_2$ conducted using X-ray diffraction data taken at RT. Observed (+), calculated (red line), and difference (observed minus calculated), which appears at the top of the figure in blue. This $La_{1.2}Sr_{1.8}Mn_2O_7F_2$ specimen contains a small amount of impurity phase, which is FLaO itself, or a crystalline material isostructural with FLaO. The tick marks show the diffraction peak positions of $La_{1.2}Sr_{1.8}Mn_2O_7F_2$ (lower) and FLaO (upper).

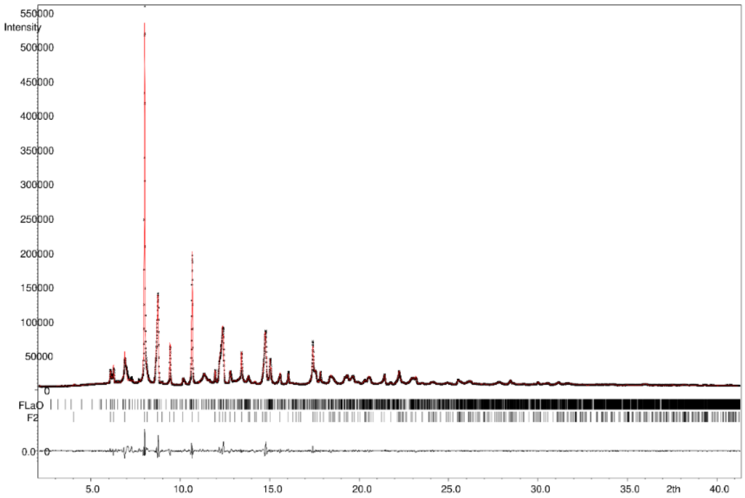

Fig. 4-7. Rietveld analysis results of $La_{1.2}Sr_{1.8}Mn_2O_7F_2$ conducted using X-ray diffraction data taken at 773 K. Observed (+), calculated (red line), and difference (observed minus calculated), which appears at the top of the figure in blue. This $La_{1.2}Sr_{1.8}Mn_2O_7F_2$ specimen contains a small amount of impurity phase, which is FLaO itself, or a crystalline material isostructural with FLaO. The tick marks show the diffraction peak positions of $La_{1.2}Sr_{1.8}Mn_2O_7F_2$ (lower) and FLaO (upper).

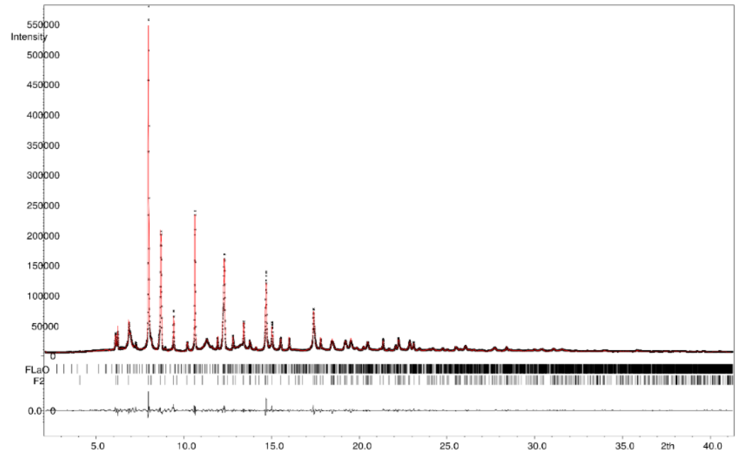

Fig. 4-8. Rietveld analysis results of $La_{1.2}Sr_{1.8}Mn_2O_7F_2$ conducted using X-ray diffraction data taken at 873 K. Observed (+), calculated (red line), and difference (observed minus calculated), which appears at the bottom of the figure. This $La_{1.2}Sr_{1.8}Mn_2O_7F_2$ specimen contains a small amount of impurity phase, which is FLaO itself, or a crystalline material isostructural with FLaO. The tick marks are the diffraction peak positions of $La_{1.2}Sr_{1.8}Mn_2O_7F_2$ (lower) and FLaO (upper).

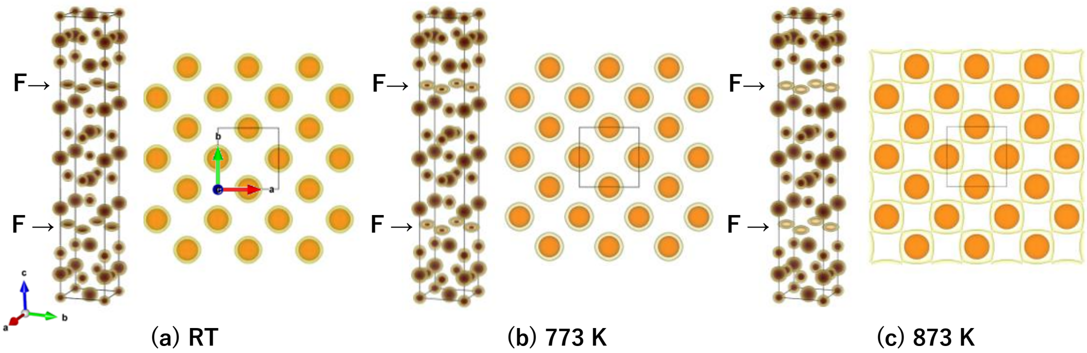

(a) RT (b) 773 K (c) 873 K

Fig. 4-9. Electron density maps of $La_{1.2}Sr_{1.8}Mn_2O_7F_2$ at (a) RT, (b) 773 K, and (c) 873 K obtained through the MEM analyses using their SXRD data shown in **Fig. 4-6~4-9** and **Table 4-3~4-5** (isosurface levels = 10.0, 5.0, and 2.5 e/Å^3, painted in dark brown, orange, and yellow).

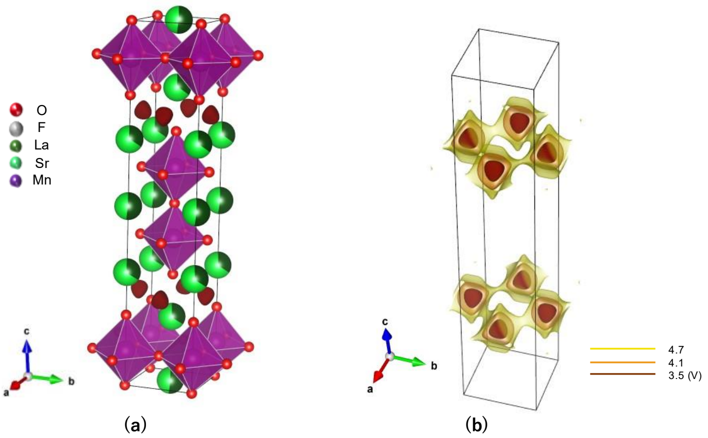

Fig. 4-10. Isosurfaces showing the difference from -1, which is the formal charge of F, obtained by the BVS calculation for $La_{1.2}Sr_{1.8}Mn_2O_7$. BVS mapping of $La_{1.2}Sr_{1.8}Mn_2O_7$ calculated as target ion is **F^-** shows mobility of F anion in the framework. (a) Structure model of $La_{1.2}Sr_{1.8}Mn_2O_7$ and BVS map depicted at isosurface level = 3.5 V shows that inserted **F^-** ions fall into deep Coulombic potential holes painted by dark brown to stay and form $La_{1.2}Sr_{1.8}Mn_2O_7F$ and $La_{1.2}Sr_{1.8}Mn_2O_7F_2$. (b) Once given sufficient energies to these **F^-** ions through charge/discharge process, it is considered getting very likely for them to move to neighboring F sites through Coulomb potential trough shown by yellow along <110> direction.

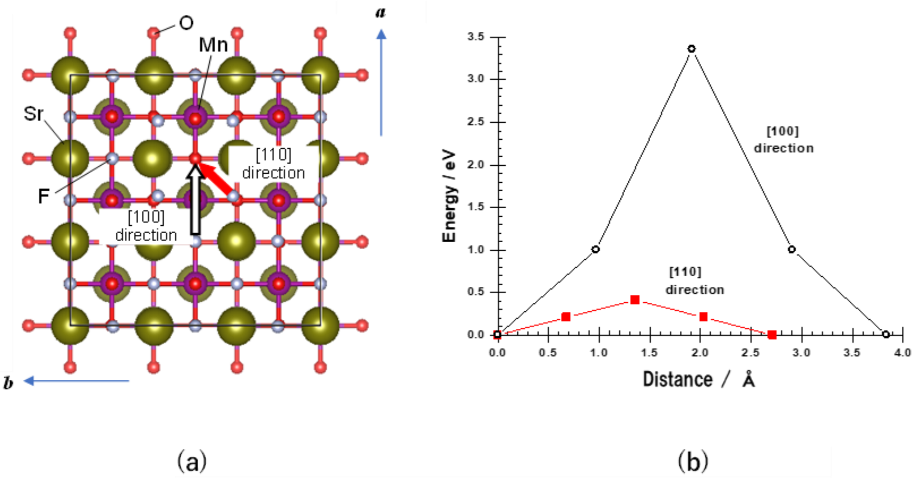

Fig. 4-11. Atomic configurations nearby (a) F^- ion vacancy in the $LaSr_2Mn_2O_7F_2$ supercell model and (b) energy profiles during F^- ion migration in the directions of [100] and [110] via vacancy mechanisms obtained by first-principles NEB calculations.

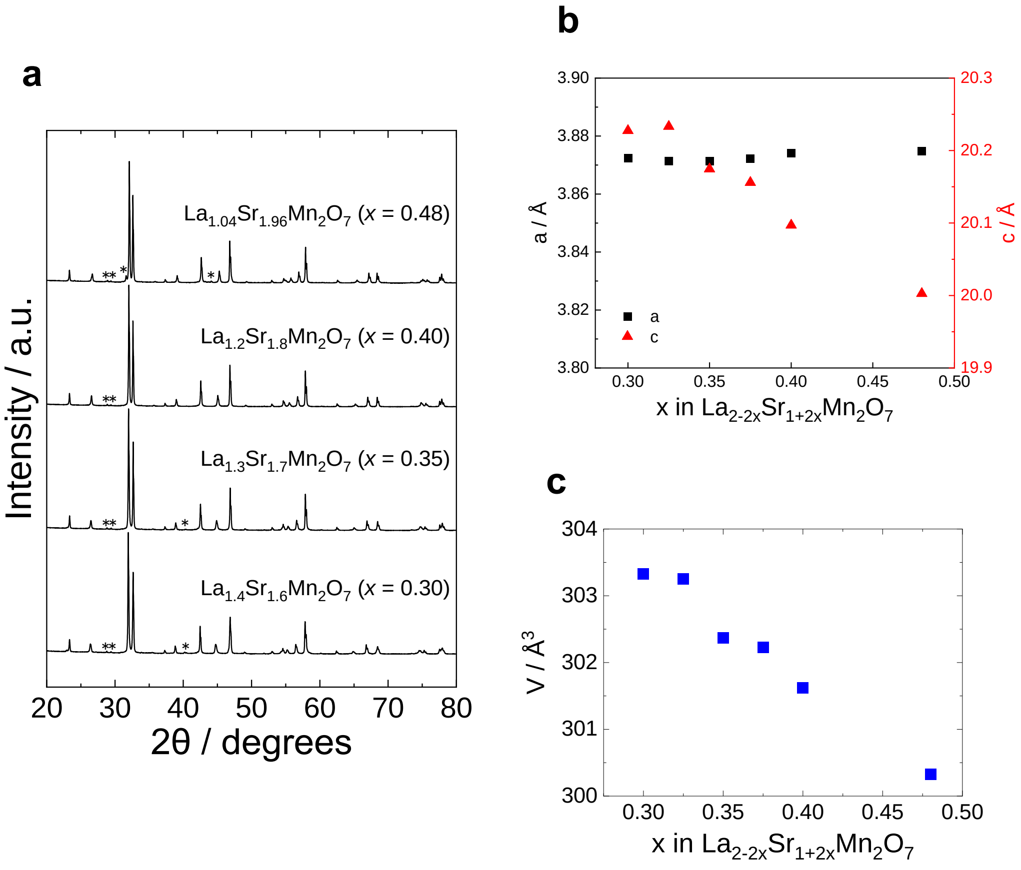

Fig. 4-12. Crystal structure of $La_{2-2x}Sr_{1+2x}Mn_2O_7$ ($x = 0.30, 0.325, 0.35, 0.375, 0.40, 0.48$). **a**, X-ray diffraction patterns of $x = 0.30$, 0.35, 0.40, and 0.48, **b**, lattice constants *a*, *c* and **c**, cell volume as a function of *x* in $La_{2-2x}Sr_{1+2x}Mn_2O_7$. The asterisk means impurity in **Fig. 4-12a**.

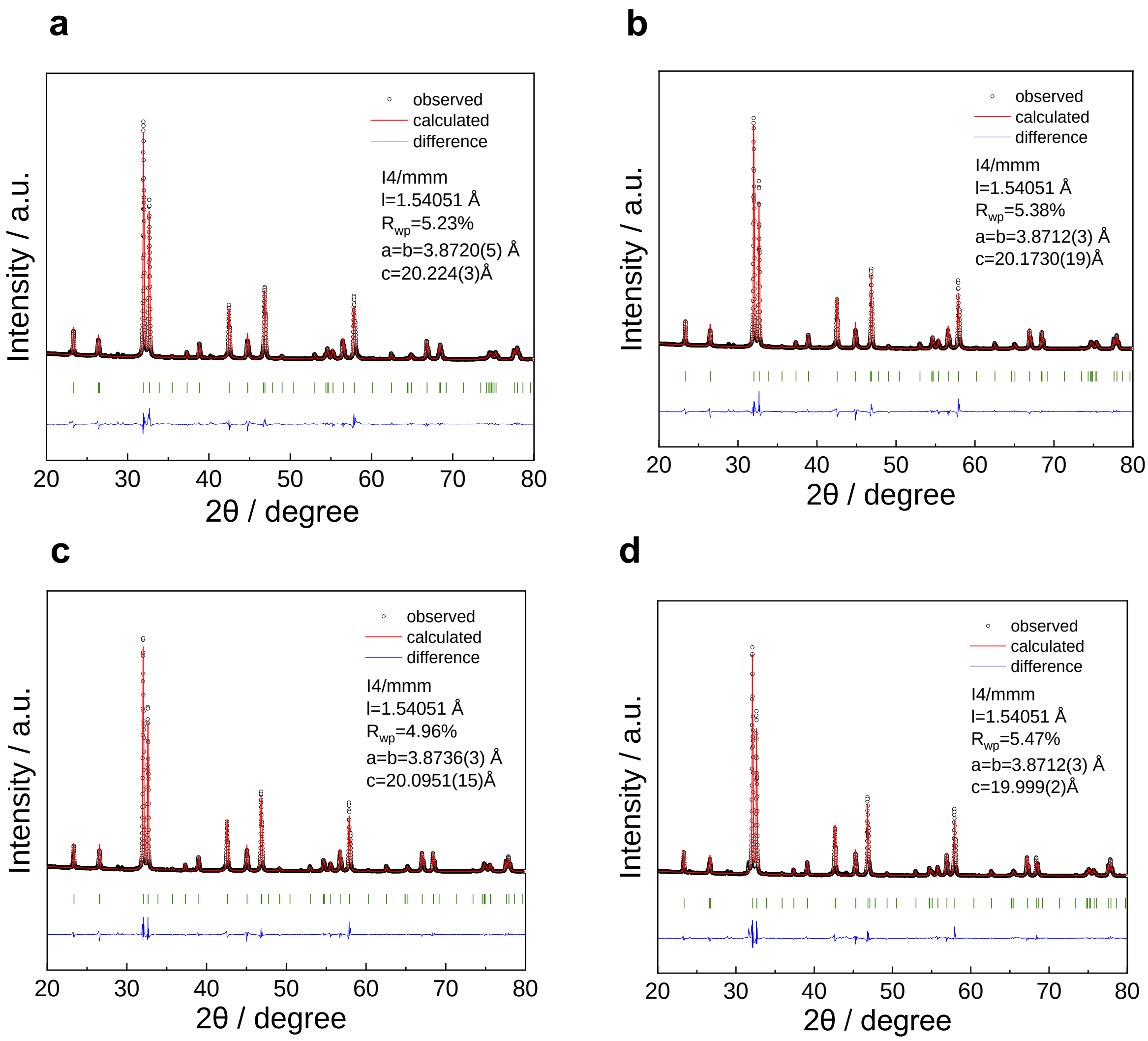

Fig. 4-13. XRD patterns for the as-prepared La$_{2-2x}$Sr$_{1+2x}$Mn$_2$O$_7$ and Rietveld fitting results. **a**, x = 0.30, **b**, x = 0.35, **c**, x = 0.40, and **d**, x = 0.48. The circles and black line denote the observed and calculated intensities, respectively. Short vertical lines indicate the positions of possible Bragg reflections. The difference between the observed and calculated profiles is shown at the bottom. The asterisk means impurity.

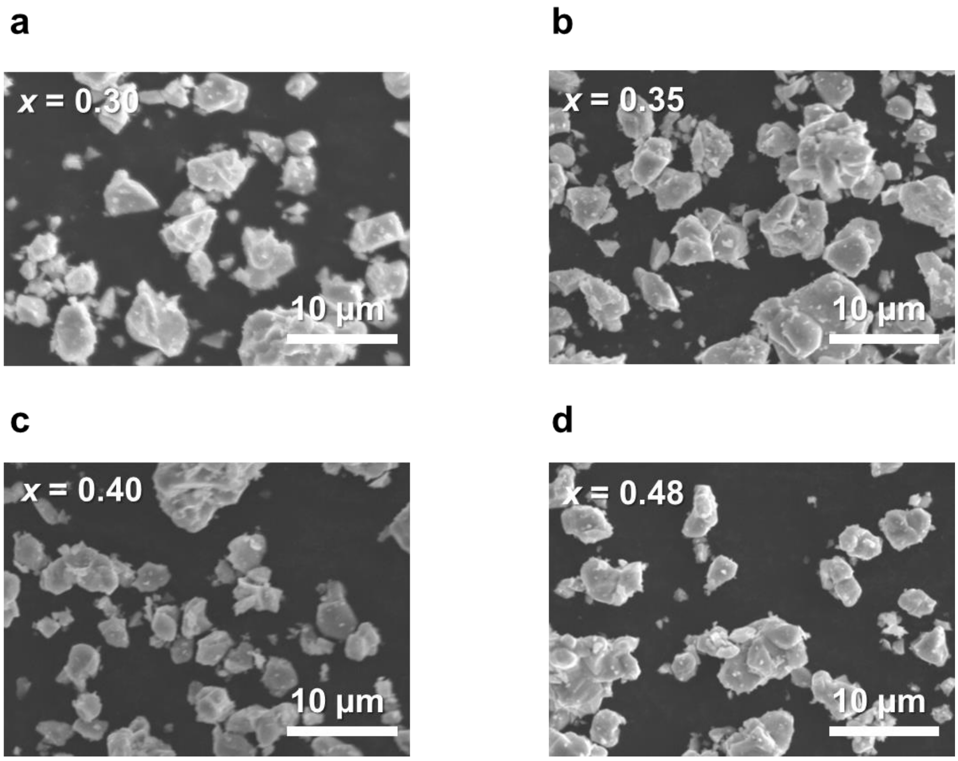

Fig. 4-14. SEM images of $La_{2-2x}Sr_{1+2x}Mn_2O_7$ with **a**, $x = 0.30$, **b**, $x = 0.35$, **c**, $x = 0.40$, and **d**, $x = 0.48$.

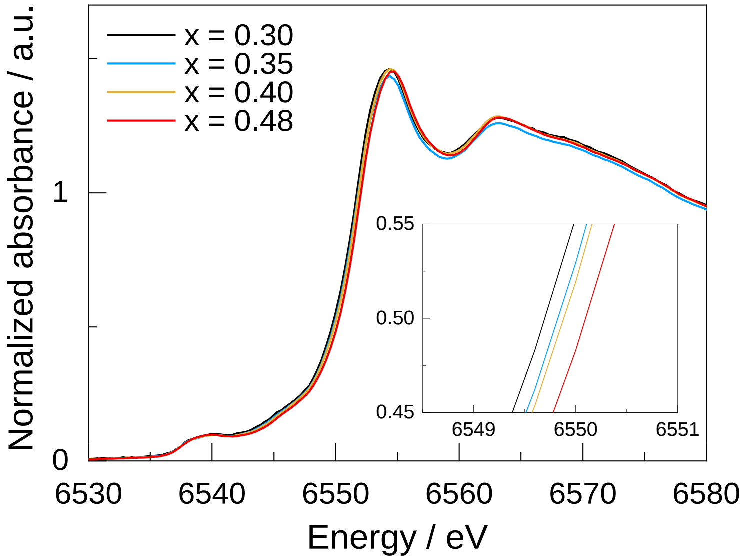

Fig. 4-15. XANES spectra for Mn *K*-edge of $La_{2-2x}Sr_{1+2x}Mn_2O_7$ (x = 0.30, 0.35, 0.40, 0.48).

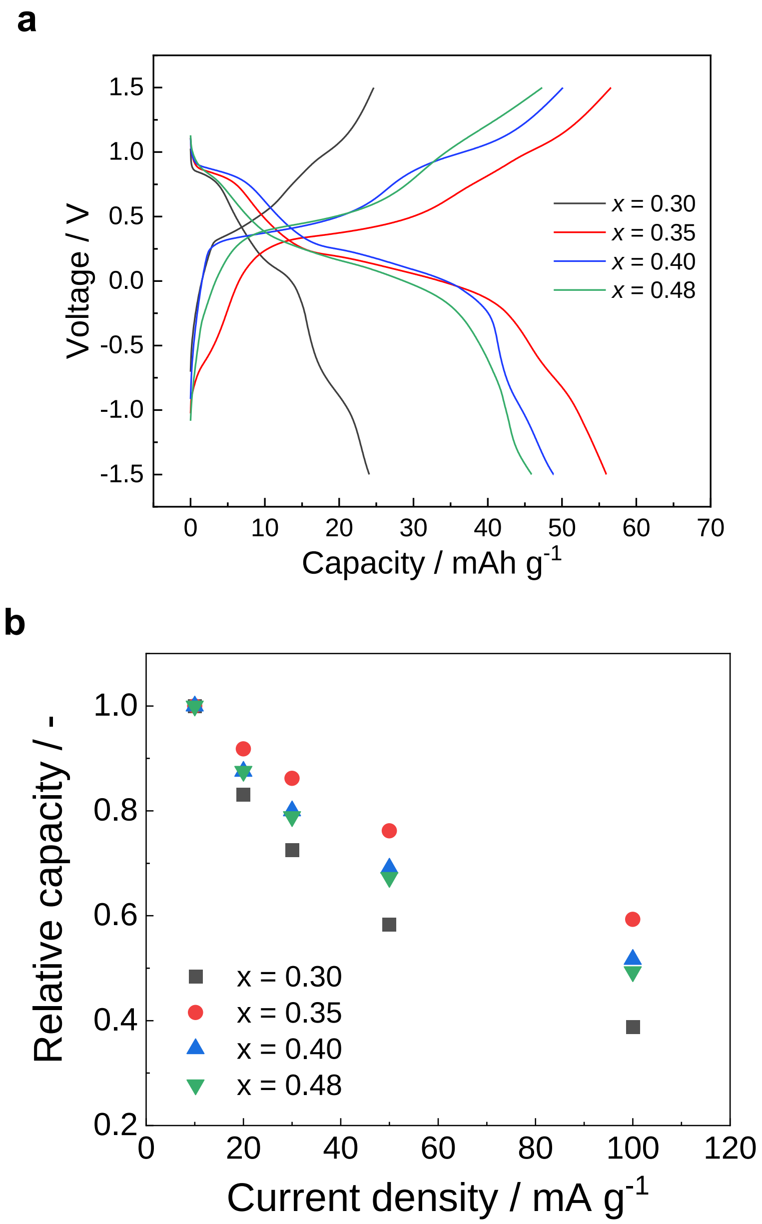

Fig. 4-16. Rate performance of $La_{2-2x}Sr_{1+2x}Mn_2O_7$ (x = 0.30, 0.35, 0.40, 0.48). **a**, Charge and discharge curves at 10 mA/g and **b**, relative capacity at various current densities.

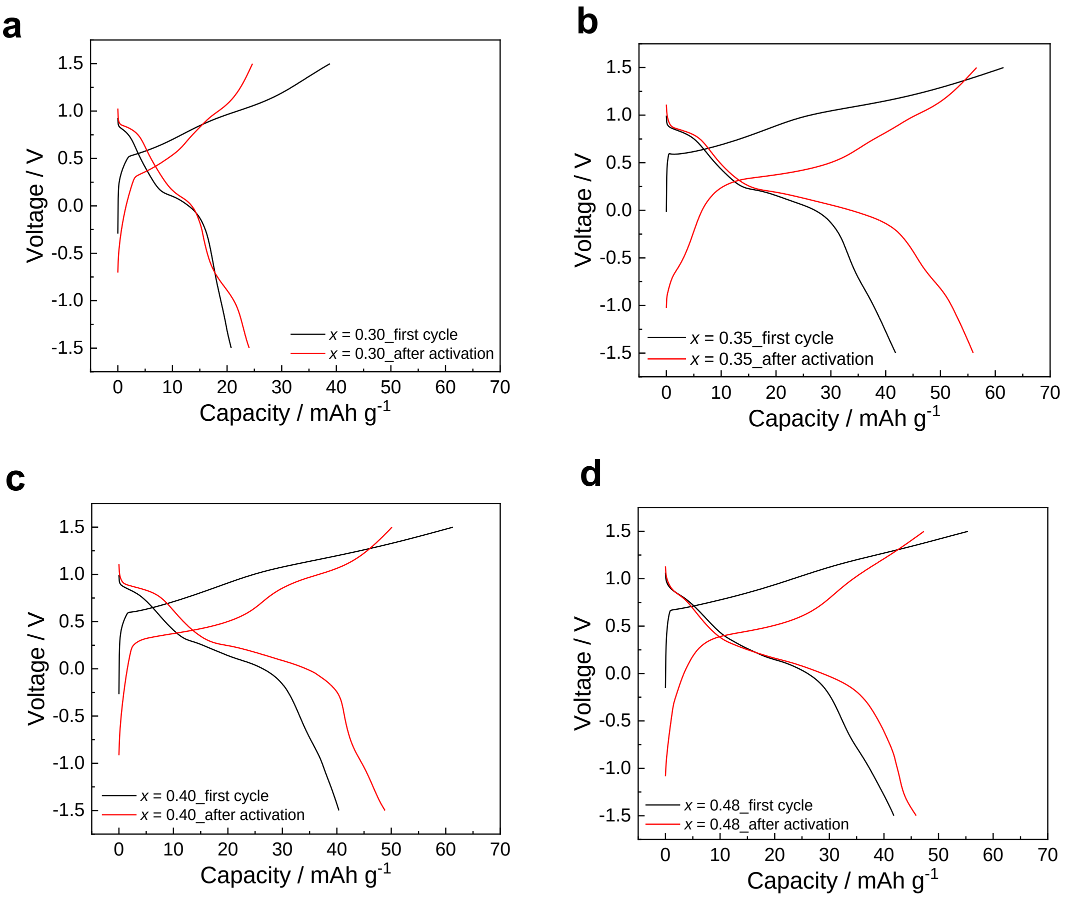

Fig. 4-17. Charge and discharge curves of La$_{2\text{-}2x}$Sr$_{1+2x}$Mn$_2$O$_7$ with **a**, $x = 0.30$, **b**, 0.35, **c**, 0.40, **d**, 0.48 at first cycle and after activation process under 10 mA/g.

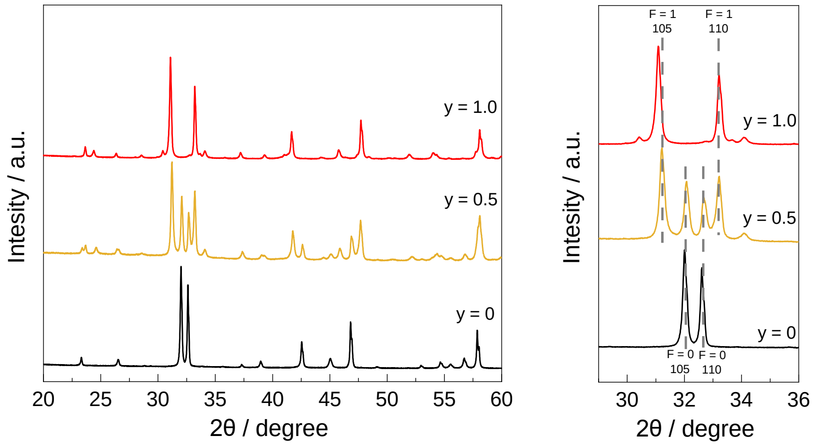

Fig. 4-18. XRD patterns of La$_{1.2}$Sr$_{1.8}$Mn$_2$O$_7$ oxide after chemical fluorination with different fluorine content y.

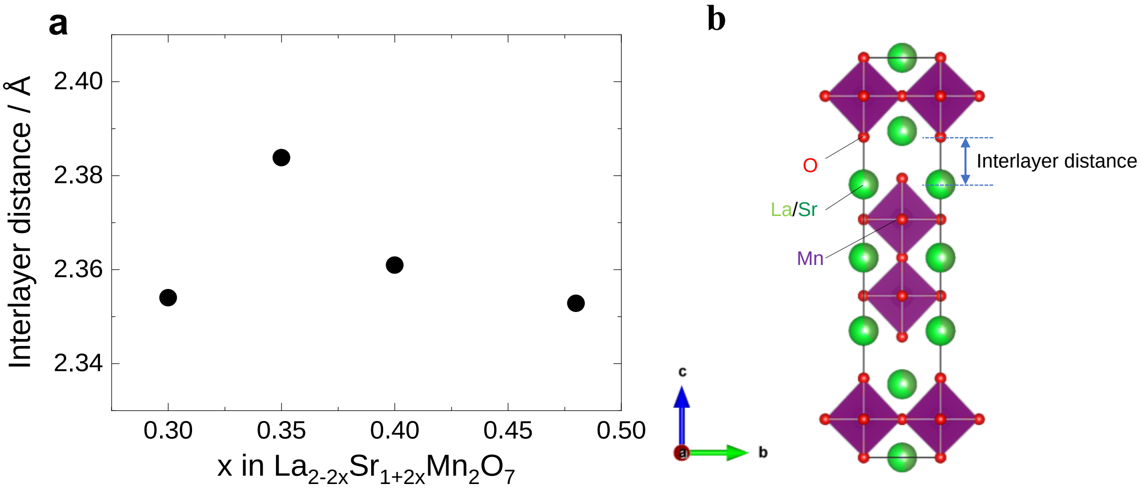

Fig. 4-19. **a**, Interlayer distance as a function of *x* in $La_{2-2x}Sr_{1+2x}Mn_2O_7$ and **b**, crystal structure featuring the interlayer distance.

Table 4-1. Structural parameters determined from the Rietveld structural analysis with ND data taken at 700 K on $La_{1.2}Sr_{1.8}Mn_2O_7F$. *P*4/*nmm*; $a= b= 3.8336(2)$ Å, $c= 21.917(3)$ Å, $\alpha= \beta= \gamma= 90°$, $V= 322.10(5)$ Å^3. Standard deviations are shown in parentheses. $R_p= 5.85$, $_wR_p= 8.66$, $R_{Fobs}= 1.25$, and $R_{Fwobs}= 1.94$ (%). It was assumed that La and Sr atoms completely occupy their respective La/Sr sites and Mn atoms are completely located at their two 2*c* site. By adopting anisotropic temperature factors only for F- ions, the structural refinements were performed to obtain more precise 3D distribution on them.

Atom	x	Y	z	*B* (x10^{-2} Å^2)	*m*	Occ.
La1	¼	¼	0.2362(7)	0.9(5)	2*c*	0.60(8)
Sr1	¼	¼	0.2362(7)	2.9(7)	2*c*	0.40(8)
La2	¼	¼	0.4233(8)	0.9(5)	2*c*	0.18(6)
Sr2	¼	¼	0.4233(8)	2.9(7)	2*c*	0.82(6)
La3	¼	¼	0.0613(8)	0.9(5)	2*c*	0.42(10)
Sr3	¼	¼	0.0613(8)	2.9(7)	2*c*	0.58(10)
Mn1	¾	¾	0.1509(18)	2.2(4)	2*c*	1
Mn2	¾	¾	0.3229(15)	2.2(4)	2*c*	1
O1	¾	¼	0.1413(7)	1.80(11)	4*f*	1.00(2)
O2	¾	¼	0.3187(8)	1.80(11)	4*f*	1
O3	¾	¾	0.0528(15)	1.80(11)	2*c*	1
O4	¾	¾	0.2330(16)	1.80(11)	2*c*	0.92(4)
O5	¾	¾	0.4058(15)	1.80(11)	2*c*	0.88(4)
F1	¾	¼	½	B_{ij}	2*b*	0.87(5)

↓

$B_{11}=B_{22}=0.120(15)$, $B_{33}=0.0003(6)$, $B_{12}=B_{23}=B_{13}= 0$ (Å^2)

Table 4-2. Structural parameters determined from the Rietveld structural analysis with ND data taken at 700 K for $La_{1.2}Sr_{1.8}Mn_2O_7F_2$. *I4/mmm*; $a= b=$ 3.8345(4) Å, $c=$ 23.249(5) Å, $\alpha= \beta= \gamma=$ 90°, $V=$ 341.84(9) Å^3. Standard deviations are shown in parentheses. $R_p=$ 5.45, $_wR_p=$ 8.83, $R_{Fobs}=$ 1.32, and $R_{Fwobs}=$ 2.35 (%). It is assumed that La and Sr atoms completely occupy their respective La/Sr sites and Mn atoms are completely located at their 4*e* site. About 2% vacancies were observed at the 4*d* F anion site. By adopting anisotropic temperature factors only for F^- ions same as $La_{1.2}Sr_{1.8}Mn_2O_7F$, structural refinements were performed to obtain more precise 3D distribution on them.

Atom	*x*	*y*	*z*	*B* (Å^2)	*m*	Occ.
A1	0	0	0.3202(5)	1.41(4)	4*e*	0.38(5)
Sr1	0	0	0.3202(5)	1.41(4)	4*e*	0.62(5)
La2	0	0	½	1.41(4)	2*b*	0.45(10)
Sr2	0	0	½	1.41(4)	2*b*	0.55(10)
Mn1	0	0	0.0815(13)	0.81(13)	4*e*	1
O1	0	½	0.4141(5)	2.21(3)	8*g*	0.96(2)
O2	0	0	0	2.21(3)	2*a*	1
O3	0	0	0.1642(7)	2.21(3)	4*e*	0.98(3)
F1	0	½	¼	B_{ij}	4*d*	0.978(19)

↓

$B_{11}=B_{22}=0.100(4)$, $B_{33}=0.0001(1)$, $B_{12}=B_{23}=B_{13}=0$ (Å^2)

Table 4-3. Structural parameters obtained from the Rietveld analysis performed with the X-ray diffraction data of $La_{1.2}Sr_{1.8}Mn_2O_7F_2$ taken at RT; *I4/mmm*: $a= b= 3.7867(8)$ Å, $c= 23.255(5)$ Å, $\alpha= \beta=\gamma= 90°$, $V= 333.45(14)$ Å^3. Standard deviations are shown in parentheses. $R_p= 5.34$, $_wR_p= 8.60$, $R_{Fobs}= 1.60$, and $R_{Fwobs}= 2.81$ (%). It is assumed that La and Sr atoms completely occupy their respective La/Sr sites and Mn atoms are completely located at their 4*e* site. By adopting anisotropic temperature factors only for F^- ions, the same as in the ND analyses, structural refinements were performed to obtain more precise 3D distribution on them. It is difficult to find a very few vacancies for light atoms, O and F, by X-ray diffraction method; we assumed that they are fully occupied their atomic sites.

Atom	*x*	*y*	*z*	*B* (Å^2)	*m*	Occ.
La1	0	0	0.32099(2)	0.7191(7)	4*e*	0.3802(1)
Sr1	0	0	0.32099	0.7191	4*e*	0.6198
La2	0	0	½	0.7191	2*b*	0.4396(2)
Sr2	0	0	½	0.7191	2*b*	0.5604
Mn1	0	0	0.0864(2)	0.7191	4*e*	1
O1	0	½	0.4243(3)	1.49(4)	8*g*	1
O2	0	0	0.1604(7)	1.49	4*e*	1
O3	0	0	0	1.49	2*a*	1
F1	0	½	¼	B_{ij}	4*d*	1

↓

$B_{11}=B_{22}= 0.088(4)$, $B_{33}= 0.00002(18)$, $B_{12}=B_{23}=B_{13}= 0$ (Å^2)

Table 4-4. Structural parameters obtained from the Rietveld analysis performed with the X-ray diffraction data of $La_{1.2}Sr_{1.8}Mn_2O_7F_2$ taken at 773 K; *I*4/*mmm*: using X-ray diffraction data taken at 773 K; $a = b =$ 3.8294(2) Å, $c =$ 23.292(2) Å, $\alpha = \beta = \gamma =$ 90°, $V =$ 341.55(3) Å^3. Standard deviations are shown in parentheses. $R_p =$ 4.03, $_wR_p =$ 6.12, and $R_{Fobs} =$ 1.60, and $R_{Fwobs} =$ 3.40 (%). It is assumed that La and Sr atoms completely occupy their respective La/Sr sites and Mn atoms are completely located at their 4*e* site. By adopting anisotropic temperature factors only for F^- ion the same as in the ND analyses, structural refinements were performed to obtain more precise 3D distribution on them. It is difficult to find a very few vacancies for light atoms, O and F, by X-ray diffraction method; we assumed that they are fully occupied their atomic sites.

Atom	*x*	*y*	*z*	*B* (Å^2)	*m*	Occ.
La1	0	0	0.32112(1)	0.825(1)	4*e*	0.3742(1)
Sr1	0	0	0.32112(1)	0.825	4*e*	0.6258
La2	0	0	½	0.825	2*b*	0.4517(2)
Sr2	0	0	½	0.825	2*b*	0.5483
Mn1	0	0	0.0836(1)	0.825	4*e*	1
O1	0	½	0.4280(2)	1.75(2)	8*g*	1
O2	0	0	0.1645(4)	1.75	4*e*	1
O3	0	0	0	1.75	2*a*	1
F1	0	½	¼	B_{ij}	4*d*	1

↓

$B_{11} = B_{22} =$ 0.157(4), $B_{33} =$ 0.0007(2), $B_{12} = B_{23} = B_{13} =$ 0 (Å^2)

Table 4-5. Structural parameters obtained from the Rietveld analysis performed with the X-ray diffraction data of $La_{1.2}Sr_{1.8}Mn_2O_7F_2$ taken at 873 K; I4/mmm: a= b= 3.8492(5) Å, c= 23.226(3) Å, α= β= γ= 90°, V= 344.13(8) Å^3. Standard deviations are shown in parentheses. R_p= 3.79, $_wR_p$= 5.45, R_{Fobs}= 1.05, and R_{Fwobs}= 1.61 (%). It is assumed that La and Sr atoms completely occupy their respective La/Sr sites and Mn atoms are completely located at their 4*e* site. About 2% vacancies were observed at the 4d F anion site. By adopting anisotropic temperature factors only for F^- ions the same as in the ND analyses, structural refinements were performed to obtain more precise 3D distribution on them. It is difficult to find a very few vacancies for light atoms, O and F, by X-ray diffraction method; we assumed that they are fully occupied their atomic sites.

Atom	x	y	z	B (Å^2)	m	Occ.
La1	0	0	0.32075(1)	1.59(18)	4*e*	0.3803(2)
Sr1	0	0	0.32075	1.59	4*e*	0.6197
La2	0	0	½	1.59	2*b*	0.4394(4)
Sr2	0	0	½	1.59	2*b*	0.5606
Mn1	0	0	0.0858(1)	1.59	4*e*	1
O1	0	½	0.4183(2)	1.87(15)	8*g*	1
O2	0	0	0.1629(4)	1.87	4*e*	1
O3	0	0	0	1.87	2*a*	1
F1	0	½	¼	B_{ij}	4*d*	1

↓

B_{11}=B_{22}=0.298(3), B_{33}=0.00006(16) , B_{12}=B_{23}=B_{13}= 0 (Å^2)

Table 4-6. Structural parameters determined from the Rietveld structural analysis of the X-ray diffraction data taken at RT for $La_{1.2}Sr_{1.8}Mn_2O_7$; *I4/mmm*: $a= b=$ 3.8874(2) Å, $c=$ 20.099(1) Å, $\alpha= \beta= \gamma=$ 90°, $V=$ 303.74(3) Å^3. Standard deviations are shown in parentheses. R_p= 4.92, $_wR_p$= 6.69, R_{Fobs}= 2.74, R_{Fwobs}= 4.13 (%). It is assumed that La and Sr atoms completely occupy their respective La/Sr sites and Mn atoms are completely located at their 4*e* site. It is difficult to find a very few vacancies for light O atoms by X-ray diffraction method; we assumed that they are fully occupied their atomic sites.

Atom	*x*	*y*	*z*	*B* (Å^2)	*m*	Occ.
La1	0	0	½	0.66(5)	2*b*	0.52(1)
Sr1	0	0	½	0.66(5)	2*b*	0.48(1)
La2	0	0	0.31759(9)	0.50(3)	4*e*	0.34(2)
Sr2	0	0	0.31759(9)	0.50(3)	4*e*	0.66(2)
Mn1	0	0	0.0978(2)	0.17(5)	4*e*	1
O1	0	0	0.0938(8)	0.9(2)	8*g*	1
O2	0	0	0.8021(8)	1.5(3)	4*e*	1
O3	0	½	0	3.2(7)	2*a*	1

Table 4-7. Atomic coordinates, occupancies, and atomic displacement parameters obtained by Rietveld refinement of X-ray diffraction data for $La_{1.4}Sr_{1.6}Mn_2O_7$ indexed in the tetragonal *I4/mmm* space group with lattice constants: $a = b = 3.8720(5)$ Å, $c = 20.224(3)$ Å.

Atom	*x*	*y*	*z*	*Occ.*	*Site*	*Sym.*
La1	0	0	0.5	0.518	2b	4/mmm
Sr1	0	0	0.5	0.482	2b	4/mmm
La2	0	0	0.31694	0.441	4e	4mm
Sr2	0	0	0.31694	0.559	4e	4mm
Mn1	0	0	0.09715	1	4e	4mm
O1	0	0	0	1	2a	4/mmm
O2	0	0.5	0.09537	1	8g	2mn
O3	0	0	0.80105	1	4e	4mm

$R_{wp} = 5.23\%$

Table 4-8. Atomic coordinates, occupancies, and atomic displacement parameters obtained by Rietveld refinement of X-ray diffraction data for $La_{1.3}Sr_{1.7}Mn_2O_7$ indexed in the tetragonal *I4/mmm* space group with lattice constants: $a = b = 3.8712(3)$ Å, $c = 20.1730(19)$ Å.

Atom	*x*	*y*	*z*	*Occ.*	*Site*	*Sym.*
La1	0	0	0.5	0.517	2b	4/mmm
Sr1	0	0	0.5	0.483	2b	4/mmm
La2	0	0	0.31661	0.391	4e	4mm
Sr2	0	0	0.31661	0.609	4e	4mm
Mn1	0	0	0.09761	1	4e	4mm
O1	0	0	0	1	2a	4/mmm
O2	0	0.5	0.09576	1	8g	2mn
O3	0	0	0.80278	1	4e	4mm

$R_{wp} = 5.38\%$

Table 4-9. Atomic coordinates, occupancies, and atomic displacement parameters obtained by Rietveld refinement of X-ray diffraction data for $La_{1.3}Sr_{1.7}Mn_2O_7$ indexed in the tetragonal *I4/mmm* space group with lattice constants: *a* = *b* = 3.8736(3) Å, *c* = 20.0951(15) Å.

Atom	*x*	*y*	*z*	*Occ.*	*Site*	*Sym.*
La1	0	0	0.5	0.463	2b	4/mmm
Sr1	0	0	0.5	0.537	2b	4/mmm
La2	0	0	0.31684	0.368	4e	4mm
Sr2	0	0	0.31684	0.632	4e	4mm
Mn1	0	0	0.09762	1	4e	4mm
O1	0	0	0	1	2a	4/mmm
O2	0	0.5	0.09563	1	8g	2mn
O3	0	0	0.80203	1	4e	4mm

R_{wp} = 4.96%

Table 4-10. Atomic coordinates, occupancies, and atomic displacement parameters obtained by Rietveld refinement of X-ray diffraction data for $La_{1.3}Sr_{1.7}Mn_2O_7$ indexed in the tetragonal *I4/mmm* space group with lattice constants: *a* = *b* = 3.8712(3) Å, *c* = 19.999(2) Å.

Atom	*x*	*y*	*z*	*Occ.*	*Site*	*Sym.*
La1	0	0	0.5	0.408	2b	4/mmm
Sr1	0	0	0.5	0.592	2b	4/mmm
La2	0	0	0.31680	0.316	4e	4mm
Sr2	0	0	0.31680	0.684	4e	4mm
Mn1	0	0	0.09782	1	4e	4mm
O1	0	0	0	1	2a	4/mmm
O2	0	0.5	0.09523	1	8g	2mn
O3	0	0	0.80218	1	4e	4mm

R_{wp} = 5.47%

Table 4-11. Mn-O distance and a magnitude of Jahn–Teller distortion (Δ_{JT}) estimated using the atomic positions obtained from Rietveld analysis. Mn-O_{ap} or Mn-O_{eq} are the distance between Mn and O at apical site or the distance between Mn and O at equatorial site. Δ_{JT} is calculated using an equation Δ_{JT} = Mn-O_{ap}/Mn-O_{eq}[1].

	$x = 0.30$	$x = 0.35$	$x = 0.40$	$x = 0.48$
Mn-O_{ap} / Å	1.9976	1.9727	1.9769	1.9688
Mn-O_{eq} / Å	1.9363	1.9360	1.9372	1.9378
Δ_{JT}	1.0390	1.0276	1.0268	1.0208

4.5. References

1. M. Yashima, N. Sirikanda, T. Ishihara, *J. Am. Chem. Soc.* **2010**,132, 2385–2392
2. B. Dunn, H. Kamath, J.-M. Tarascon, *Science,* **2011** 334, 928–935.
3. F. Gschwind, G. Rodriguez-Garcia, D. J. S. Sandbeck, A. Gross, M. Weil, M. Fichtner, N. Hörmann, *J. Fluor. Chem*. **2016**, 182, 76-90.
4. L. Zhang, M. A. Reddy, P. Gao, T. Diemant, R. Jürgen Behm, M. Fichtner, *J. Solid State Electrochem.* **2016**, 21, 1243-1251.
5. M. Anji Reddy, M. Fichtner, *J. Mater. Chem*. **2011,** 21, 17059-17062.
6. D. Zhang, T. Yoshinari, K. Yamamoto, Y. Kitaguchi, A. Ochi, K. Nakanishi, H. Miki, S. Nakanishi, H. Iba, T. Watanabe, T. Uchiyama, Y. Orikasa, K. Amezawa, Y. Uchimoto, *ACS Appl. Energy Mater*. **2021,** 4, 3352-3357.
7. T. Yoshinari, D. Zhang, K. Yamamoto, Y. Kitaguchi, A. Ochi, K. Nakanishi, H. Miki, S. Nakanishi, H. Iba, T. Uchiyama, T. Watanabe, T. Matsunaga, K. Amezawa, Y. Uchimoto, *J. Mater. Chem. A* **2021**, 9, 7018-7024.
8. D. Zhang, K. Yamamoto, A. Ochi, Y. Wang, T. Yoshinari, K. Nakanishi, H. Nakano, H. Miki, S. Nakanishi, H. Iba, T. Uchiyama, T. Watanabe, K. Amezawa, Y. Uchimoto, *J. Mater. Chem.* A, **2021**, 9, 406-412.
9. D. Zhang, H. Nakano, K. Yamamoto, K. Tanaka, T. Yahara, K. Imai, T. Mori, H. Miki, S. Nakanishi, H. Iba, *ACS Appl. Mater. & Interfaces* **2021**, 13, 30198-30204.
10. D. T. Thieu, M. H. Fawey, H. Bhatia, T. Diemant, V. S. K. Chakravadhanula, R. J. Behm, C. Kübel, M. Fichtner, *Adv. Funct. Mater.* **2017***,* 27, 1701051.
11. M. A. Nowroozi, K. Wissel, J. Rohrer, A. R. Munnangi, O. Clemens, *Chem. Mater.*, **2017**, 29, 3441-3453.
12. M. A. Nowroozi, S. Ivlev, J. Rohrer, O. Clemens, *J. Mater. Chem. A* **2018**, 6, 4658-4669.
13. Y. Wang, K. Yamamoto, Y. Tsujimoto, T. Matsunaga, D. Zhang, Z. Cao, K. Nakanishi, T. Uchiyama, T. Watanabe, T. Takami, H. Miki, H. Iba, K. Maeda, H. Kageyama, Y. Uchimoto, *Chem. Mater.* **2022**, 34, 609-616.
14. Y. Wang, T. Takami, Z. Li, K. Yamamoto, T. Matsunaga, T. Uchiyama, T. Watanabe, H. Miki, T. Inoue, H. Iba, U. Mizutani, H. Sato, K. Maeda, H. Kageyama, Y. Uchimoto, *Chem. Mater.* **2022**, 34, 10631–10638.
15. K. Wissel, R. Schoch, T. Vogel, M. Donzelli, G. Matveeva, U. Kolb, M. Bauer, P. R. Slater, O. Clemens, *Chem. Mater.* **2021**, 33*,* 499-512.
16. M. A. Nowroozi, K. Wissel, M. Donzelli, N. Hosseinpourkahvaz, S. Plana-Ruiz, U. Kolb, R. Schoch, M. Bauer, A. M. Malik, J. Rohrer, S. Ivlev, F. Kraus, O. Clemens,

Commun. Mater. **2020**, 1, 27.

17. S. Vasala, A. Jakob, K. Wissel, A. I. Waidha, L. Alff, O. Clemens, *Adv. Electron. Mater*. **2020**, 6, 1900974.
18. H. Miki, K. Yamamoto, H. Nakaki, T. Yoshinari, K. Nakanishi, S. Nakanishi, H. Iba, J. Miyawaki, Y. Harada, A. Kuwabara, Y. Wang, T. Watanabe, T. Matsunaga, K. Maeda, H. Kageyama, Y. Uchimoto, *J. Am. Chem. Soc.* accepted.
19. S. Xu, R. Jacobs, D. Morgan, *Chem. Mater*. **2018**, 30, 7166-7177.
20. T. Sivakumar, J. B. Wiley. *Mater. Res. Bull*. **2009**, 44, 74–77.
21. K. Rucka, M. Sgrajaa, G. Krabbesa, K. Do¨rra, K.-H. Mu¨llera, M. Khristovb, J. Alloys Compd. **2000**, 306, 151–157.
22. T. Sivakumar, J. B. Wiley, *Materials Research Bulletin*, **2009**, 44, 1, 74-77
23. C. Rongeat, M. A. Reddy, R. Witter, M. Fichtner. *ACS Appl. Mater. Interfaces* **2014**, 6, 2103–2110.
24. S. Torii, M. Yonemura, T.Y.S.P. Putra, J. Zhang, P. Miao, R. P. Muroya, T. Muroya, R. Tomiyasu, T. Morishima, S. Sato, *J. Phys. Soc. Jpn*. **2011**, 80, B020.
25. T. Hattori, Y. Katayama, A. Machida, T. Otomo, K. Suzuya, *J. Phys.: Conf. Ser.* **2010**, 215, 012024 1–4.
26. V. Petricek, M. Dusek, L. Palatinus, *Z. Kristallogr*. **2014**, .229, 345–352.
27. K. Momma, T. Ikeda, A. A. Belik, F. Izumi, *Powder Diffraction* **2013**. 28, 184–193.
28. K. Momma, F. Izumi, *J. Appl. Crystallogr*. **2012**, 44, 1272–1276.
29. P. E. Blöchl, *Phys. Rev. B* **1994**, 50, 17953–17979.
30. D. G. Kresse, D. Joubert, *Phys. Rev. B* **1999**, 59, 1758–1775.
31. G. Kresse, J. Hafner, *Phys. Rev. B* **1993**, 47, 558–561.
32. G. Kresse, J. Furthmüller, *Comp. Mater. Sci*. **1996**, 6, 15–50.
33. G. Kresse, J. Furthmüller, *Phys. Rev. B* **1996**, 54, 11169–11186.
34. J. P. Perdew, A. Ruzsinszky, G. I. Csonka, O. A. Vyron, G. E. Scuseria, L.A. Constantin, X. Zhou, K. Burke, *Phys. Rev. Lett*. **2008**, 100, 136406 1–5.
35. S. L. Dudarev, G. A. Botton, S. Y. Savrasov, C. J. Humphreys, A. P. Sutton, *Phys. Rev. B* **1998**, 57, 1505–1509.
36. M. Ležaić, N. A. Spaldin, *Phys. Rev. B* **2011**, 83, 024410 1–6.
37. H. J. Monkhorst, J. D. Pack, *Phys. Rev. B* **1976**, 13, 5188–5192.
38. A. Seko, Y. Koyama, I. Tanaka, *Phys. Rev. B* **2009**, 80, 165122 1–7.
39. G. Mills, H. Jonsson, G. K. Schenter, *Surf. Sci.* **1995**, 324, 305–337.
40. T. Kimura, Y. Tomioka, A. Asamitsu, Y. Tokura, *Phys. Rev. Lett*. **1998**, 81, 5920.
41. M. Kubota, H. Fujioka, K. Hirota, K. Ohoyama, Y. Moritomo, H. Yoshizawa, Y. Endoii, *J. Phys. Soc. Jpn*. **2000**, 69, 1606-1609.

42. A. R. Armstrong, M. Holzapfel, P. Novak, C. S. Johnson, S.-H. Kang, M. M. Thackeray, and P. G. Bruce, *J. Am. Chem. Soc.* **2006**, 128, 8694-8698.
43. M. Oishi, K. Yamanaka, I. Watanabe, K. Shimoda, T. Matsunaga, H. Arai, Y. Ukyo, Y. Uchimoto, Z. Ogumia and T. Ohta, *J. Mater. Chem. A,* **2016**, 4, 9293–9302.
44. M. Jiang, B. Key, Y. S. Meng, and C. P. Grey, *Chem. Mater.* **2009**, 21, 2733–2745.
45. N. Yabuuchi, K. Yoshii, S.-T. Myung, I. Nakai, and S. Komaba, *J. Am. Chem. Soc.***2011**, 133, 4404–4419.
46. T. Sivakumar, J.B. Wiley, *Mater. Res. Bull.* **2009**, 44, 74–77.

Chapter 5.
Effect on Anionic Redox of Transition Metal Species in Ruddlesden-Popper type Perovskites

Abstract

So far, we have focused on $La_{1.2}Sr_{1.8}Mn_2O_7$ with a Ruddlesden-Popper layered perovskite structure and demonstrated its ability for electrochemical insertion and extraction of fluoride ions. Furthermore, we have proposed that by utilizing not only transition metals but also oxide ion redox reactions, it could be a promising cathode material for high-energy density fluoride ion batteries. In this chapter, our objective was to deepen our understanding of the conditions under which anion redox occurs by varying the transition metal species present in the structure. We examined the charge-discharge characteristics and mechanisms when using $Sr_3Ru_2O_7$ and $La_2SrFe_2O_7$ as cathodes. Both materials showed the ability for fluoride ion insertion and extraction, confirming their potential as materials exhibiting intercalation reactions. Interestingly, we found that $La_2SrFe_2O_7$ exhibited a high capacity corresponding to approximately 2.5 electron reactions by utilizing oxygen redox reactions. This ability to reversibly utilize anion redox in Fe-based oxides differs from the mechanism of anion redox in lithium-excess cathode materials[1]. It may be related to the peculiarities of Fe-based perovskite oxides, such as the abnormal valence of Fe^{4+} and the lack of changes in the cation coordination environment around oxygen in the case of fluoride ion batteries.

5.1. Introduction

Against the background of remarkable industrial development in recent years and the liberalization of mobility of people and goods, research and development of various innovative batteries are being studied aiming at higher performance storage battery systems.

Among them, fluoride ion batteries (FIBs), which can utilize a multivalent reaction while using a monovalent anion as a carrier, is expected as an innovative battery to have a high energy density[2]. However, it includes issues such as low fluoride ion diffusivity in the active material and cycle degradation associated with dramatic volume changes during charge/discharge since the electrode materials for FIBs ever reported utilize the conversion type charge/discharge reaction of metals/metal fluorides[3].

In order to solve these problems, we have studied the development of novel intercalation type electrode materials. In previous chapters, we have found that Ruddlesden-Popper type layered perovskite $La_{1.2}Sr_{1.8}Mn_2O_7$ allows electrochemical insertion and removal of fluoride ions in the crystal structure. Furthermore, it has been found that a high capacity can be developed by utilizing anionic redox of oxide ions. This material can improve the cycle stability and rate performance of FIBs, although this material is inferior in capacity to the conversion type positive electrode material.

However, there remains still large room for improvement in material properties for practical application, and we think the next study is to analyze the mechanism of high-capacity expression in detail and search for materials that can express higher capacity. For example, it is important to know the origin of stable anion redox, which has been reported to be explained by the band structure of transition metals and oxygen in Li-excess cathode materials in LIB[4].

The purpose of this study is to clarify the origin of the anion redox in the FIBs. Specifically, we focused on $Sr_3Ru_2O_7$ and $La_2SrFe_2O_7$, which are composed of different transition metal species with $La_{1.2}Sr_{1.8}Mn_2O_7$, and evaluated their electrode characteristics using an all-solid-state battery. Especially for $La_2SrFe_2O_7$, we attempt to analyze the charge compensation mechanism using *ex-situ* XAFS. Although we assumed the same mechanism as Li-rich cathodes in LIBs[1,4], contrary to expectations, we obtained the possibility of using different type of anion redox, such as reversible use of superoxide ions.

5.2. Experimental

5.2.1. Synthesis of Materials

$Sr_3Ru_2O_7$ and $La_2SrFe_2O_7$ were prepared by solid-state synthesis, referring to the previous reports[5-8]. In the case of $Sr_3Ru_2O_7$, $SrCO_3$ (99.9%, WAKO pure chemical industries, ltd.) and RuO_2 (99.9%, Strem Chemicals, Inc.) were mixed using a planetary ball mill for 10 hours. The mixing ratio was adjusted to a molar ratio of 3:2. The mixture was pelletized and then annealed at 1300 °C for 20 hours. After grinding, the mixture was pelletized again and subjected to the same annealing conditions to obtain the sample. $La_2SrFe_2O_7$ was synthesized using La_2O_3 (99.99%, Kojundo Chemical Laboratory), $SrCO_3$ (99.9%, WAKO pure chemical industries, ltd.), and Fe_2O_3 (99.9%, WAKO pure chemical industries, ltd.) as starting materials. The synthesis procedure and conditions were the same as for $Sr_3Ru_2O_7$. To use $La_{0.9}Ba_{0.1}F_{2.9}$, which exhibits relatively high fluoride-ion conductivity, as a solid electrolyte, it was synthesized following a method reported in the literature[9]. LaF_3 (99.9%, Kojundo Chemical Laboratory) and BaF_2 (99.9%, Kojundo Chemical Laboratory) were weighed and mixed by ball-milling for 12 hours at 600 rpm. To prevent exposure to air, 45 ml ZrO_2 ball mill pots were filled with Ar. Subsequently, we obtained crystalline $La_{0.9}Ba_{0.1}F_{2.9}$ by annealing at 600°C for 10 hours.

5.2.2. Assembly of the Electrochemical Cell and Measurement

All-solid-state fluoride ion batteries were fabricated for evaluation of cathode active material. All processes were carried out in Ar filled glovebox. The cathode layer was composed of active material ($Sr_3Ru_2O_7$ or $La_2SrFe_2O_7$), solid electrolyte $La_{0.9}Ba_{0.1}F_{2.9}$, and electron-conductive agent Vapor-Grown Carbon Fiber in a weight ratio of 30:60:10, which were ball-milled together as powders (mixing conditions were set at 100 rpm to prevent undesired reactions). The anode layer consisted of PbF_2/acetylene black (Denki Kagaku Kogyo, AB) composite mixed for 3 hours at 600 rpm in a ball mill. $La_{0.9}Ba_{0.1}F_{2.9}$, a fluoride ion conductor, was used as the separator. The electrochemical cells were formed by compressing 10 mg of cathode powder and 50 mg of anode layer onto both sides of the solid electrolyte pellet at 4 ton/cm^2. Pb foil with 0.2 mm thick was stacked as the anode current collector, while Pt foils were stacked as the cathode current collectors. The cells were evaluated at 140°C in a potential range of -1.5 to 3.0 V vs. Pb/PbF_2. Various electrochemical properties were evaluated using a potentiostat/galvanostat apparatus (VMP3, Bio-Logic Science Instruments).

5.2.3. Materials Characterization

X-ray diffraction (XRD) measurements were carried out using Rigaku Ultima IV with Cu Kα radiation at 40 kV, 40 mA. Synchrotron X-ray diffraction (SXRD) profiles collected at BL02B2 beamline in SPring-8. X-ray absorption spectroscopy (XAS) was recorded at BL01B1and BL14B2 beamline in SPring-8. Corrector-spherical aberration scanning transmission electron-microscope (Cs-STEM) observation was performed to analyze the crystal structure of active materials after charge-discharge evaluation by JEM-ARM200F (JEOL). The samples were prepared by thinning using cryo-focused ion beam (cryo-FIB) micro-sampling technique in nanoDUE'T NB5000 (HITACHI) to allow electron beam transmission during STEM observation. To identify the atomic-level arrangement of elements and the position of intercalated fluoride ions in the crystal material, atomic-resolution electron energy loss spectroscopy (EELS) mapping measurements were conducted.

5.3. Results and Discussion

5.3.1. Fluoride Ion Intercalation into $Sr_3Ru_2O_7$

The crystal structures of the prepared $Sr_3Ru_2O_7$ were examined by XRD measurements. The obtained XRD patterns are shown in **Fig. 5-1**. No detectable peaks attributed to impurities are observed in the samples, and the patterns were indexed to the tetragonal *I*4/*mmm* space group.

The electrochemical performance of the synthesized $Sr_3Ru_2O_7$ was examined by galvanostatic measurements. The cathode mixture is constituted without a chemical reaction between the active material $Sr_3Ru_2O_7$, solid electrolyte $La_{0.9}Ba_{0.1}F_{2.9}$ and electron conductor VGCF. **Fig. 5-2** shows the charge/discharge curves of the $Sr_3Ru_2O_7$ cathodes evaluated under the conditions of 10 mA/g at 140°C, in the voltage range of -1.5V to 3.0V. The discharge capacity was approximately 200mAh/g, and the corresponding number of electron reactions was determined to be four. This indicates a similar number of electron reactions as the $La_{1.2}Sr_{1.8}Mn_2O_7$ cathode utilizing anion redox reactions, suggesting that $Sr_3Ru_2O_7$ also exhibits a high capacity by utilizing oxygen-derived redox reactions. The cause of the high capacity may be interpreted by comparing with the phenomenon of anion redox in LIB[4]. In Ru-based Li-excess cathodes, it is reported that a high capacity can be delivered by the charge compensation of the generation of ligand holes in the hybridized orbitals of Ru 4d and O 2p[3]. Similarly, in $Sr_3Ru_2O_7$, in the high potential region, high capacity could be obtained basically by generating ligand holes in Ru 4d and O 2p.

Fig. 5-3 shows the results of ex-situ XRD patterns after charge/discharge. During the charging process, the peaks corresponding to $Sr_3Ru_2O_7$ disappeared, and new peaks attributed to the oxyfluoride compound $Sr_3Ru_2O_7F_2$ were observed in samples charged above 2.0V. This observation is consistent with the results of Cs-STEM analysis shown in **Fig. 5-4**. The atomic-resolution STEM-EELS mapping in **Fig. 5-4b** revealed a strong fluorine signal in the interstitial layers, indicating the progress of intercalation reactions similar to $La_{1.2}Sr_{1.8}Mn_2O_7$. For samples charged up to 3.0V, no significant changes were observed in the XRD spectra compared to 2.0V. This trend is similar to $La_{1.2}Sr_{1.8}Mn_2O_7$. On the other hand, during discharge, both peaks attributed to $Sr_3Ru_2O_7$ and $Sr_3Ru_2O_7F_2$ disappeared after discharging to -1.5V. In addition, it has been confirmed that the shape of the discharge curve changes little by little as the cycle progresses, particularly in the high potential region. The disappearance of crystalline peaks in the XRD spectrum suggests the possibility of amorphization occurring during the discharge process, which may be related to the changes in the shape of the discharge curve[11]. This is a different behavior compared to $La_{1.2}Sr_{1.8}Mn_2O_7$, and further detailed analysis is planned for the future.

5.3.2. Fluoride Ion Intercalation into $La_2SrFe_2O_7$

Fig. 5-5a shows the XRD pattern of synthesized $La_2SrFe_2O_7$. The pattern is good agreement with the reported structure. No impurity peaks were also observed in the pattern. **Fig. 5-5b** shows SEM images of $La_2SrFe_2O_7$, which composed approximately 10 μm of particle size. In addition, the shape of the facet surface is confirmed from the particle surface, indicating that the crystallinity is high.

Fig. 5-6 shows the charge/discharge curves of the $La_2SrFe_2O_7$ cathode at 10 mA/g under 140°C. The initial charge curve is characteristic, a plateau is confirmed around 1.6 V vs. Pb/PbF_2, and a capacity equivalent to 3 electrons was delivered. $La_2SrFe_2O_7$ includes Fe^{3+}, and considering that there are few examples where Fe^{4+} exists stably, the activation of the electrode due to oxygen release, which leads to reversible charge/discharge of the subsequent cycle, should be occurring. Except for the characteristic charge curve of the first time, it was confirmed that a reversible charge/discharge curve was drawn after that, and its charge/discharge capacity was about 120mAh/g equivalent to 2.5 electron reaction, and charge/discharge efficiency can be confirmed to be close to 100%. Furthermore, the charge/discharge capacity increases slightly with each cycle, which behaves differently from the Fe-based Li-excess cathodes in LIB.

Fig. 5-7 shows the results of XRD measurement of synchrotron radiation to investigate structural changes during charge and discharge. Almost no change was observed in the XRD peak during charge/discharge. That is, although a reversible charge/discharge capacity was confirmed, a result indicating insertion of fluoride ions into the rock salt layer was not obtained. This is similar to the process of excessively incorporating fluoride ions into the structure of the high potential region of $La_{1.2}Sr_{1.8}Mn_2O_7$, and $La_2SrFe_2O_7$ is thought to cause insertion and desorption of fluoride ions utilizing the perovskite layer.

The charge compensation during insertion/extraction of fluoride ions into the structure was examined by XAFS measurement. The measurement result of Fe *L*-edge is shown in **Fig. 5-8a**. It was confirmed that the peak derived from Fe^{3+} was slightly weakened by charging, and the result suggesting the formation of Fe^{4+} during charging was obtained. Also, surprising results were obtained from O *K*-edge shown in **Fig. 5-8b**. It is confirmed that the unstable $(O_2)^-$ superoxide ions that appear temporarily during the charging process increase in strength with the progress of charging in the LIB Fe-based Li-excess cathode[1]. That is, superoxide ions are stabilized during the charging process. Further surprisingly, it is confirmed that the $(O_2)^-$ ions disappear reversibly during the discharge process. Such behavior is a behavior that has not been confirmed by LIB, and should be a phenomenon unique to fluoride ion batteries.

The reason why this phenomenon occurred was examined. In the following, we consider that superoxide ions could contribute to the redox reaction stably in this material system from two viewpoints. The first is the possibility that this phenomenon is unique to Sr-Fe-O perovskite materials. Research in other fields says that Sr-Fe-O-based perovskites are actually stabilized by generating holes in the bond orbitals with oxygen, but there is an unusual valence of Fe^{4+}. In this case, it is considered that an abnormal valence such as Fe^{4+} was generated during the oxidation process by insertion of fluoride ions. Second, the oxygen coordination environment is different from the Li system. In the case of a Li-ion battery, Li is desorbed with charging, that is, cations around oxygen decrease, and it is thought that oxidized oxide ions are likely to become unstable. On the other hand, in the case of a fluoride ion battery, fluoride ions, which are another anion species, can enter the structure and have some influence on the binding, but there is no release of cationic species out of the structure. It is thought that the product ions are isolated from other oxide ions and stabilized in an isolated state. From the above, it is considered that the $La_2SrFe_2O_7$ positive electrode for fluoride ion batteries behaved differently from the Li-rich positive electrode.

Fig. 5-9 shows the measurement result of F *K*-edge. It was confirmed that the peak near 685 eV increased with charging, and conversely the intensity decreased during the discharging process. In past research reports[12], there is a report that the peak at this position is derived from the bond with the transition metal in the perovskite, suggesting that F was inserted into the perovskite during the charging process.

5.4. Conclusion

In order to obtain knowledge about the condition of oxide anion redox, we examined the charge/discharge behavior of $Sr_3Ru_2O_7$ and $La_2SrFe_2O_7$ with different transition metal species. In all cases, charging to a high potential resulted in a suggestion of reversible progress of the charge/discharge reaction via redox of oxide ions. However, these results were found to be slightly different in character from the anion redox in LIBs. Most surprisingly, in $La_2SrFe_2O_7$, the reversible redox reaction of superoxide ions would contribute to the charge/discharge reaction. This is suggested by the results of XAFS measurements, it was confirmed that the peak accompanying the generation of superoxide ions increased with charging, and the peak gradually disappeared with discharge. This is because, in the perovskite structure, the unusual valence exists, and unlike Li-containing transition metal compounds, the coordination environment of cations around oxygen does not change during charge/discharge (cation vacancy cannot be generated). It may contribute to stabilizing the redox reaction of superoxide ions.

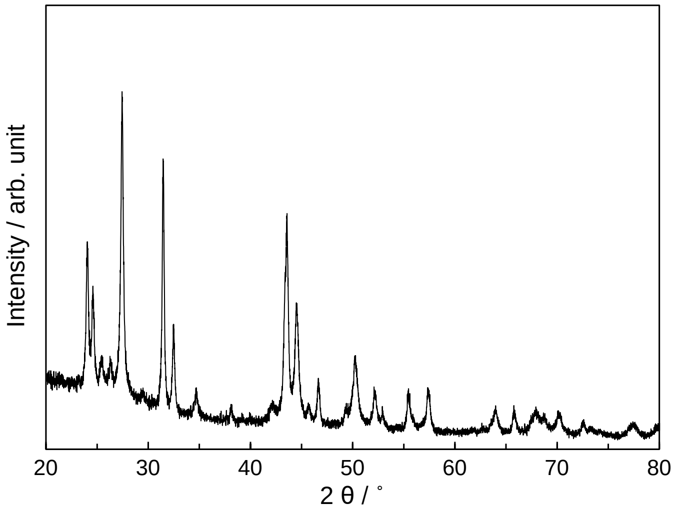

Fig. 5-1. XRD pattern of synthesized $Sr_3Ru_2O_7$.

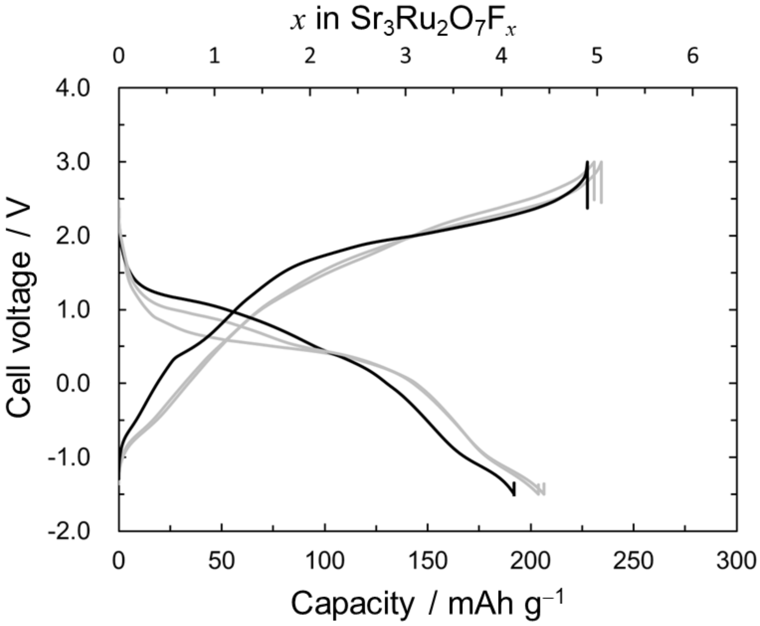

Fig. 5-2. Charge/discharge curves of $Sr_3Ru_2O_7$. Black lines, gray lines show 1st cycle, 2nd and 3rd cycles, respectively.

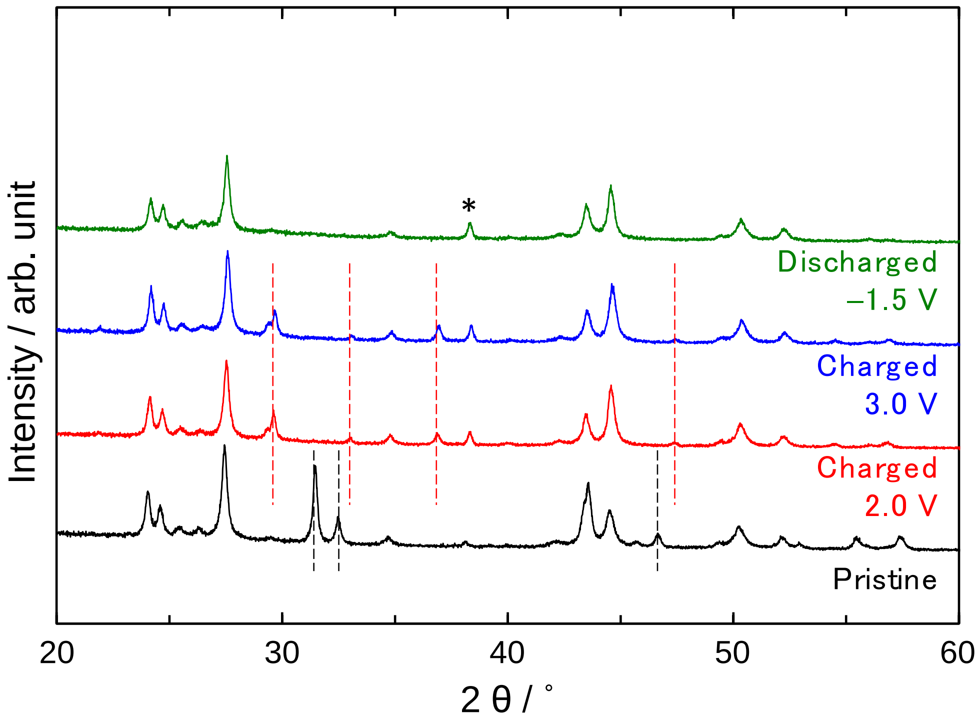

Fig. 5-3. XRD patterns of $Sr_3Ru_2O_7$ cathode before and after charge/discharge. Asterisk shows a peak derived from a measurement jig.

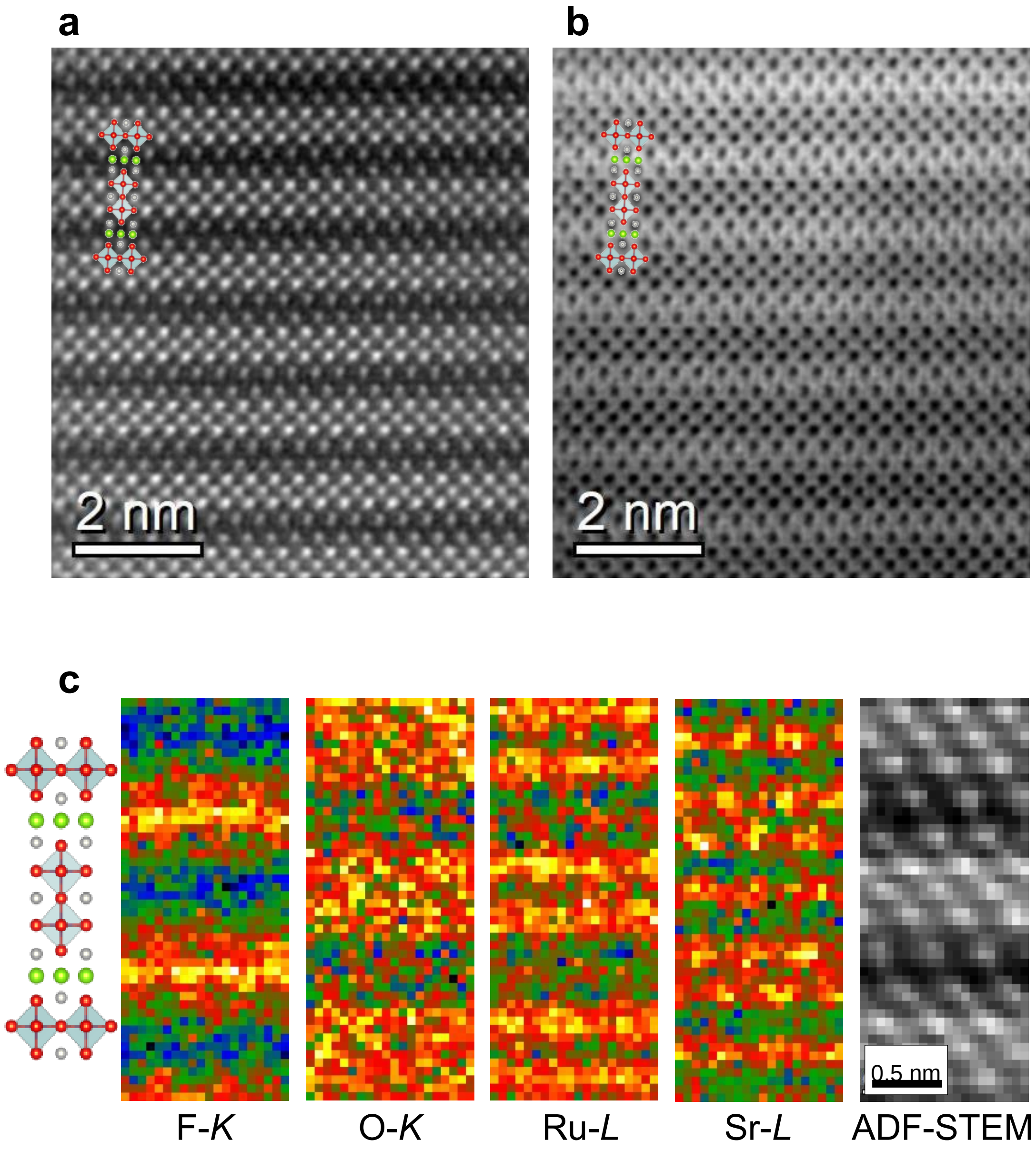

Fig. 5-4. Spherical Aberration (Cs) corrected Scanning Transmission Electron Microscope (Cs-STEM) observations of $Sr_3Ru_2O_7$ cathode after charged at 1.4 V vs. Pb/PbF_2 viewed along [010]. **a**, High-angle annular dark-field (HAADF) and **b**, annular bright-field (ABF) STEM images **c**, Atomic resolution STEM-EELS mapping images. For simplicity, the ideal structures are shown[10].

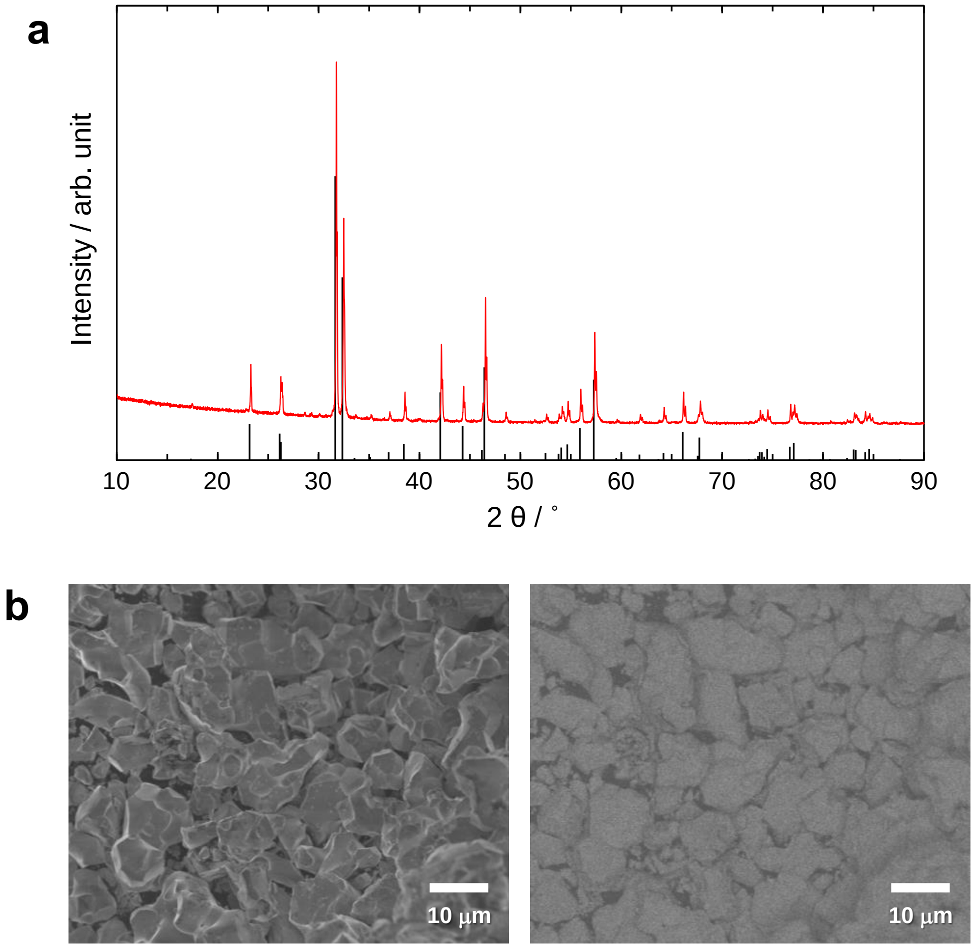

Fig. 5-5. a, XRD pattern of prepared $La_2SrFe_2O_7$ (Reference ICSD #85943). **b,** SEM images of $La_2SrFe_2O_7$ (Left; secondary electron image. Right; Backscattered electron image.).

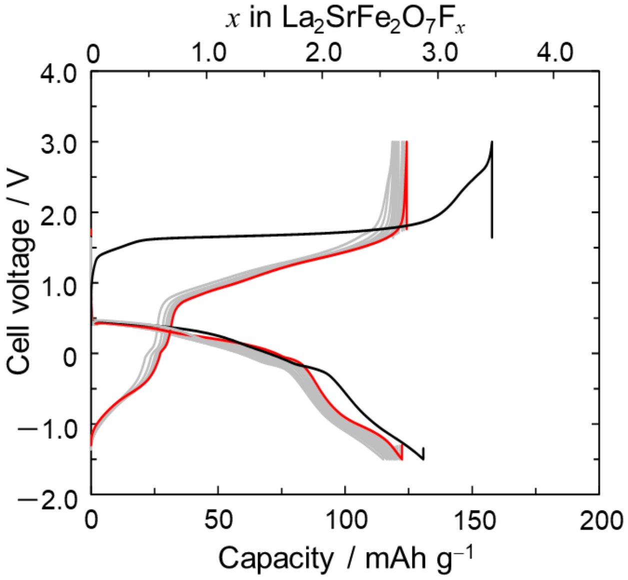

Fig. 5-6. Charge/discharge curves of $La_2SrFe_2O_7$ cathode. Black lines, gray lines and red lines show 1st cycle, 2nd – 9th cycles and 10th cycle, respectively.

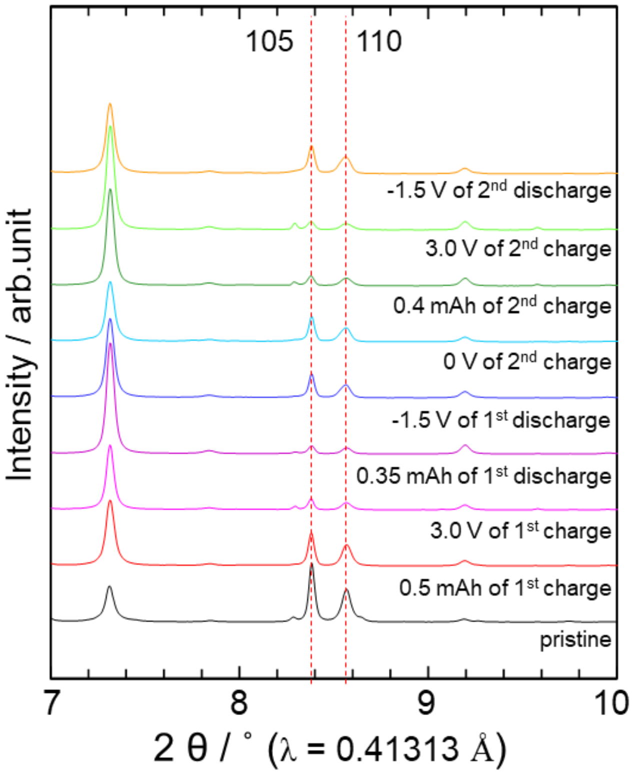

Fig. 5-7. Synchrotron XRD patterns of $La_2SrFe_2O_7$ cathode during charge/discharge.

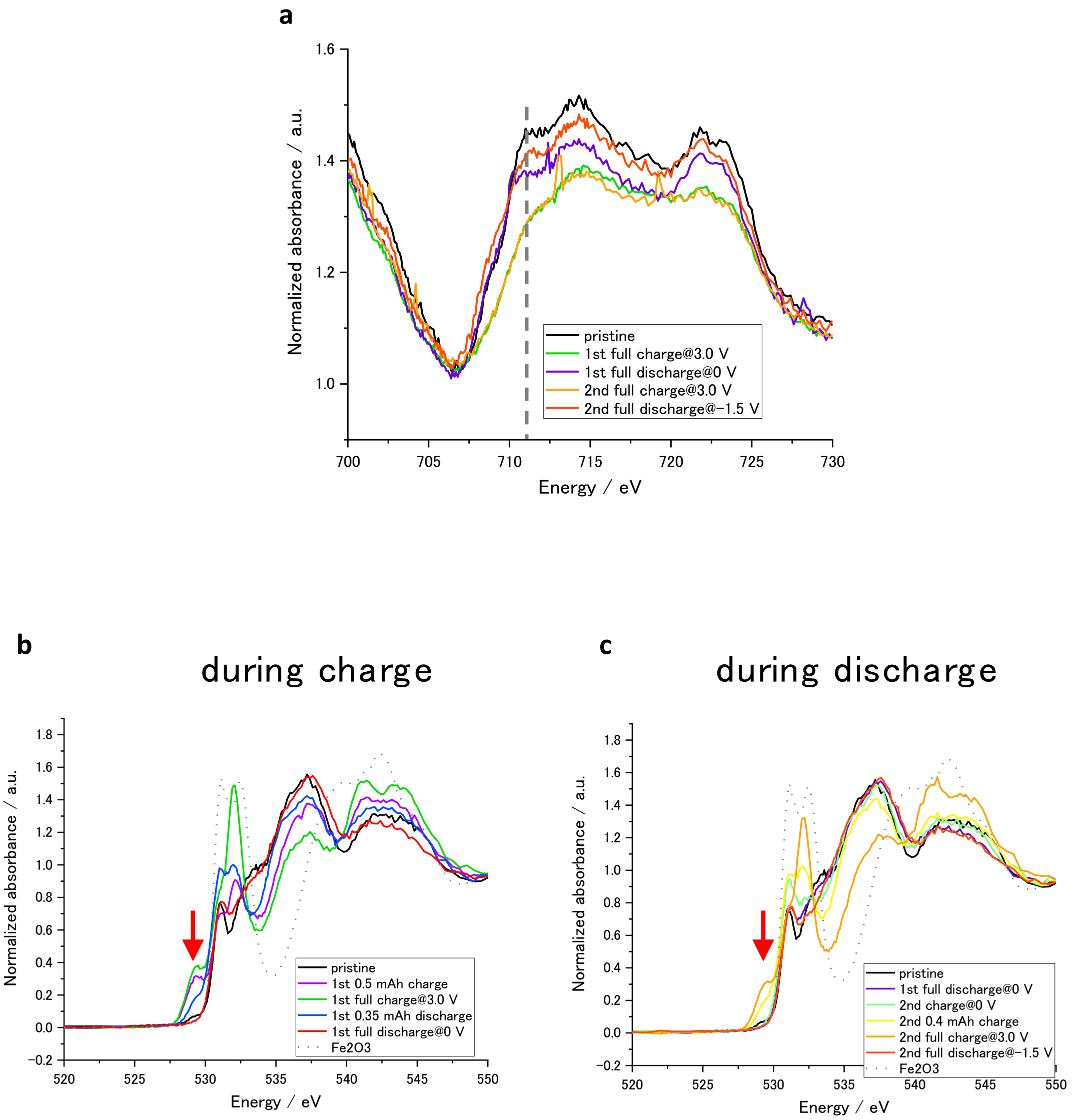

Fig. 5-8. XANES spectra of $La_2SrFe_2O_7$ cathode during charge/discharge. **a,** Fe *L*-edge spectra. **b,** O *K*-edge spectra during charge process. **c,** O *K*-edge spectra during discharge process.

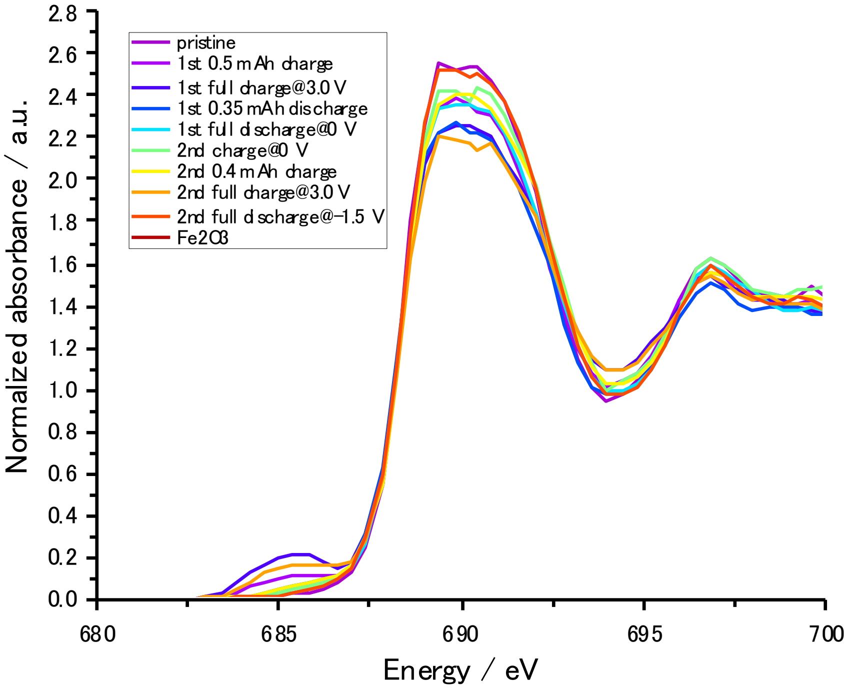

Fig. 5-9. XANES spectra of F K-edge in $La_2SrFe_2O_7$ cathode during charge/discharge.

5.5. References

1. N. Yabuuchi, M. Nakayama, M. Takeuchi, S. Komaba, Y. Hashimoto, T. Mukai, H. Shiiba, K. Sato, Y. Kobayashi, A. Nakao, M. Yonemura, K. Yamanaka, K. Mitsuhara, T. Ohta, Origin of stabilization and destabilization in solid-state redox reaction of oxide ions for lithium-ion batteries, *Nature Commun*, **2016**, 7, 13814.

2. F. Gschwind, G. Rodriguez-Garcia, D.J.S. Sandbeck, A. Gross, M. Weil, M. Fichtner, N. Hormann, Fluoride ion batteries: Theoretical performance, safety, toxicity, and a combinatorial screening of new electrodes, *J. Fluorine Chem*. **2016**, 182, 76-90

3. M. Anji Reddy and M. Fichtner, Batteries based on fluoride shuttle, *J. Mater. Chem.*, **2011**, 21, 17059

4. K. Yamamoto, Y. Zhou, N. Yabuuchi, K. Nakanishi, T. Yoshinari, T. Kobayashi, Y. Kobayashi, R. Yamamoto, A. Watanabe, Y. Orikasa, K. Tsuruta, J. Park, H. R. Byon, Y. Tamenori, T. Ohta, Y. Uchimoto, Charge Compensation Mechanism of Lithium-Excess Metal Oxides with Different Covalent and Ionic Characters Revealed by Operando Soft and Hard X-ray Absorption Spectroscopy, *Chem. Mater.*, **2020**, 32, 139-147

5. A. Banerjee, R Prasad, V. Venugopal, Thermodynamic properties of Sr_2RuO_4(s) and $Sr_3Ru_2O_7$(s) by using solid-state electrochemical cells, *J. Alloys and Compounds*, **2004**, 373, 1-2, 59-66

6. Shaked, H., Jorgensen, J. D., Chmaissem, O., Ikeda, S. & Maeno, Y. Neutron diffraction study of the structural distortions in $Sr_3Ru_2O_7$. *J. Solid State Chem.* **154**, 361–367 (2000).

7. E. A. Tugova, V. F. Popova, I. A. Zvereva & V. V. Gusarov, Mechanism and kinetics of formation of $La_2SrFe_2O_7$ and $Nb_2SrFe_2O_7$, *Russian J. General Chem.*,

2007, 77, 979-981

8. Sharma, I. B. & Singh, D. Preparation and study of structural electrical and magnetic properties of $La_2SrFe_2O_7$ and $La_2SrMn_2O_7$. *Proc. Indian Acad. Sci. - Chem. Sci.* **107**, 189–196 (1995).

9. C. Rongeat, M. A. Reddy, R. Witter, M. Fichtner, Solid Electrolytes for Fluoride Ion Batteries: Ion Conductivity in Polycrystalline Tysonite-Type Fluorides, *ACS Appl. Mater. Interfaces,* **2014**, 6, 3, 2103–2110

10. K. Momma, F. Izumi. *VESTA 3* for three-dimensional visualization of crystal, volumetric and morphology data. *J. Appl. Crystallogr.*, **2011**, 44, 1272–1276.

11. Sathiya, M. *et al.* Origin of voltage decay in high-capacity layered oxide electrodes. *Nat. Mater.* **14**, 230–238 (2015).

12. J. Wang, Y. Shin, E. Arenholz, B. M. Lefler, J. M. Rondinelli, and S. J. May, Effect of fluoropolymer composition on topochemical synthesis of $SrMnO_{3-\delta}F_{\gamma}$ oxyfluoride films, *Phys. Rev. Materials*, **2018** 2, 073407

Chapter 6.
General Conclusion

For the realization of a society that provides free mobility of people and things such as CASE (Abbreviation for "Connected", "Autonomous driving", "Shared & Services", and "Electric vehicles") and MaaS (Abbreviation for "Mobility as a Service"), research and development of high-performance energy devices is required. Fluoride ion batteries with energy density exceeding that of Li-ion batteries are considered as one candidate for high energy density batteries. However, since the conventional fluoride ion battery employs a conversion-type reaction mechanism, there are significant problems in fluoride ion diffusivity and cycle characteristics. In this thesis, for the purpose of these fundamental solutions, we focused on the search for intercalation materials that were rarely reported before and proposed a novel cathode material with Ruddlesden-Popper type layered perovskite structure.

In Chapter 1, an overview of fluoride ion batteries was explained. In particular, the challenges with fluoride ion batteries have been organized, focusing on the electrode materials ever reported. Based on that, we provided a detailed explanation of the research guidelines we developed for intercalation materials.

In Chapter 2, we focused on $La_{1.2}Sr_{1.8}Mn_2O_7$ and $La_{1.2}Sr_{1.8}Mn_2O_7F_2$, which have Ruddlesden-Popper type layered perovskite structures, to validate the concept of intercalation cathodes. We confirmed that fluoride ions can be electrochemically intercalated and deintercalated utilizing the anion sites in the rock salt layers, demonstrating the potential of intercalation reactions in fluoride ion batteries.

Surprisingly, we discovered for the first time that up to four fluoride ions can be reversibly intercalated and deintercalated within the structure. XAFS measurements and STEM observations revealed that this reaction is not solely dependent on the transition metal Mn but also significantly influenced by the redox reaction of oxide ions. Additionally, RIXS measurements suggested the formation of O-O bonds within the crystal structure during the anion redox of oxide ions. These reactions exhibit relatively good cycling and rate characteristics, indicating the potential of anion redox-based intercalation cathodes as candidates for fluoride battery cathodes.

In Chapter 3, we conducted a detailed analysis of the insertion and extraction reactions of fluoride ions into the rock salt layer of $La_{1.2}Sr_{1.8}Mn_2O_7F_x$ ($0 \leq x \leq 2$). It was revealed that an intermediate phase, $La_{1.2}Sr_{1.8}Mn_2O_7F$, is formed during the charge and discharge reactions, indicating a two-step, two-phase coexistence reaction. The presence of this two-step reaction helps alleviate the significant volume change from $La_{1.2}Sr_{1.8}Mn_2O_7$ to $La_{1.2}Sr_{1.8}Mn_2O_7F_2$, contributing to favorable rate characteristics.

In Chapter 4, we conducted a study focusing on ion diffusion in the crystal structure to further improve the rate performance of intercalation cathodes. Estimation of ion diffusion pathways in the crystal structure was carried out through precise neutron diffraction and synchrotron XRD analysis. We confirmed that, contrary to conventional anion conduction, hopping conduction along the <110> direction utilizing only the interstitial sites in the rock salt layer is predominant. To enhance ion diffusion pathways, samples with varying La/Sr ratios in $La_{2-2x}Sr_{1+2x}Mn_2O_7$ were prepared, and their effects on rate performance were investigated. It was revealed that increasing the interlayer distance improves the rate performance, providing guidelines for material design aimed at enhancing rate performance.

In Chapter 5, we have described the results of evaluating the characteristics of positive electrodes for $Sr_3Ru_2O_7$ and $La_2SrFe_2O_7$ composed of different transition metals. In $La_2SrFe_2O_7$, different results from Fe-based Li-rich materials, which are said to be unable to utilize anion redox stably, were obtained, and the *ex-situ* XAFS results suggested that superoxide ions contributed to charge compensation reversibly in charge/discharge reactions.

In Chapter 6, this chapter summarizes this paper.

This study proposed that intercalation cathodes can be potential candidates for high-energy density fluoride ion batteries, and it elucidates their charge/discharge mechanism and ion diffusion mechanism. By using these results, we hope to contribute to further material exploration in the field.

List of Publications

■Chapter 2

Hidenori Miki, Kentaro Yamamoto, Hiroyuki Nakaki, Takahiro Yoshinari, Koji Nakanishi, Shinji Nakanishi, Hideki Iba, Jun Miyawaki, Yoshihisa Harada, Akihide Kuwabara, Yanchang Wang, Toshiki Watanabe, Toshiyuki Matsunaga, Kazuhiko Maeda, Hiroshi Kageyama, Yoshiharu Uchimoto
"Double-Layered Perovskite Oxyfluoride Cathodes with High Capacity Involving O–O Bond Formation for Fluoride-Ion Batteries."
Journal of American Chemical Society, Published online.
https://doi.org/10.1021/jacs.3c10871

■Chapter 3

Hidenori Miki, Kentaro Yamamoto, Toshiyuki Matsunaga, Toshiki Watanabe, Mukesh Kumar, Neha Thakur, Hideki Iba, Hiroshi Kageyama, Yoshiharu Uchimoto
"Transient phase change of Ruddlesden-Popper type perovskite on fluoride-ion intercalation reaction."
Solid State Ionics, **2024**, 406, 116481.
https://doi.org/10.1016/j.ssi.2024.116481

■Chapter 4

Hidneori Miki, Toshiyuki Matsunaga, Zhuoran Li, Kentaro Yamamoto, Mukesh Kumar, Neha Thakur, Toshiki Watanabe, Hideki Iba, Shintaro Kobayashi, Shogo Kawaguchi, Kazutaka Ikeda, Masato Hagihara, Takashi Kamiyama, Akihide Kuwabara, Hiroshi Kageyama, Yoshiharu Uchimoto
"Fluoride ion storage and conduction mechanism in fluoride ion battery cathode, Ruddlesden-Popper-type layered perovskite $La_{1.2}Sr_{1.8}Mn_2O_7$ crystal."
Chemistry of Materials, to be submitted.

Hidenori Miki, Kentaro Yamamoto, Cao Shuo, Toshiyuki Matsunaga, Mukesh Kumar, Neha Thakur, Yuki Sakaguchi, Toshiki Watanabe, Hideki Iba, Hiroshi Kageyama, Yoshiharu Uchimoto
"Accelerated fluoride-ion intercalation/deintercalation in a layered perovskite cathode by controlling the interlayer distance for fluoride-ion batteries."
Solid State Ionics, **2024**, 406, 116480.
https://doi.org/10.1016/j.ssi.2024.116480

■Chapter 5

Hidenori Miki, Kentaro Yamamoto, Cao Shuo, Wang Yanchang, Toshiyuki Matsunaga, Tomoki Uchiyama, Shinji Nakanishi, Hideki Iba, Koji Amezawa, Hiroshi Kageyama, Yoshiharu Uchimoto
"Effect on Anionic Redox of Transition Metal Species in Ruddlesden-Popper type Perovskites"
Chemistry of Materials, to be submitted.